Quantification of the Diffuser-Induced Speckle Error in Imaging Spectrometers

Quantifizierung des Diffusor-induzierten Speckle-Fehlers in abbildenden Spektrometern

Florian Richter

München 2021

Quantification of the Diffuser-Induced Speckle Error in Imaging Spectrometers

Quantifizierung des Diffusor-induzierten Speckle-Fehlers in abbildenden Spektrometern

Florian Richter

Dissertation

der Fakultät für Physik

der Ludwig-Maximilians-Universität

München

vorgelegt von

Florian Richter

aus Hamburg

München, den 19.07.2021

Erstgutachter: Prof. Dr. Mark Wenig

Zweitgutachter: Prof. Dr. Thomas Birner

Tag der mündlichen Prüfung: 13.09.2021

Contents

List of Figures

List of Tables

Abstract

Quantifying the impact of trace gases on the Earth's climate is of great interest. A method that has been widely employed over the last decades is spectroscopy via space-based passive imaging spectrometers. These instruments require a periodic radiometric calibration preferably with the Sun as a well-known reference. Also, the Sun spectrum is used as reference for the analysis of the measured spectra. During the acquisition, a diffuser is used to scatter the Sunlight into the instrument, thereby overfilling its pupil and field of view. The diffuse light coming from the diffuser induces an interference pattern at the detection plane, which is known as speckle. Depending on the used diffuser type and the design of the instrument, the speckle pattern may cause significant error amplitudes. The speckle error can not be reliably removed by post-processing or mitigated with common speckle reduction techniques because this would involve additional moving parts in the optical system and would pose a considerable risk of failure for space instruments. Hence, the speckle error needs to be suppressed by the design of certain instrument parameters. The characterization of speckle in imaging spectrometers was mostly done via representative end-to-end setups. Especially for recent instrument designs, which feature comparably small speckle amplitudes, this method is unreliable because the speckle error cannot be adequately distinguished from other error sources, such as straylight. Also, no comprehensive theoretical models have been presented that may completely explain results from measurements. In this thesis, an existing measurement technique is improved and characterized in terms of its errors and limitations. It is based on the acquisition of monochromatic speckle

patterns in the slit plane, which are then numerically propagated to the detection plane. This technique reduces the complexity of the measurement and isolates the error contribution by the diffuser. The main achievement of this thesis is the development of a standalone theoretical prediction model, which is based on the above measurement technique. The model needs basic instrument and diffuser scattering parameters as input and calculates the speckle error amplitude and the speckle size at the detector plane. It considers the speckle averaging effect from polarization, averaging by the spectral bandwidth perceived by the instrument, and averaging within detector pixels. The validity of the prediction model is tested in three ways. First, it is compared to the measurement technique mentioned above. Second, it is compared to a test measurement with a spectrometer. Third, it is used to emulate an artificial measurement with a spectrometer of the Global Ozone Monitoring Experiment, which is an Earth Observation mission for which the error of the retrieved column densities due to the diffuser is known. For this, the measured spectrum is distorted with a speckle error according to the model prediction. The resulting deviation in the retrieved column density is compared to literature. The results of all approaches are in good agreement with the prediction model. One can therefore infer that the developed model is a reliable and fast method to quantify the speckle error in imaging spectrometers, which requires no test setups and therefore makes it viable even in early planning phases of a mission. It is the first model completely resting on established speckle theory.

Zusammenfassung

Die Quantifizierung des Einflusses von Spurengasen auf das Klima der Erde ist von großem Interesse. Eine in den letzten Jahrzehnten häufig verwendete Methode ist die Spektroskopie mit weltraumgestützten, passiven, abbildenden Spektrometern. Diese Instrumente werden regelmäßig einer radiometrischen Kalibration unterzogen, die vorzugsweise mit der Sonne als Referenz durchgeführt wird. Diese Sonnenreferenz wird auch zur Analyse der gemessenen Erd-Spektra verwendet. Zur Kalibration dient ein Diffusor, der das Sonnenlicht in das Instrument streut und so dessen Pupille und Sichtfeld homogen ausleuchtet. Das vom Diffusor ausgehende diffuse Licht induziert ein Interferenzmuster an der Detektionsebene, das als Speckle bekannt ist. Je nach verwendetem Diffusortyp und der Konstruktion des Geräts kann das Speckle-Muster erhebliche Fehleramplituden verursachen. Der Speckle-Fehler kann nicht zuverlässig durch Post-Processing entfernt oder durch gängige Speckle-Reduktionsverfahren abgeschwächt werden, da dies zusätzliche bewegliche Teile im optischen System bedeuten und bei Weltrauminstrumenten ein erhebliches Ausfallrisiko darstellen würde. Daher muss der Speckle-Fehler möglichst im Vornherein durch das Anpassen bestimmter Instrumentenparameter unterdrückt werden. Die Charakterisierung von Speckle in abbildenden Spektrometern wurde meist über Ende-zu-Ende-Versuchsaufbauten durchgeführt, die das eigentliche Instrument nachbilden. Insbesondere für neuere Gerätedesigns, die vergleichsweise kleine Speckle-Amplituden aufweisen, ist diese Methode unzuverlässig, weil der Speckle-Fehler nicht genau von anderen Fehler-Quellen, wie beispielsweise Streulicht, unterschieden werden kann. Bisher sind auch keine umfassenden the-

oretischen Modelle bekannt, die Ergebnisse von Messungen vollständig erklären könnten. In dieser Arbeit wird ein existierendes Messverfahren verbessert und hinsichtlich seiner Fehler und Limitierungen charakterisiert. Monochromatische Speckle-Signale werden einzeln in der Spalt-Ebene gemessen und dann numerisch zur Detektionsebene propagiert. Dieses Verfahren reduziert die Komplexität der Messung und ermöglicht das alleinige Messen der Diffuser-Beiträge. Den Kern dieser Arbeit bildet die Entwicklung eines theoretisches Vorhersagemodell, das auf dem oben erwähnten Messverfahren beruht. Das Modell benötigt einige grundlegende Geräte- und Streuparameter des Diffusors als Eingabe und berechnet die Speckle-Fehleramplitude und die Speckle-Größe in der Detektorebene. Es werden die Mittelungseffekte durch Polarisation, durch die vom Instrument bedingte spektrale Bandbreite sowie Mittelungen innerhalb von Detektorpixel berücksichtigt. Die Gültigkeit des Vorhersagemodells wird auf drei Arten getestet. Erstens wird es mit dem oben erwähnten Messverfahren verglichen. Zweitens wird es mit einer Testmessung mit einem Spektrometer verglichen. Drittens wird es verwendet, um eine künstliche Messung mit einem Spektrometer des Global Ozone Monitoring Experiment zu emulieren, welches eine Erdbeobachtungsmission ist, für die der durch den Diffusor verursachte Fehler in der errechnten Säulen-Dichte bekannt ist. Dafür wird das gemessene Erd-Spektrum entsprechend der Modellvorhersage mit einem Speckle-Fehler verzerrt. Die resultierende Abweichung in der Säulen-Dichte wird mit der Literatur verglichen. Die Ergebnisse aller Ansätze stimmen gut mit den Vorhersagen des Modells überein. Daraus lässt sich schließen, dass das entwickelte Modell eine zuverlässige und schnelle Methode zur Quantifizierung des Speckle-Fehlers in abbildenden Spektrometern ist, das keine Versuchsaufbauten benötigt und damit auch in frühen Planungsphasen einsetzbar ist. Es ist das erste Modell, welches vollständig auf fundamentaler Speckle-Theorie basiert.

Chapter 1

Introduction

One of the most pressing challenges of our time is climate change (IPCC, 2015). It is a consequence of increased greenhouse gas emissions, especially over the last century (Hegerl et al., 2019). These trace gases are responsible for absorbing and reflecting the Earth's heat emission in the atmosphere. It is therefore of great interest to quantify the concentration of trace gases and to identify emission sources. For these tasks, space-based Remote-Sensing satellite missions play an integral role (IPCC, 2014, section 1.5). A widely used type of instrument is the passive imaging spectrometer that is installed on the satellites. These instruments record the light's intensity depending on its wavelength coming from the Earth. On its way from the Sun through the atmosphere, the light interacts with molecules by scattering, absorption, or reflection (see fig. 1.1). These processes have a characteristic wavelength dependency for every species known from laboratory measurements (Stutz et al., 2008, section 3.7.2). Therefore, one can, in principle, deduce the specific concentration of a trace gas by comparing the incoming spectrum of the Sun with the one being reflected by the Earth and looking for those intrinsic features. These passive spectroscopy methods are complemented by active techniques, such as Light Detection And Ranging (LIDAR) or Laser-Induced Fluorescence (LIF), where an artificial light source instead of the Sun is used.

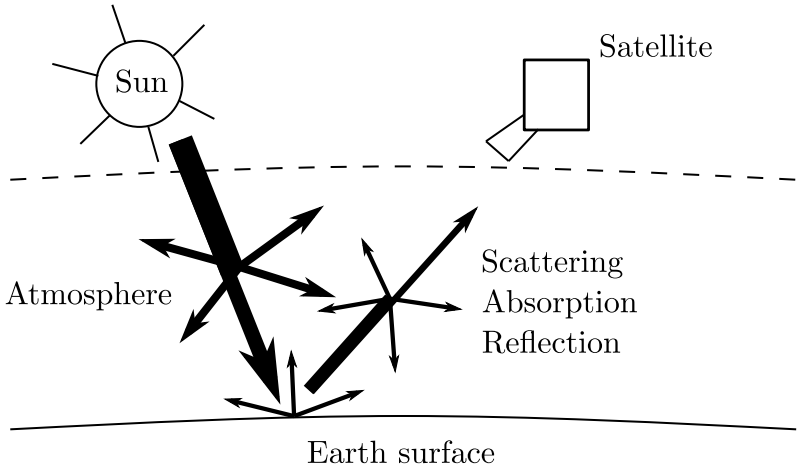

Figure 1.1: Illustration of passive Remote-Sensing via satellite. Light coming from the Sun propagates through the Earth's atmosphere to the satellite, thereby interacting with trace gas molecules by scattering, absorption, or reflection. These interactions can take place in the atmosphere and at the surface. Every species has its own unique spectral fingerprint for these interactions. The reflected and scattered light from the atmosphere is analyzed with respect to these fingerprints, which allows the retrieval of the respective trace gas concentration.

1.1 Remote-Sensing with Imaging Spectrometers

A space-based imaging spectrometer functions as follows: from an orbit above the atmosphere an area on the Earth surface (field of view) is captured by a telescope and focused at the entrance slit. The field at the slit is imaged through a dispersive element onto an array detector, thereby splitting the light into its spectral components. The work done in this thesis applies to both linear and two-dimensional array detectors. A schematic is shown in fig. 1.2. The instrument views different areas on the ground by orbiting in a Low Earth Orbit. Recent examples for this type of instrument are the Global Ozone Monitoring Experiment (GOME) onboard the European Research Satellite 2 (ERS-2) (ESTEC Publishing Division, 1995), the Envisat Medium Resolution Imaging Spectrometer (MERIS) (Olij et al., 1997), the Sentinel-5/UVNS instrument (Guehne et al., 2017), and the GreenHouse Gas Information System (GHGIS) instrument of CO2M, which is the former CarbonSat mission (Fletcher et al., 2015). In order to provide meaningful measurement data, the instrument is calibrated periodically in order to compensate for systematic

effects, such as detector aging. For the radiometric (intensity) calibration, the Sun is often used as a reference. The Sun has a perceived opening angle of 0.5°, which is far less than the field of view of an imaging spectrometer. Therefore, a diffuser is used to scatter the Sunlight into the instrument homogeneously, thereby overfilling the field of view. This is also illustrated in fig. 1.2.

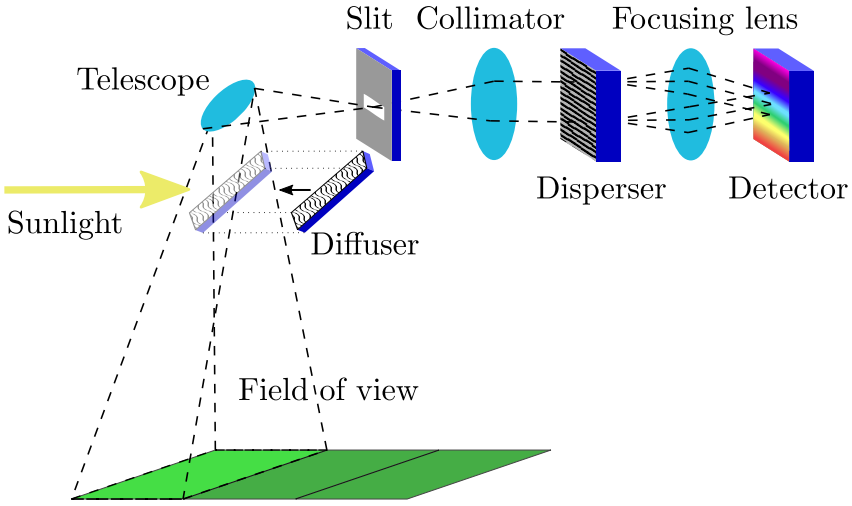

Figure 1.2: Schematic of an imaging spectrometer. A field of view on the Earth's surface is imaged by a telescope to the entrance slit. From there, it is imaged through a collimator, a dispersive element, and a focusing lens on an array detector. During the radiometric calibration, a diffuser is positioned in the field of view to homogeneously scatter Sunlight into the instrument.

1.2 Diffuser-Speckles in Imaging Spectrometers

The Sunlight scattered from the diffuser during the solar calibration gives rise to an interference pattern known as speckles (Richter and Wagner, 2001; Brug et al., 2004). The speckles propagate from the diffuser through the slit and disperser to the focal plane, where they are integrated. Here, they cause intensity fluctuations due to the peaks and valleys of these patterns called *Spectral Features* (Brug et al., 2004) and are illustrated in fig. 1.3. The diffuser essentially distorts the actual signal with a modulation, which is multiplicative. As a consequence, the Spectral Features create an error by altering the radiometric calibration function, which converts

the raw measured detector signal to calibrated radiances in terms of intensity. Also, for some methods, the solar reference spectrum can be used to analyze the measured Earth-shine spectra instead. Speckle effects are better known in the context of highly coherent light, such as holographic imaging (Bianco et al., 2018) or Laser Speckle Contrast Imaging (Heeman et al., 2019). Notable interference effects involving Sunlight, which has a broad spectrum compared to laser sources, might seem counter-intuitive at first glance. Indeed, the diffuse Sunlight coming from the diffuser does not yield a net speckle pattern with a substantial amplitude. However, the spectrum of the light incident on the instrument detector features only a limited bandwidth, namely the spectral resolution, which can be narrow enough to yield speckle patterns of significant amplitude. These Spectral Features depend on numerous geometric conditions, which make a prediction of the exact pattern at the detector plane unreliable. The quasi-statistical behavior also renders any mitigating post-processing steps ineffective. There are various speckle suppression techniques known (see J. W. Goodman, 2020, section 6) that may seem eligible in this case, such as rotation or tilting of components in the optical system. However, they require additional moving parts, which are usually not implemented in space-based instruments because of the supplementary risk of failure. The above methods are only viable in on-ground calibrations with static setups. A remaining option is the prediction of the diffuser speckle error. In combination with other radiometric error sources, such as straylight and polarization, it allows an a priori global optimization of the instrument in early planning phases. With this approach speckles can be suppressed by appropriately tuning specific design parameters of the spectrometers, such as spectral resolution, aperture dimensions, or slit dimensions.

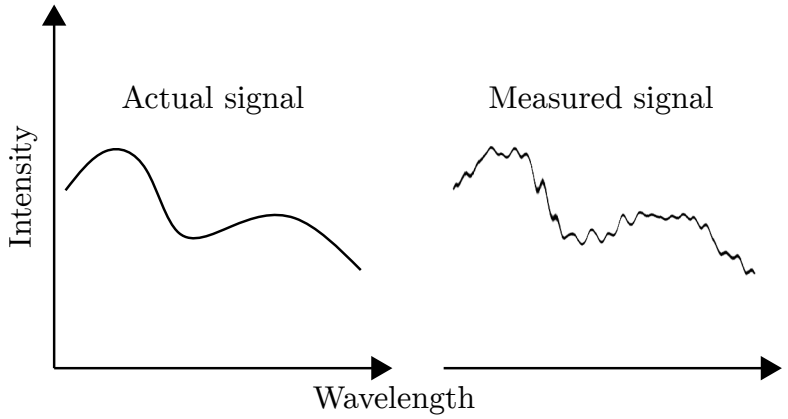

Figure 1.3: Distortion (Spectral Features) of the measured detector intensity by diffuser speckle during the solar radiometric calibration.

1.3 Need for New Diffuser-Speckle Characterization Techniques

One of the first imaging spectrometers, for which the issue of diffuser Spectral Features played a significant role, was the GOME instrument (Richter and Wagner, 2001). The observed deviation, for example, of NO_2 column densities retrieved with GOME data, were as high as 50 %. In the context of the Scanning Imaging Absorption Spectrometer for Atmospheric Chartography (SCIAMACHY) instrument "spectral oscillations" caused by the onboard diffuser were reported a few years later (Ahlers et al., 2004; Brug et al., 2004). End-to-end setups, such as proposed by Brug and Courrèges-Lacoste, 2007, served as characterization method. While representative setups may answer, whether a specific instrument design satisfies certain requirements regarding diffuser speckle, they provide little general insights concerning instrument parameters. Thus, the effort of quantifying the speckle error needed to be done for every planned spectrometer. Also, separating the diffuser speckle signal from other error sources in the setups is difficult to achieve. Although there have been attempts (Brug and Scalia, 2012), no comprehensive theoretical basis was available, which could connect instrument parameters to measurement results. For recent instruments such as the Sentinel 5/UVNS (Guehne et al., 2017) or the GHGIS instrument of CO2M (former CarbonSat), a novel approach was

proposed by Burns et al., 2017 and improved by Richter et al., 2018. It is based on the subsequent acquisition of monochromatic speckle patterns in the entrance slit of an instrument over the range of multiple times the spectral resolution. In a numerical simulation, the speckle patterns are propagated through the instrument, combined to a spectrum and integrated as such at the detector plane. This measurement technique as well as simplifying assumptions about the optical system reduce the experimental complexity and limit systematic error contributions. Since most of the instrument is simulated, this method is can produce comprehensive measurement data for most instrument designs. Most importantly, it removes the black-box character from the problem by allowing a step-by-step tracing of the speckle behavior throughout the instrument. Also, one can detect even the smallest speckle amplitudes with it. This important for the above-mentioned recent instrument designs, which use volume diffusers featuring smaller speckle error signals than can be reliably distinguished from other detected signals. Based on this novel measurement technique, a standalone mathematical prediction model is developed within this thesis and in Richter et al., 2021. It is the first model fundamentally based on speckle theory concepts.

Brug and Courrèges-Lacoste, 2007 first proposed the *Spectral Features Amplitude* (SFA) as a standardized measure of the diffuser speckle signal at the detector. It describes the amplitude of the features in the perceived spectrum that are solely caused by the diffuser. This is illustrated in fig. 1.4. By dividing the red graph by the blue one on the left-hand side yields the speckle signal as an amplitude relative to the mean normalized intensity. The SFA is defined as the standard deviation over multiple spectral channels of the diffuser speckle signal on the right-hand side. Another important parameter of the speckle signal is its average period or the speckle size L_c. It can be determined, for example, by calculating the autocorrelation of the amplitude signal.

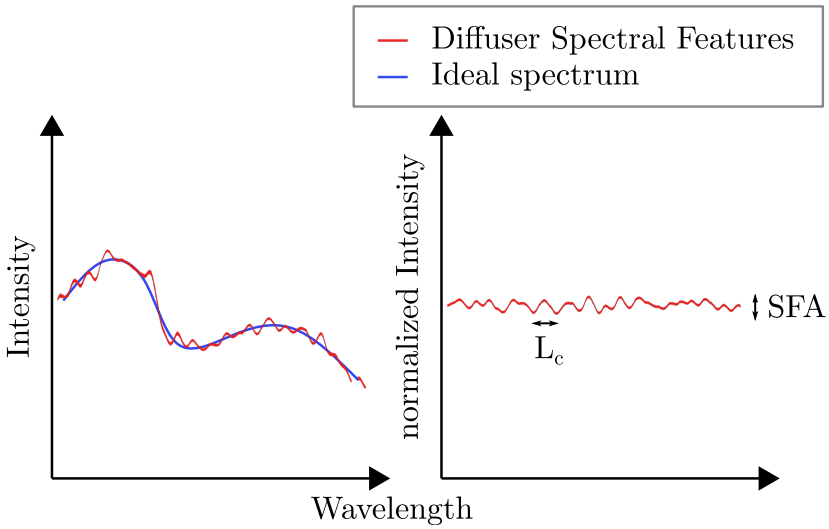

Figure 1.4: Left-hand side: detector signal (blue) and the intensity fluctuation due to diffuser speckle (red). Right-hand side: division of the red graph by the blue one yields the speckle signal as an amplitude relative to the mean normalized intensity. The standard deviation of this graph is the Spectral Features Amplitude (SFA). The average spectral length or period of the Spectral Features is denoted by L_c.

1.4 Outline of the Thesis

In this thesis, new ways for characterizing diffuser induced Spectral Features in imaging spectrometers are developed, improved, and assessed. The thesis begins with an introduction to theoretical concepts (chapter 2). First, some basics of probability theory are given in section 2.1, which are the prerequisite for the description of speckle in section 2.2. Then, a recently developed alternative measurement approach for diffuser Spectral Features is described in chapter 3. It is improved as well as characterized in terms of uncertainties. Based on this technique, a standalone mathematical prediction model is given in chapter 4. Results from both the measurement and prediction are compared for a current instrument design. In order to validate the prediction model, an end-to-end test spectrometer setup is designed and evaluated in terms of the Spectral Features in chapter 5. The results are then compared to the estimated prediction of the model. In chapter 6, the prediction model is used to estimate the impact of diffuser speckle on retrieved NO_2 column densities using the Differential Optical Absorption Spectroscopy method.

As a reference serves the GOME instrument, which allows a comparison between the deviations calculated in this study and the actually observed ones from literature. Hence, the validity of this model is shown in three ways. In chapter 7, the results of the thesis are summarized and evaluated. Finally, an outlook is given.

Chapter 2

Theory

In this chapter, the theoretical concepts needed to characterize speckles in imaging spectrometer are presented. First, a few basics from probability theory are introduced in section 2.1. They are needed for the statistical description of speckle in sections 2.2 and 2.3.

2.1 Probability Theory

The occurrence of speckles in an optical system needs to be treated as a random process. The presented terms and definitions can be found in Ibe, 2013; Klenke, 2013; J. W. Goodman, 2015, whereas the following summary of frequently used concepts, formulas, and notations is adopted from the first source.

Let's consider a random experiment with a spinner that can take every direction relative to a reference in a two-dimensional plane. The probability space Ω of the experiment contains every single possible outcome w and can be defined in the case of the spinner as $\Omega = [0°, 360°)$, which denotes every angle between the reference and direction spun of the spinner. A random variable $X(w)$[1] is a function that assigns a real number to every outcome w, $X : \Omega \longmapsto \xi$, whereas this case one can define $\xi = [0, 360)$. An event is defined as the subset of possible outcomes w

[1]Random variables are usually denoted as a single letter X without the function variable, hence we will follow that notation from here on.

that meet a certain criterion. For example $V = [X = 45] = 45°$ denotes an event consisting of all outcomes for which X is equal to 45. We can assign a probability to every event, e.g. for the above, we can write $p = P[X = 45] = 0$. This event is assigned zero probability because the chance of any angle being spun from the uncountable number of possible angles is infinitely small. However, the probability of a range of angles is non-zero. With the event $[X \leq x]$ the *cumulative distribution function* (CDF) F_X of X is defined by

$$F_X(x) = P[X \leq x] = \frac{x}{360}. \tag{2.1}$$

For the current example, we have $F_X(90) = P[X \leq 90] = \frac{1}{4}$. The function defined by

$$f_X(x) = \frac{dF_X(x)}{dx} = \frac{1}{360}, \tag{2.2}$$

that has the property for an event V,

$$P[V \in X] = \int_V f_X(x)\, dx \tag{2.3}$$

is called the *probability density function* (PDF) of X. The *expectation value* or *mean* of X is defined by

$$E[X] = \overline{X} = \int_\xi x f_X(x)\, dx = 180, \tag{2.4}$$

which can be interpreted as the weighted average of possible values of X. The nth moment of X for $n = 1, 2, 3...$ is defined by

$$E[X^n] = \overline{X^n} = \int_\xi x^n f_X(x)\, dx = \frac{360^n}{n+1}. \tag{2.5}$$

Note that the first moment is the expectation value X. The *central moments* give a

measure of the spread of a random variable about their means:

$$E\left[(X-\overline{X})^n\right] = \overline{(X-\overline{X})^n} = \int_\xi (x-\overline{X})^n f_X(x)\,dx\,. \tag{2.6}$$

The special case for $n = 2$ is called *variance* σ_X^2,

$$\sigma_X^2 = E\left[(X-\overline{X})^2\right] = E\left[X^2\right] - E\left[X\right]^2 = \frac{360^2}{3} - 180^2 = 10800, \tag{2.7}$$

where the third step follows from expanding the inner brackets and using $E\left[E\left[X\right]\right] = E\left[X\right]$. The *characteristic function* M_X of X is defined in terms of the PDF:

$$M_X(w) = E\left[e^{j\omega X}\right] = \int_\xi e^{j\omega x} f_X(x)\,dx = \frac{e^{j\omega 360}-1}{j\omega 360}. \tag{2.8}$$

Consider two random variables X and Y with means $E\left[X\right] = \overline{X}$ and $E\left[Y\right] = \overline{Y}$, and variances σ_X^2 and σ_Y^2, respectively. The *covariance* of X and Y, denoted by $Cov(X,Y)$ or σ_{XY}, is defined by

$$\sigma_{XY} = E\left[(X-\overline{X})(Y-\overline{Y})\right] = E\left[XY\right] - E\left[X\right]E\left[Y\right], \tag{2.9}$$

where the last step follows again from the same arguments used in equation 2.7. The covariance is a measure of linear correlation between the two random variables. X and Y are called *independent* if $E\left[XY\right] = E\left[X\right]E\left[Y\right]$. In this case they are also *uncorrelated*, because $\sigma_{XY} = 0$. However, the reverse does not necessarily hold. That is, if they are uncorrelated, it is still possible for them to be dependent in some non-linear way. A comparable method of measuring linear correlation is the *correlation coefficient* $\rho_{X,Y}$ of X and Y, which is defined as the normalized covariance by

$$\rho_{X,Y} = \frac{\sigma_{XY}}{\sigma_X \sigma_Y}. \tag{2.10}$$

2.2 Speckle Theory

In this section, a few frequently encountered fundamental concepts about speckles are summarized, which are mainly based on the work of J. W. Goodman, 2007. Based on this theory, the impact of speckle in imaging spectrometers can be well described.

2.2.1 First-Order Statistics of Speckles

We start with the description of an ideal or undisturbed speckle distribution, which will be the basis for all further discussions. The signal amplitude of an electromagnetic wave can be expressed with the cosine function in the space-time as (J. W. Goodman, 2020):

$$\mathcal{A}(x,y,t) = A(x,y,t)\cos[2\pi f_0 t - \theta(x,y,t)], \tag{2.11}$$

where A is the amplitude, f_0 is the center frequency, and θ the phase of the signal. It is convenient to write this signal as a complex phasor:

$$\mathbf{A}(x,y,t) = A(x,y,t)\, e^{i\theta(x,y,t)}. \tag{2.12}$$

This representation is equal to doubling the negative frequency components and suppressing the positive ones. The frequency term in the exponent is omitted because it is not needed in the following. This form allows for a natural description of speckle consisting of an amplitude and a phase without losing information about the original signal. A speckle field $\mathbf{A}$ can be considered a summation of a multitude of these signals having random amplitudes and phases. For a fixed point in space and time, the so-called *random phasor sum* is given by:

$$\mathbf{A} = Ae^{i\theta} = \frac{1}{\sqrt{N}}\sum_{n=1}^{N}\mathbf{a}_n = \frac{1}{\sqrt{N}}\sum_{n=1}^{N}a_n e^{i\phi_n}, \tag{2.13}$$

where $\mathbf{A}$ is the resultant complex phasor, N is the number of phasor components in the sum, A represents the magnitude of $\mathbf{A}$, θ the phase of the resultant, $\mathbf{a}_n$ the nth complex component phasor of the sum, a_n is the magnitude of $\mathbf{a}_n$, and ϕ_n is the phase of $\mathbf{a}_n$. Referring back to the notations introduced in the previous section 2.1 the amplitudes and phases are random variables with $a_n : \mathbb{R} \longmapsto \mathbb{R}$ and $\phi_n : \mathbb{G} \longmapsto \mathbb{G}$, where $\mathbb{G} := [-\pi, \pi)$. For the random phasor sum we have $\mathbf{A} : \left(\mathbb{R}^N, \mathbb{G}^N\right) \longmapsto (\mathbb{R}, \mathbb{G})$. Lets consider the real and imaginary part of $\mathbf{A}$

$$\mathcal{R} = \mathrm{Re}(\mathbf{A}) = \frac{1}{\sqrt{N}} \sum_{n=1}^{N} a_n \cos \phi_n \tag{2.14}$$

$$\mathcal{I} = \mathrm{Im}(\mathbf{A}) = \frac{1}{\sqrt{N}} \sum_{n=1}^{N} a_n \sin \phi_n \tag{2.15}$$

The following assumptions are presumed for the statistics of the component phasors that make up the sum:

1. Amplitudes and phases a_n and ϕ_n are statistically independent of a_m and ϕ_m for $n \neq m$.

2. For any n, a_n and ϕ_n are statistically independent of each other.

3. The phases ϕ_m are uniformly distributed on the interval $[-\pi, \pi)$.

With these assumptions in mind, let us consider the random phasor sum $\mathbf{A}$ for large N. The sum of the real and imaginary parts $\mathcal{R}$ and $\mathcal{I}$ of the resultant phasor $\mathbf{A}$ are then large sums of independent random variables. The *Central Limit Theorem* states that the statistics of the sum of N independent random variables is asymptotically Gaussian as N approaches infinity (see Marks, 2009). Hence, according to J. W. Goodman, 2015 one can combine $\mathcal{R}$ and $\mathcal{I}$ to a *bivariate*

Gaussian PDF with the general form for an arbitrary correlation as

$$f_{\mathcal{R},\mathcal{I}}(\mathcal{R},\mathcal{I}) = \frac{1}{2\pi\sigma_{\mathcal{R}}\sigma_{\mathcal{I}}\sqrt{1-\rho_{\mathcal{R}\mathcal{I}}}} \times \exp\left[-\frac{1}{2(1-\rho_{\mathcal{R}\mathcal{I}}^2)}\left(\frac{(\mathcal{R}-\overline{\mathcal{R}})^2}{\sigma_{\mathcal{R}}^2} + \frac{(\mathcal{I}-\overline{\mathcal{I}})^2}{\sigma_{\mathcal{I}}^2} - \frac{2\rho_{\mathcal{R}\mathcal{I}}(\mathcal{R}-\overline{\mathcal{R}})(\mathcal{I}-\overline{\mathcal{I}})}{\sigma_{\mathcal{R}}\sigma_{\mathcal{I}}}\right)\right] \tag{2.16}$$

In the following, the mean and variance of $\mathcal{R}$ and $\mathcal{I}$ are calculated explicitly. For the means we have

$$\begin{aligned} E[\mathcal{R}] &= E\left[\frac{1}{\sqrt{N}}\sum_{n=1}^{N} a_n \cos\phi_n\right] = \frac{1}{\sqrt{N}}\sum_{n=1}^{N} E\left[a_n\cos\phi_n\right] \\ &= \frac{1}{\sqrt{N}}\sum_{n=1}^{N} E\left[a_n\right] E\left[\cos\phi_n\right] = 0 \end{aligned} \tag{2.17}$$

$$\begin{aligned} E[\mathcal{I}] &= E\left[\frac{1}{\sqrt{N}}\sum_{n=1}^{N} a_n \sin\phi_n\right] = \frac{1}{\sqrt{N}}\sum_{n=1}^{N} E\left[a_n\sin\phi_n\right] \\ &= \frac{1}{\sqrt{N}}\sum_{n=1}^{N} E\left[a_n\right] E\left[\sin\phi_n\right] = 0, \end{aligned} \tag{2.18}$$

where the order of averaging and summation is interchanged. Due to the independence of a_n and ϕ_n the averaging can be separated, and we use the uniform statistics of ϕ_n, implying zero means for both $\cos\phi_n$ and $\sin\phi_n$. For calculating the variances we first consider for $n \neq m$, $E\left[\cos\phi_n\cos\phi_m\right] = E\left[\cos\phi_n\right]E\left[\cos\phi_m\right] = 0$ and also $E\left[\sin\phi_n\sin\phi_m\right] = 0$. Variances with zero means are equal to the second moment, hence we have

$$\begin{aligned} \sigma_{\mathcal{R}}^2 &= E\left[\mathcal{R}^2\right] = \frac{1}{\sqrt{N}}\sum_{n=1}^{N}\sum_{m=1}^{N} E\left[a_n a_m\right] E\left[\cos\phi_n\cos\phi_m\right] \\ &= \sum_{n=1}^{N}\frac{1}{\sqrt{N}} E\left[a_n^2\right] E\left[\cos^2\phi_n\right] = \frac{1}{\sqrt{N}}\sum_{n=1}^{N} E\left[a_n^2\right] E\left[\frac{1}{2}+\frac{1}{2}\cos 2\phi_n\right] \\ &= \frac{1}{\sqrt{N}}\sum_{n=1}^{N}\frac{E\left[a_n^2\right]}{2} \end{aligned} \tag{2.19}$$

$$\begin{aligned}\sigma_{\mathcal{I}}^2 = E\left[\mathcal{I}^2\right] &= \frac{1}{\sqrt{N}}\sum_{n=1}^{N}\sum_{m=1}^{N} E\left[a_n a_m\right] E\left[\sin\phi_n \sin\phi_m\right] \\ &= \sum_{n=1}^{N}\frac{1}{\sqrt{N}} E\left[a_n^2\right] E\left[\sin^2\phi_n\right] = \frac{1}{\sqrt{N}}\sum_{n=1}^{N} E\left[a_n^2\right] E\left[\frac{1}{2} - \frac{1}{2}\cos 2\phi_n\right] \\ &= \frac{1}{\sqrt{N}}\sum_{n=1}^{N}\frac{E\left[a_n^2\right]}{2}.\end{aligned} \tag{2.20}$$

Here we used that only terms for $n = m$ further contribute. Additionally, a trigonometry identity and the uniformity of $2\phi_n$ is utilized, which follows from the uniformity of ϕ_n. With similar steps, we can show that the real and imaginary part are uncorrelated:

$$\begin{aligned}\sigma_{\mathcal{RI}} &= E\left[\mathcal{RI}\right] - E\left[\mathcal{R}\right] E\left[\mathcal{I}\right] \\ &= E\left[\left(\sum_{n=1}^{N}\frac{1}{\sqrt{N}} a_n \cos\phi_n\right)\left(\sum_{m=1}^{N}\frac{1}{\sqrt{N}} a_m \sin\phi_m\right)\right] - 0 \\ &= \frac{1}{\sqrt{N}}\sum_{n=1}^{N} E\left[a_n^2\right] E\left[\cos\phi_n \sin\phi_n\right] \\ &= \frac{1}{\sqrt{N}}\sum_{n=1}^{N} E\left[a_n^2\right] E\left[\frac{1}{2}\sin 2\phi_n\right] = 0,\end{aligned} \tag{2.21}$$

where in the last step the double-angle trigonometric identity, and again, the uniformity of $2\phi_n$ is used. In summary, we established that $\mathcal{R}$ and $\mathcal{I}$ have zero means, are uncorrelated, and have equal variances. By taking into account the above findings, that is the zero means $\overline{\mathcal{R}} = \overline{\mathcal{I}} = 0$, equal variances $\sigma_{\mathcal{R}} = \sigma_{\mathcal{I}} = \sigma$, and zero correlation $\sigma_{\mathcal{RI}} = 0$, which implies $\rho_{\mathcal{RI}} = 0$ with eq. (2.10). The PDF in eq. (2.16) reduces to

$$f_{\mathcal{R},\mathcal{I}}\left(\mathcal{R},\mathcal{I}\right) = \frac{1}{2\pi\sigma^2}\exp\left[-\frac{\mathcal{R}^2 + \mathcal{I}^2}{2\sigma^2}\right]. \tag{2.22}$$

Because of the circular nature of equal probability values in the complex plane contingent by eq. (2.22) $\mathbf{A}$ is said to be a *circular complex Gaussian variable* (J. W. Goodman, 2015). To find the joint PDF of intensity and phase, one can use the rules of probability theory for the transformation of variables (J. W. Goodman,

2015). Consider the relations between real and imaginary parts to intensity and phase

$$\begin{aligned} I &= \mathcal{R}^2 + \mathcal{I}^2 \\ \theta &= \arctan\left(\frac{\mathcal{I}}{\mathcal{R}}\right) \end{aligned} \tag{2.23}$$

and

$$\begin{aligned} \mathcal{R} &= \sqrt{I}\cos\theta \\ \mathcal{I} &= \sqrt{I}\sin\theta. \end{aligned} \tag{2.24}$$

One can express the desired joint density function of intensity and phase through $\mathcal{R}$ and $\mathcal{I}$ by (Dainty et al., 1975)

$$f_{I,\theta} = f_{\mathcal{R},\mathcal{I}}\left(\sqrt{I}\cos\theta, \sqrt{I}\sin\theta\right)\|J\|, \tag{2.25}$$

where $\|J\|$ is the magnitude of the Jacobian determinant of the transformation between the two sets of variables,

$$\|J\| = \left\| \begin{matrix} \frac{\partial\mathcal{R}}{\partial I} & \frac{\partial\mathcal{R}}{\partial\theta} \\ \frac{\partial\mathcal{I}}{\partial I} & \frac{\partial\mathcal{I}}{\partial\theta} \end{matrix} \right\| = \frac{1}{2}. \tag{2.26}$$

Substituting eq. (2.22) in eq. (2.25) we find

$$f_{I,\theta} = \frac{1}{4\pi\sigma^2}\exp\left(-\frac{I}{2\sigma^2}\right), \tag{2.27}$$

where $I \geq 0$ and $-\pi \leq \theta < \pi$ (see initial assumption about the component phases). For this work, the intensity is of primary interest. The corresponding PDF is found by integration over the angular domain,

$$f_I(I) = \int_{-\pi}^{\pi} f_{I,\theta}(I,\theta)\,d\theta = \frac{1}{2\sigma^2}\exp\left(-\frac{I}{2\sigma^2}\right). \tag{2.28}$$

The nth moment is according to eq. (2.5)

$$\begin{aligned}\overline{I^n} &= \int_{-\infty}^{\infty} I^n f_I(I)\, dI = \int_0^{\infty} I^n \frac{1}{2\sigma^2} \exp\left(-\frac{I}{2\sigma^2}\right) dI \\ &= \left(2\sigma^2\right)^n n!,\end{aligned} \tag{2.29}$$

where in the second step the domain $I \geq 0$ of f_I is incorporated. From this result, we derive the mean intensity $\bar{I}$ is $2\sigma^2$, and we can write the PDF as

$$f_I(I) = \frac{1}{\bar{I}} \exp\left(-\frac{I}{\bar{I}}\right). \tag{2.30}$$

This distribution describes fully developed speckles.
An vital quantity to characterize speckle is the *contrast* C defined as the fraction of the standard deviation σ_I and mean intensity $\bar{I}$,

$$C = \frac{\sigma_I}{\bar{I}}. \tag{2.31}$$

This value shows the normalized magnitude of intensity fluctuations in an image and is the most important value used throughout this work to characterize speckle patterns. With eq. (2.29) we calculate C for the above type of speckle using the first and second moment:

$$C = \frac{\sqrt{\overline{I^2} - \bar{I}^2}}{\bar{I}} = \frac{\sqrt{2\bar{I}^2 - \bar{I}^2}}{\bar{I}} = 1. \tag{2.32}$$

Thus, for ideal or undisturbed speckles, we expect a contrast of unity. This kind of speckles are called *fully developed Gaussian speckles*. From hereon, it will be assumed that the underlying speckle statistic is the one just presented. For future references, we also calculate the characteristic function of intensity, which is given by eq. (2.8):

$$\mathbf{M}_I(\omega) = \int_0^{\infty} e^{jwI} f_I(I)\, dI = \int_0^{\infty} e^{jwI} \left[\frac{1}{\bar{I}} e^{-I/\bar{I}}\right] dI = \frac{1}{1 - j\omega\bar{I}}. \tag{2.33}$$

2.2.2 Statistics of the Sum of Independent Speckle Intensities

When dealing with speckles in spectrometers, the speckle statistic present on the detector plane of the instrument can not be considered ideal in the sense of the previous section. Instead, the net statistic can be considered as a summation of a number of the latter ones. This section discusses the hypothetical case, where all speckle intensities are independent, e.g., their spatial distributions have nothing in common. Let us consider the sum of N independent speckle intensities. For the total intensity, we have

$$I_S = \sum_{n=1}^{N} I_n. \tag{2.34}$$

The characteristic function $\mathbf{M}_S(\omega)$ of the sum of independent random variables I_S is the product of the characteristic function of their components $\mathbf{M}_n(\omega)$ (Marks, 2009),

$$\mathbf{M}_S(\omega) = \prod_{n=1}^{N} \mathbf{M}_n(\omega). \tag{2.35}$$

Assuming that every speckle pattern I_n is following the same statistics as derived in the previous section $\mathbf{M}_n(\omega)$ is given by eq. (2.33), yielding

$$\mathbf{M}_S(\omega) = \prod_{n=1}^{N} \frac{1}{1 - j\omega\overline{I_n}}, \tag{2.36}$$

where $\overline{I_n}$ is the mean intensity of the nth speckle pattern of the sum. By applying the inverse Fourier transformation to the characteristic function $\mathbf{M}_S(\omega)$ (see again eq. (2.33)), we get the PDF for the total intensity $p_S(I_S)$. A concrete result depends on the relations between the different values of mean intensity $\overline{I_n}$. If all $\overline{I_n}$ are distinct and nonzero, one finds for $I_S > 0$

$$f_S(I_S) = \sum_{n=1}^{N} \frac{\overline{I_n}^{N-2}}{\prod_{p=1,\, p\neq n}^{N} (\overline{I_n} - \overline{I_p})} \exp\left(-\frac{I_s}{\overline{I_n}}\right). \tag{2.37}$$

In a second case, if all $\overline{I_n}$ have the same value I_0 we get

$$f_S(I_S) = \frac{I_S^{N-1}}{\Gamma(N) I_0^N} \exp\left(-\frac{I_S}{I_0}\right) = \frac{N^N I_S^{N-1}}{\Gamma(N) \overline{I_S}^N} \exp\left(-N\frac{I_S}{\overline{I_S}}\right), \tag{2.38}$$

where $\overline{I_S} = NI_0$ is the total mean intensity. As in the previous section, the speckle contrast for the total intensity is of particular interest. Therefor, we determine the first and second moments. In the general case of distinct I_n with mean values $\overline{I_n}$, the first moment of the total intensity is seen to be

$$\overline{I_S} = \sum_{n=1}^{N} \overline{I_n}. \tag{2.39}$$

For the second moment we have

$$\overline{I_S^2} = \sum_{n=1}^{N}\sum_{m=1}^{N} \overline{I_n I_m} = \sum_{n=1}^{N} \overline{I_n^2} + \sum_{n=1}^{N}\sum_{m=1,\, m\neq n}^{N} \overline{I_n}\,\overline{I_m}, \tag{2.40}$$

where we use that I_n and I_m are independent for $m \neq n$. Additionally, we recall that every speckle pattern in the sum follows negative exponential statistics as described in section 2.2.1, from which follows that $\overline{I_n^2} = 2\overline{I_n}^2$ (see eq. (2.29)). We can rewrite the second moment as follows:

$$\overline{I_S^2} = 2\sum_{n=1}^{N} \overline{I_n}^2 + \sum_{n=1}^{N}\sum_{m=1,\, m\neq n}^{N} \overline{I_n}\,\overline{I_m} = \sum_{n=1}^{N} \overline{I_n}^2 + \left(\sum_{n=1}^{n} \overline{I_n}\right)^2 = \sum_{n=1}^{N} \overline{I_n}^2 + \overline{I_S}^2. \tag{2.41}$$

The variance calculates to

$$\sigma_s^2 = \overline{I_S^2} - \overline{I_S}^2 = \sum_{n=1}^{N} \overline{I_n}^2. \tag{2.42}$$

Finally, for the speckle contrast C for the sum of independent speckle intensities, we get

$$C = \frac{\sigma_S}{\overline{I_S}} = \frac{\sqrt{\sum_{n=1}^{N} \overline{I_n}^2}}{\sum_{n=1}^{N} \overline{I_n}}. \tag{2.43}$$

For the case of equal mean intensities in the sum ($\overline{I_n} = I_0 \,\forall\, n$), this yields the insightful result:

$$C = \frac{1}{\sqrt{N}}. \tag{2.44}$$

It tells us that by summing N completely different speckle images of the same intensity together, the speckle contrast is reduced by a factor of $\sqrt{N}$.

2.2.3 Statistics of the Sum of Correlated Speckle Intensities

We will now look at speckle intensities that are partially correlated to each other. The following is a generalization of section 2.2.2, where the correlation between all intensities is essentially zero. We start again with the sum of N speckle intensities:

$$I_S = \sum_{n=1}^{N} I_n = \sum_{n=1}^{N} |\mathbf{A}_n|^2. \tag{2.45}$$

The linear correlation between two speckle pattern intensities I_n and I_m is given by the correlation coefficient (see eq. (2.10)), which in our case yields on intensity basis

$$\rho_{n,m} = \frac{\overline{I_n I_m} - \overline{I_n}\,\overline{I_m}}{\sqrt{\overline{I_n^2} - \overline{I_n}^2}\sqrt{\overline{I_m^2} - \overline{I_m}^2}} = \frac{\overline{I_n I_m} - \overline{I_n}\,\overline{I_m}}{\overline{I_n},\,\overline{I_m}}, \tag{2.46}$$

where in the last step we use eq. (2.29) since the intensities follow a negative exponential distribution. Similarly, for the correlation coefficients of the complex fields $\mathbf{A}_n$ and $\mathbf{A}_m$ we have

$$\mu_{n,m} = \frac{\overline{\mathbf{A}_n \mathbf{A}_m^*} - \overline{\mathbf{A}_n}\,\overline{\mathbf{A}_m}}{\sqrt{\overline{\mathbf{A}_n^2} - \overline{\mathbf{A}_n}^2}\sqrt{\overline{\mathbf{A}_m^2} - \overline{\mathbf{A}_m}^2}} = \frac{\overline{\mathbf{A}_n \mathbf{A}_m^*}}{\sqrt{\overline{I_n}},\sqrt{\overline{I_m}}}, \tag{2.47}$$

where in the last step we invoke the circular Gaussian statistics of the fields (implying zero means) and use eq. (2.45). Additionally, this enables us to relate the correlation of the intensities to the ones of the fields (Middleton, 1960; J. W. Goodman, 2007) by

$$\Gamma_I = \overline{I_n I_m} = \overline{I_n}\,\overline{I_m}\left[1 + |\mu_{n,m}|^2\right]. \tag{2.48}$$

Substituting this into eq. (2.46) one can see that

$$\rho_{n,m} = |\mu_{n,m}|^2. \tag{2.49}$$

The form of $\mu_{n,m}$ is therefore

$$\mu_{n,m} = \sqrt{\rho_{n,m}} \exp(j\psi_{n,m}), \tag{2.50}$$

where $\psi_{n,m}$ is the phase term describing the correlation between the fields $\mathbf{A}_n$ and $\mathbf{A}_m$. To calculate the speckle contrast, we define the column vector $\underline{\mathcal{A}}$ containing all N fields

$$\underline{\mathcal{A}} = \begin{bmatrix} \mathbf{A}_1 \\ \mathbf{A}_2 \\ \vdots \\ \mathbf{A}_n \end{bmatrix}. \tag{2.51}$$

Every speckle field $\mathbf{A}_n$ has a certain amount of correlation with every other field $\mathbf{A}_m$ given by $\mu_{n,m}$. One can account for the different correlations between all fields by defining a coherency matrix $\underline{\mathcal{J}}$ as a mathematical representation by

$$\underline{\mathcal{J}} = \overline{\underline{\mathcal{A}}\underline{\mathcal{A}}^\dagger}, \tag{2.52}$$

where † stands for the Hermitian transpose operation. For the entries in the matrix we have $\mathbf{J}_{n,m} = \overline{\mathbf{A}_n \mathbf{A}_m^*}$, thus the coherency matrix can be written using eq. (2.47) as

$$\underline{\mathcal{J}} = \begin{bmatrix} \overline{I_1} & \sqrt{\overline{I_1}\,\overline{I_2}}\mu_{1,2} & \cdots & \sqrt{\overline{I_1}\,\overline{I_N}}\mu_{1,N} \\ \sqrt{\overline{I_1}\,\overline{I_2}}\mu_{1,2}^* & \overline{I_2} & \cdots & \sqrt{\overline{I_2}\,\overline{I_N}}\mu_{2,N} \\ \vdots & \vdots & \ddots & \vdots \\ \sqrt{\overline{I_1}\,\overline{I_N}}\mu_{1,N}^* & \sqrt{\overline{I_2}\,\overline{I_N}}\mu_{2,N}^* & \cdots & \overline{I_N} \end{bmatrix}. \tag{2.53}$$

The coherence matrix is *Hermitian* by construction because of the conjugate symmetry about the diagonal. Additionally, we see that $\overline{I_S} = \mathrm{tr}(\underline{\mathcal{J}})$, i.e. the total mean intensity is the sum over the diagonal of $\underline{\mathcal{J}}$. In the next step, we transform

the partially correlated field components that make up the sum to a basis, for which the correlation is zero (J. W. Goodman, 2015). The average intensities of the fields $\overline{I_n}$ (the diagonal entries of $\underline{\mathcal{J}}$) will, in general, be altered by this transformation. However, the total mean intensity $\overline{I_S}$ will remain constant. The above mentioned transformation of the speckle fields $\mathbf{A}_n$ is a unitary linear transformation $\underline{\mathcal{L}_0}$, that diagonalizes $\underline{\mathcal{J}}$:

$$\underline{\mathcal{J}'} = \underline{\mathcal{L}_0}\underline{\mathcal{J}}\underline{\mathcal{L}_0^\dagger} = \begin{bmatrix} \lambda_1 & 0 & \cdots & 0 \\ 0 & \lambda_2 & \cdots & 0 \\ \vdots & \vdots & \ddots & \vdots \\ 0 & 0 & \cdots & \lambda_N \end{bmatrix}. \tag{2.54}$$

Its existence is a result of matrix theory (Landi and Zampini, 2018). Due to its unitary nature, that is $\underline{\mathcal{L}_0}\underline{\mathcal{L}_0^\dagger} = \mathbb{1}$, it is lossless, meaning the total mean intensity $\overline{I_S} = \mathrm{tr}(\underline{\mathcal{J}}) = \mathrm{tr}(\underline{\mathcal{J}'})$ is retained. Also, according to J. W. Goodman, 2007 the circular complex Gaussian statistics of the underlying fields are preserved. Note, that the complex coherence factor of eq. (2.50) includes a phase $\psi_{n,m}$. One can show, that due to the construction of $\underline{\mathcal{J}}$ the phase term can be omitted when calculating the eigenvalues (Dainty et al., 1975, Sect. 4.7.2). After transforming an ensemble of correlated speckle fields with average intensity $\overline{I_n}$ to an uncorrelated one with different individual average intensities λ_n (while retaining the total average intensity I_S), we can use the results from section 2.2.2. Hence, for the speckle contrast we can write in accordance with eq. (2.43),

$$C = \frac{\sigma_S}{\overline{I_S}} = \frac{\sqrt{\sum_{n=1}^{N} \lambda_n^2}}{\sum_{n=1}^{N} \lambda_n}. \tag{2.55}$$

2.2.4 Statistics of Polarized Speckle Intensities

Another effect that can influence the observed speckle contrast is polarization, which is discussed in this section. The polarization state of light describes the orientation of the electric field oscillations in a (x, y)-plane perpendicular to the propagation direction z of the light. We start with linearly polarized light in x

direction incident on a diffusing material,

$$\vec{\mathbf{A}}_i = \sqrt{I_i}\hat{x}, \tag{2.56}$$

where I_i is the incident intensity and $\hat{x}$ the unit vector in the x-direction. The observed light can be written as

$$\vec{\mathbf{A}}_o = \mathbf{A}_x\hat{x} + \mathbf{A}_y\hat{y}. \tag{2.57}$$

Hence for the total observed intensity, we get

$$I = I_x + I_y = \left|\mathbf{A}_x^2\right| + \left|\mathbf{A}_y^2\right|. \tag{2.58}$$

We assume that the speckle intensities follow a negative exponential distribution as described in section 2.2.1. Recalling section 2.2.3 the current case can be thought of as the sum of two correlated speckle intensities. Therefore, the correlation between the two underlying speckle fields $\mathbf{A}_x$ and $\mathbf{A}_y$ is

$$\rho_{x,y} = |\mu_{x,y}|^2. \tag{2.59}$$

We follow the same formalism as introduced in section 2.2.3 and write for the coherency matrix

$$\underline{\mathcal{J}} = \begin{bmatrix} \overline{I_x} & \sqrt{\overline{I_x}\,\overline{I_y}}\mu_{x,y} \\ \sqrt{\overline{I_x}\,\overline{I_y}}\mu_{x,y}^* & \overline{I_y} \end{bmatrix}, \tag{2.60}$$

which can be diagonalized with linear unitary transformation $\underline{\mathcal{L}_0}$ to

$$\underline{\mathcal{J}'} = \begin{bmatrix} \lambda_1 & 0 \\ 0 & \lambda_2 \end{bmatrix}. \tag{2.61}$$

It yields a trivial result in case of no correlation ($\mu_{x,y} = 0$) between the two components. The two eigenvalues of the coherence matrix are explicitly given by

$$\lambda_{1,2} = \frac{1}{2}\left[\overline{I_x} + \overline{I_y} \pm \sqrt{\left(\overline{I_x} - \overline{I_y}\right) + 4\overline{I_x}\overline{I_y}\left|\mu_{x,y}\right|^2}\right]. \tag{2.62}$$

We verify with eq. (2.62) that

$$\overline{I_x} + \overline{I_y} = \lambda_1 + \lambda_2 = \bar{I} \tag{2.63}$$

and conclude that in analogy to the previous case, we can describe light with correlated x and y polarization components as uncorrelated in the new basis x' and y' with different component intensities. Hence, for completely depolarized light λ_1 and λ_2 are of equal strength and without loss of generality we have $\lambda_1 > \lambda_2$ for polarized light. According to Wolf, 1959, we can decompose the diagonalized coherence matrix using these two arguments by

$$\underline{\mathcal{J}'} = \begin{bmatrix} \lambda_2 & 0 \\ 0 & \lambda_2 \end{bmatrix} + \begin{bmatrix} \lambda_1 - \lambda_2 & 0 \\ 0 & 0 \end{bmatrix}. \tag{2.64}$$

In doing so we describe the light as a composition of a completely depolarized and a completely polarized part. We recall that the total intensity is still given by eq. (2.63) and the polarized one by $\lambda_1 - \lambda_2$. We define the degree of polarization as

$$\mathcal{P} = \frac{\lambda_1 - \lambda_2}{\lambda_1 + \lambda_2} \tag{2.65}$$

which can take a value between 1 for full polarization and 0 for complete depolarized light. We can express the $\mathcal{P}$ using eq. (2.62),

$$\mathcal{P} = \frac{\sqrt{\left(\overline{I_x} - \overline{I_y}\right)^2 + 4\overline{I_x}\overline{I_y}\left|\mu_{x,y}\right|^2}}{\overline{I_x} + \overline{I_y}}. \tag{2.66}$$

By using eq. (2.65) one can write the eigenvalues in terms of $\mathcal{P}$,

$$\lambda_{1,2} = \frac{1}{2}\bar{I}\,(1 \pm \mathcal{P})\,. \tag{2.67}$$

We are now able to calculate the speckle contrast according to eq. (2.43) as

$$C = \frac{\sqrt{\lambda_1^2 + \lambda_2^2}}{\lambda_1 + \lambda_2} = \frac{\sqrt{\frac{1}{4}\bar{I}^2(1+\mathcal{P})^2 + \frac{1}{4}\bar{I}^2(1-\mathcal{P})^2}}{\bar{I}} = \sqrt{\frac{1+\mathcal{P}^2}{2}}. \tag{2.68}$$

As $\mathcal{P}$ approaches zero C converges the same value as it has been derived in section 2.2.2 for $N = 2$, i.e. the sum of two independent speckle intensities. For fully polarized light ($\mathcal{P} = 1$) no reduction takes place.

2.2.5 Speckle Size

A very important characteristic of speckles is their spatial extent governed by the optical system they originated from. J. W. Goodman, 2007; Dainty et al., 1975 have derived a way to determine the size of a speckle utilizing the autocorrelation function of the speckle field between different points in the imaging plane. Consider a planar

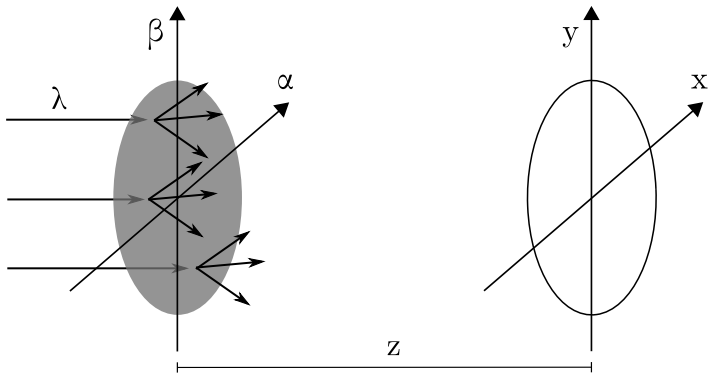

Figure 2.1: Free-space scattering geometry in transmission. Light incident from the left is scattered by a diffuser at the (α, β)-plane and observed in a finite area in the (x, y)-plane a distance z downstream. Adapted from J. W. Goodman, 2020.

rough diffuser, as depicted in fig. 2.1, in a plane (α, β), which is homogeneously illuminated by coherent light of wavelength λ. The parallel imaging plane (x, y)

is positioned at a distance z from the diffuser plane. The diffuser is assumed to be rough enough to induce phase shifts of multiple times 2π. Additionally, we only consider points in the imaging plane close to the z-axis; that is, only small scattering angles are considered (*paraxial propagation*). This enables us to express the complex field amplitude of the light in the imaging plane in terms of the scattered field amplitude in the plane just behind the diffuser by the Fresnel diffraction integral (see J. W. Goodman, 2017),

$$\mathbf{A}(x,y) = \frac{e^{jkz}}{j\lambda z} e^{j\frac{k}{2z}(x^2+y^2)} \iint_{-\infty}^{\infty} \mathbf{a}(\alpha,\beta) e^{j\frac{k}{2z}(\alpha^2+\beta^2)} e^{j\frac{2\pi}{\lambda z}(x\alpha+y\beta)}\, d\alpha\, d\beta\,. \tag{2.69}$$

As mentioned in the beginning, we want to find the autocorrelation function $\Gamma_{\mathbf{A}}$ of the speckle fields in the imaging plane between to points (x_1, y_1) and (x_2, y_2),

$$\Gamma_{\mathbf{A}}\left((x_1,y_1),(x_2,y_2)\right) = E\left[\mathbf{A}(x_1,y_1)\mathbf{A}^{\star}(x_2,y_2)\right]. \tag{2.70}$$

Substituting this into eq. (2.69) gives

$$\begin{aligned}\Gamma_{\mathbf{A}}\left((x_1,y_1),(x_2,y_2)\right) = \frac{1}{\lambda^2 z^2} e^{j\frac{k}{2z}(x_1^2+y_1^2-x_2^2-y_2^2)} \iint_{-\infty}^{\infty} \iint_{-\infty}^{\infty} \Gamma_{\mathbf{a}}\left((\alpha_1,\beta_1),(\alpha_2,\beta_2)\right) \\ \times\, e^{j\frac{k}{2z}(\alpha_1^2+\beta_1^2-\alpha_2^2-\beta_2^2)} e^{j\frac{2\pi}{\lambda z}(x_1\alpha_1+y_1\beta_1-x_2\alpha_2-y_2\beta_2)}\, d\alpha_1\, d\beta_1\, d\alpha_2\, d\beta_2\,,\end{aligned} \tag{2.71}$$

where $\Gamma_{\mathbf{a}}\left((\alpha_1,\beta_1),(\alpha_2,\beta_2)\right) = E\left[\mathbf{a}(\alpha_1,\beta_1)\mathbf{a}^{\star}(\alpha_2,\beta_2)\right]$ denotes the correlation function of the scattered fields just behind the diffuser plane. For the next step, the light exiting the diffuser plane is assumed to be completely spatially incoherent. This means that the spatial correlation function $\Gamma_{\mathbf{a}}$ of the scattered field $\mathbf{a}(\alpha,\beta)$ is as narrow, that it can be approximated by a delta function:

$$\Gamma_{\mathbf{a}}((\alpha_1,\beta_1),(\alpha_2,\beta_2)) = \kappa I(\alpha_1,\beta_1)\delta(\alpha_1-\alpha_2,\beta_1-\beta_2). \tag{2.72}$$

κ denotes constant with dimensions length squared, $I(\alpha_1, \beta_1)$ the field intensity just behind the diffuser plane, and $\delta(\alpha_1 - \alpha_2, \beta_1 - \beta_2)$ the two-dimensional delta function. Substituting this into eq. (2.71), we get

$$\begin{aligned}
&\Gamma_{\mathbf{A}}\left((x_1, y_1), (x_2, y_2)\right) = \\
&\quad \frac{1}{\lambda^2 z^2} e^{j\frac{k}{2z}(x_1^2 + y_1^2 - x_2^2 - y_2^2)} \iiiint_{-\infty}^{\infty} \kappa I(\alpha_1, \beta_1) \delta(\alpha_1 - \alpha_2, \beta_1 - \beta_2) \\
&\quad \times e^{j\frac{k}{2z}(\alpha_1^2 + \beta_1^2 - \alpha_2^2 - \beta_2^2)} e^{j\frac{2\pi}{\lambda z}(x_1\alpha_1 + y_1\beta_1 - x_2\alpha_2 - y_2\beta_2)} \, d\alpha_1 \, d\beta_1 \, d\alpha_2 \, d\beta_2 \\
&\quad = \frac{\kappa}{\lambda^2 z^2} e^{j\frac{k}{2z}(x_1^2 + y_1^2 - x_2^2 - y_2^2)} \iint_{-\infty}^{\infty} I(\alpha_1, \beta_1) e^{-j\frac{2\pi}{\lambda z}(\alpha_1(x_1 - x_2)\beta_1(x_1 - x_2)} \, d\alpha_1 \, d\beta_1 \, .
\end{aligned} \tag{2.73}$$

For future purposes we are only interested in the modulus of the autocorrelation function of the fields $|\Gamma_{\mathbf{A}}|$, thus we can omit the complex term in front of the integral. Also, we substitute $\Delta x = x_1 - x_2$ and $\Delta y = y_1 - y_2$ and replace the coordinates (α_1, β_1) by (α, β). The resulting expression for $\Gamma_{\mathbf{A}}$ becomes

$$\Gamma_{\mathbf{A}}(\Delta x, \Delta y) = \frac{\kappa}{\lambda^2 z^2} \iint_{-\infty}^{\infty} I(\alpha, \beta) e^{-j\frac{2\pi}{\lambda z}(\alpha\Delta x + \beta\Delta y)} \, d\alpha \, d\beta \, , \tag{2.74}$$

which, apart from the constant factor in front of the integral, is the two-dimensional Fourier transform of the scattered intensity at the diffuser. In other words, the autocorrelation function of the fields in the observation plane can be described, under the approximations made, by the Fourier transform of the scattered intensity just behind the diffuser plane. This is an equivalent result of coherence theory known as *van Cittert–Zernike Theorem* and is described in Hecht and Lippert, 2018, p. 1131f. In order to find an expression for the correlation coefficient of the fields, we recall its definition as normalized covariance from eq. (2.10) and see that for zero mean fields, we get

$$\mu_{\mathbf{A}}(\Delta x, \Delta y) = \frac{\Gamma_{\mathbf{A}}(\Delta x, \Delta y)}{\Gamma_{\mathbf{A}}(0, 0)} = \frac{\iint_{-\infty}^{\infty} I(\alpha, \beta) e^{-j\frac{2\pi}{\lambda z}(\alpha\Delta x + \beta\Delta y)} \, d\alpha \, d\beta}{\iint_{-\infty}^{\infty} I(\alpha, \beta) \, d\alpha \, d\beta} . \tag{2.75}$$

The autocorrelation of intensity is found by using eq. (2.48)

$$\Gamma_I(\Delta x, \Delta y) = \bar{I}^2\big[1 + |\mu_{\mathbf{A}}(\Delta x, \Delta y)|^2\big], \tag{2.76}$$

and the normalized autocorrelation function (see eq. (2.10)) is determined to be

$$\rho_I(\Delta x, \Delta y) = \frac{\Gamma_I(\Delta x, \Delta y) - \bar{I}^2}{\sigma_I \sigma_I} = \frac{\Gamma_I(\Delta x, \Delta y) - \bar{I}^2}{\bar{I}^2} = |\mu_{\mathbf{A}}(\Delta x, \Delta y)|^2. \tag{2.77}$$

In the second step eq. (2.29) and in the last one eq. (2.76) is used. The "size" of an speckle can now be defined via the correlation area $\mathcal{A}_c$ by integrating over $\rho_I(\Delta x, \Delta y)$

$$\mathcal{A}_c = \iint_{-\infty}^{\infty} \rho_I(\Delta x, \Delta y)\, d\Delta x\, d\Delta y = \iint_{-\infty}^{\infty} |\mu_{\mathbf{A}}(\Delta x, \Delta y)|^2\, d\Delta x\, d\Delta y\,. \tag{2.78}$$

We will now calculate the speckle size for a rectangular scattering spot (or pupil) of dimension $L_\alpha \times L_\beta$. Therefor we define $I(\alpha, \beta)$ to be

$$I(\alpha, \beta) = I_0 \Pi\left(\frac{\alpha}{L_\alpha}\right)\Pi\left(\frac{\beta}{L_\beta}\right), \tag{2.79}$$

where $\Pi(x)$ is the rectangle function, which is unity for $|x| \leq \frac{1}{2}$ and zero otherwise. The Fourier transform of $I(\alpha, \beta)$ calculates according to eq. (2.75) as follows:

$$\mu_{\mathbf{A}}(\Delta x, \Delta y) = \frac{\iint_{-\infty}^{\infty} I(\alpha, \beta) e^{-j\frac{2\pi}{\lambda z}(\alpha\Delta + \beta\Delta y}\, d\alpha\, d\beta}{\iint_{-\infty}^{\infty} I(\alpha, \beta)\, d\alpha\, d\beta} = \mathrm{sinc}\left(\frac{L_\alpha \Delta x}{\lambda z}\right)\mathrm{sinc}\left(\frac{L_\beta \Delta y}{\lambda z}\right), \tag{2.80}$$

where $\mathrm{sinc}(x) = \sin(\pi x)/(\pi x)$ is the sinc function. By substituting this into eq. (2.78) we get for the correlation area

$$\mathcal{A}_c = \iint_{-\infty}^{\infty} \mathrm{sinc}^2\left(\frac{L_\alpha \Delta x}{\lambda z}\right)\mathrm{sinc}^2\left(\frac{L_\beta \Delta y}{\lambda z}\right) d\Delta x\, d\Delta y = \frac{\lambda^2 z^2}{L_\alpha L_\beta}. \tag{2.81}$$

The one-dimensional representation of the size of a speckle in α or β direction can be defined as

$$L_{c,\,\alpha/\beta} = \frac{\lambda z}{L_{\alpha/\beta}}. \tag{2.82}$$

For the case of a circular scattering spot shape of diameter D we define $I(\alpha, \beta)$ as

$$I(\alpha, \beta) = \mathrm{circ}\left(\frac{2r'}{D}\right), \tag{2.83}$$

where $r' = \sqrt{\alpha^2 + \beta^2}$ and

$$\mathrm{circ}(r') = \begin{cases} 1 & r' \leq 1 \\ 0 & \text{otherwise.} \end{cases} \tag{2.84}$$

The two-dimensional Fourier transform of this function calculates to

$$\begin{aligned}
&\iint_{-\infty}^{\infty} \mathrm{circ}\left(\frac{2r'}{D}\right) e^{-j\frac{2\pi}{\lambda z}(\alpha\Delta + \beta\Delta y)}\, d\alpha\, d\beta \\
&= \int_0^{\infty} r' \mathrm{circ}\left(\frac{2r'}{D}\right) dr' \int_{-\pi}^{\pi} e^{-j\frac{2\pi}{\lambda z} r r' (\cos(\theta)\cos(\phi) + \sin(\theta)\sin(\phi))}\, d\theta \\
&= \int_0^{D/2} r'\, dr' \int_{-\pi}^{\pi} e^{-j\frac{2\pi}{\lambda z} r r' \cos(\theta - \phi)}\, d\theta \\
&= \int_0^{D/2} r'\, dr'\, 2 \int_0^{\pi} e^{j\frac{2\pi}{\lambda z} r r' \cos(\theta')}\, d\theta' \\
&= 2\pi \int_0^{D/2} r' J_0\left(\frac{2\pi r}{\lambda z} r'\right) dr' = 2\pi \left(\frac{\lambda z}{2\pi r}\right)^2 \int_0^{\pi D r/(\lambda z)} u J_0(u)\, du \\
&= 2\pi \left(\frac{\lambda z}{2\pi r}\right)^2 \frac{\pi D}{\lambda z} r J_1\left(\frac{\pi D}{\lambda z} r\right) = 2\pi \left(\frac{D}{2}\right)^2 \frac{J_1\left(\frac{\pi D}{\lambda z} r\right)}{\frac{\pi D}{\lambda z} r},
\end{aligned} \tag{2.85}$$

where in the second step the integral is transformed to the polar coordinate system (Baddour, 2011) with $r = \sqrt{(\Delta x)^2 + (\Delta y)^2}$. In the third step the above definition of the circ function and a trigonometric identity in the exponent is used. For the following step the integral definition of the Bessel function of first kind, nth order (see Erdélyi et al., 1953, §7.12(2)), $J_n(x) = \frac{i^{-n}}{\pi} \int_0^{\pi} e^{ix\cos(\theta)} \cos(n\theta)\, d\theta$ is used to solve the integral over θ'. Afterwards the integral identity $\int_0^a u J_0(u)\, du = a J_1(a)$ is

used for the second integral. For the correlation coefficient of the fields, we then get

$$\begin{aligned}\mu_{\mathbf{A}}(\Delta x, \Delta y) =& \frac{\iint_{-\infty}^{\infty} \operatorname{circ}\left(\frac{2r'}{D}\right) e^{-\frac{2\pi}{\lambda z}(\alpha\Delta)+\beta\Delta y}\, d\alpha\, d\beta}{\iint_{-\infty}^{\infty} \operatorname{circ}\left(\frac{2r'}{D}\right) d\alpha\, d\beta} \\ =& \frac{2\pi\left(\frac{D}{2}\right)^2 \frac{J_1\left(\frac{\pi D}{\lambda z} r\right)}{\frac{\pi D}{\lambda z} r}}{\pi\left(\frac{D}{2}\right)^2} = 2\frac{J_1\left(\frac{\pi D}{\lambda z} r\right)}{\frac{\pi D}{\lambda z} r}.\end{aligned} \tag{2.86}$$

The correlation area calculates to

$$\mathcal{A}_c = 4\pi \int_0^{\infty} r \left| \frac{J_1\left(\frac{\pi D}{\lambda z} r\right)}{\frac{\pi D}{\lambda z} r} \right|^2 dr = \frac{(\lambda z)^2}{\pi (D/2)^2}, \tag{2.87}$$

where the double integral is again transformed into polar coordinates and the normalization of the Bessel function $\int_0^{\infty} J_1(ax)\, dx = 1/a$ is used. Analog to the rectangular case, we define the one-dimensional representation to be the square root of the correlation area,

$$L_c = \frac{2\lambda z}{\sqrt{\pi} D} \tag{2.88}$$

which reminds one of the well-known Airy disc size (Hecht and Lippert, 2018, p. 937), $d_{Airy} = 1.22\frac{\lambda z}{D}$. This is a consequence of the van Cittert–Zernike Theorem used in the derivation of the speckle size (Hecht and Lippert, 2018, p. 1136). We have established the speckle size for a free space geometry and a rectangular as well as a circular scattering spot shape. We have established the speckle size for a free-space geometry and a rectangular as well as a circular scattering spot shape. In J. W. Goodman, 2007 the argument is made that the above result can be applied to an imaging geometry shown in fig. 2.2, as well. In this case, the scattering surface is effectively located in the exit pupil of the imaging system. The exit pupil is defined as the image of the limiting aperture perceived from the image side of the system, which means that the variable z can be replaced with z_i in all previously derived equations for the imaging case (J. W. Goodman, 2017, pp. 411-413). This result implies that the speckle correlation is usually not influenced by optical aberrations

by the imaging lens (J. W. Goodman, 2020, section 5.1.2).

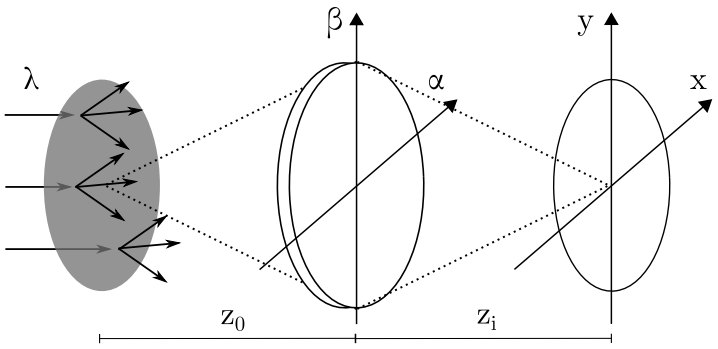

Figure 2.2: Imaging scattering geometry in transmission. Light incident from the left emerges from diffuser and is imaged by a lens in the (α, β)—plane a distance z_0 downstream. The observation plane (x, y) is in the focal plane of the lens located a distance z_i behind it. Adapted from J. W. Goodman, 2020.

2.2.6 Statistics of Integrated Speckles

Experimentally speckle can be measured with an array detector with an active area divided into pixels of finite size. Thus speckle fields are being sampled with the area of a detector element. Let's consider the measured intensity W of a uniform detector pixel

$$W = \frac{1}{\mathcal{A}_D} \iint_{-\infty}^{\infty} D(x,y) I(x,y)\, dx\, dy\,, \tag{2.89}$$

where $I(x, y)$ is the intensity of the speckle pattern being detected, and $\mathcal{A}_D = \iint_{-\infty}^{\infty} D(x, y)\, dx\, dy$ is the area of one detector element, with

$$D(x,y) = \begin{cases} 1 & \text{inside the pixel} \\ 0 & \text{outside pixel.} \end{cases} \tag{2.90}$$

As before, we are interested in the contrast, for which we, again, need to find the first and second moment to calculate the variance. For the first moment, we have

$$\overline{W} = \frac{1}{\mathcal{A}_D} \iint_{-\infty}^{\infty} D(x,y) \bar{I}\, dx\, dy = \bar{I}, \tag{2.91}$$

where the orders of averaging and integration have been interchanged again, and $\bar{I}$ is assumed independent of position. Therefore, the measured mean intensity is equal to the actual mean intensity of the speckle field. Similarly, for the second moment, we have

$$\overline{W^2} = \frac{1}{\mathcal{A}_D^2} \iint_{-\infty}^{\infty} \iint_{-\infty}^{\infty} D(x_1, y_1) D(x_2, y_2) \overline{I(x_1, y_1) I(x_2, y_2)} \, dx_1 \, dy_1 \, dx_2 \, dy_2 \, . \tag{2.92}$$

For the next step, the speckle pattern is assumed to be *wide-sense stationary*. In literature, this kind of stationarity is commonly referred to with respect to the parameter time t (Ibe, 2013). Given a random process $X(t)$ parameterized by time t, this wide-sense stationary criterion is met if the mean and the autocorrelation function are independent of absolute time (J. W. Goodman, 2015; Ibe, 2013), i.e.,

1) $E\left[X(t)\right] = \mu$, independent of t

2) $\Gamma_X(t_1, t_2) = \Gamma_X(\Delta t)$, is a function of only the time difference $\Delta t = t_2 - t_1$

If we extend this stationarity to the position parameter $\underline{p} = (x, y)$, we can write the mean of the intensity products in terms of the coordinate differences $\Delta x = x_1 - x_2$ and $\Delta y = y_1 - y_2$, which reduces the second moment to

$$\overline{W^2} = \frac{1}{\mathcal{A}_D^2} \iint_{-\infty}^{\infty} K_D(\Delta x, \Delta y) \Gamma_I(\Delta x, \Delta y) \, d\Delta x \, d\Delta y \, , \tag{2.93}$$

where $K_D(\Delta x, \Delta y)$ is the deterministic autocorrelation function of the detector element aperture $D(x, y)$,

$$K_D(\Delta x, \Delta y) = \iint_{-\infty}^{\infty} D(x_1, y_1) D(x_1 - \Delta x, y_1 - \Delta y) \, dx_1 \, dy_1 \, , \tag{2.94}$$

and Γ_I is the statistical autocorrelation function of the intensity $I(x, y)$. We use eq. (2.48) to write

$$\Gamma_I(\Delta x, \Delta y) = \bar{I}^2 \left[1 + |\mu_A(\Delta x, \Delta y)|^2\right], \tag{2.95}$$

and substitute it into eq. (2.93), yielding

$$\begin{aligned}\overline{W^2} =& \frac{\bar{I}^2}{\mathcal{A}_D^2} \iint_{-\infty}^{\infty} K_D(\Delta x, \Delta y)\, d\Delta x\, d\Delta y \\ &+ \frac{\bar{I}^2}{\mathcal{A}_D^2} \iint_{-\infty}^{\infty} K_D(\Delta x, \Delta y) |\mu_A(\Delta x, \Delta y)|^2\, d\Delta x\, d\Delta y\,.\end{aligned} \tag{2.96}$$

From eq. (2.94) one can see that $\iint_{-\infty}^{\infty} K_D(\Delta x, \Delta y)\, d\Delta x\, d\Delta y = \mathcal{A}_D$, which reduces the first term to $\overline{I^2}$. For the variance of W follows

$$\sigma_W^2 = \frac{\bar{I}^2}{\mathcal{A}_D^2} \iint_{-\infty}^{\infty} K_D(\Delta x, \Delta y) |\mu_A(\Delta x, \Delta y)|^2\, d\Delta x\, d\Delta y\,. \tag{2.97}$$

We can define a parameter

$$M = \left[\frac{1}{\mathcal{A}_D^2} \iint_{-\infty}^{\infty} K_D(\Delta x, \Delta y) |\mu_A(\Delta x, \Delta y)|^2\, d\Delta x\, d\Delta y\right]^{-1} \tag{2.98}$$

to write the speckle contrast with eq. (2.31) as

$$C = \frac{1}{\sqrt{M}}. \tag{2.99}$$

The physical interpretation of M can be better understood by separating the two functions $K_D(\Delta x, \Delta y)$ and $|\mu_A(\Delta x, \Delta y)|^2$ under the integral representing the detector pixel size and the speckle size, respectively. This can be conveniently done by considering two extreme cases, where the speckle size is narrow or wide compared to the detector pixel size. This implies that one function is significantly wider than the other and can be pulled out of the integral using the respective value

at $(\Delta x, \Delta y) = (0, 0)$. Starting with the case of very small speckles, M becomes

$$M = \left[\frac{K_D(0,0)}{\mathcal{A}_D^2} \iint_{-\infty}^{\infty} |\mu_A(\Delta x, \Delta y)|^2 \, d\Delta x \, d\Delta y \right]^{-1}, \tag{2.100}$$

where $K_D(0,0) = \iint_{-\infty}^{\infty} D^2(x_1, y_1) \, dx_1 \, dy_1$ follows from eq. (2.94). Assuming the detector is uniformly sensitive, meaning eq. (2.90) holds, $K_D(0,0)$ reduces to $\mathcal{A}_D$. The remaining factor in the integral is the autocorrelation function of intensity (see eq. (2.49)), whose result can be interpreted as the correlation area of a speckle $\mathcal{A}_c$,

$$\mathcal{A}_c = \iint_{-\infty}^{\infty} |\mu_A(\Delta x, \Delta y)|^2 \, d\Delta x \, d\Delta y \, . \tag{2.101}$$

Therefore we get for the parameter M

$$M \approx \frac{\mathcal{A}_D}{\mathcal{A}_c} \quad (\mathcal{A}_D >> \mathcal{A}_c). \tag{2.102}$$

With this result, the interpretation becomes more intuitive: M is the average number of speckles per detector pixel or the average number of speckles influencing the measurement in one pixel. In the second case with $\mathcal{A}_D << \mathcal{A}_c$ we find with $|\mu_A(0,0)|^2 = 1$,

$$M \approx \left[\frac{1}{\mathcal{A}_D^2} \iint_{-\infty}^{\infty} K_D(\Delta x, \Delta y) \, d\Delta x \, d\Delta y \right]^{-1} = 1 \quad (\mathcal{A}_D << \mathcal{A}_c). \tag{2.103}$$

We see that the parameter M can never fall below unity, and we conclude that at least one speckle will influence the measurement in a detector pixel. To determine M, the detector aperture function $D(x, y)$ and the intensity covariance function μ_A need to be specified. We will calculate an integral expression for two cases, starting with a uniform squared pixel of size $L_D \times L_D$ and a rectangular intensity pattern on the scattering medium of size $L_x \times L_y$. The detector aperture is modeled with

the rectangle function Π, by

$$D(x,y) = \Pi\left(\frac{x}{L_D}, \frac{y}{L_D}\right) = \Pi\left(\frac{x}{L_D}\right)\Pi\left(\frac{y}{L_D}\right). \tag{2.104}$$

The autocorrelation of the rectangle function is the triangle function Λ, yielding

$$\begin{aligned} K_D(\Delta x, \Delta y) = &\int_{\infty}^{\infty} \Pi\left(\frac{x_1}{L_D}\right)\Pi\left(\frac{\Delta x - x_1}{L_D}\right) dx_1 \\ &\times \int_{\infty}^{\infty} \Pi\left(\frac{y_1}{L_D}\right)\Pi\left(\frac{\Delta y - y_1}{L_D}\right) dy_1 \\ =&L_D^2 \Lambda\left(\frac{\Delta x}{L_D}\right)\Lambda\left(\frac{\Delta y}{L_D}\right) \end{aligned} \tag{2.105}$$

By invoking the *van Cittert-Zernike Theorem* one can determine the intensity covariance function μ_A as already demonstrated previously in section 2.2.5. Also, the presented geometry is adopted again. For the intensity distribution on the scattering spot, we have a 2D rectangle function:

$$I(\alpha, \beta) = \Pi\left(\frac{\alpha}{L_x}\right)\Pi\left(\frac{\beta}{L_y}\right). \tag{2.106}$$

The Fourier transform of a rectangle function is the sinc function, hence for the normalized correlation function we have

$$\mu_A(\Delta x, \Delta y) = \mathrm{sinc}(\Delta x L_x)\mathrm{sinc}(\Delta y L_y). \tag{2.107}$$

For the parameter M we can now write with eq. (2.98):

$$\begin{aligned} M =& \left[\frac{L_D^2}{L_D^4}\iint_{-\infty}^{\infty}\Lambda\left(\frac{\Delta x}{L_D}\right)\Lambda\left(\frac{\Delta y}{L_D}\right)\left|\mathrm{sinc}(\Delta x L_x)\mathrm{sinc}(\Delta y L_y)\right|^2 d\Delta x\, d\Delta y\right]^{-1} \\ =& L_D^2\left[\iint_{-L_D}^{L_D}\left(1-\left|\frac{\Delta x}{L_D}\right|\right)\left|\mathrm{sinc}(\Delta x L_x)\right|^2 d\Delta x\left(1-\left|\frac{\Delta y}{L_D}\right|\right)\left|\mathrm{sinc}(\Delta y L_y)\right|^2 d\Delta y\right]^{-1} \\ =& \left[\int_{-1}^{1}(1-|u_1|)\left|\mathrm{sinc}(u_1 L_D L_x)\right|^2 du_1\int_{-1}^{1}(1-|u_2|)\left|\mathrm{sinc}(u_2 L_D L_y)\right|^2 du_2\right]^{-1} \\ =& \left[2\int_0^1(1-u_1)\,\mathrm{sinc}^2(u_1 L_D L_x)\,du_1\, 2\int_0^1(1-u_2)\,\mathrm{sinc}^2(u_2 L_D L_y)\,du_2\right]^{-1}, \end{aligned} \tag{2.108}$$

where in the third step we have made the substitutions $u_1 = \Delta x/L_D$ and $u_2 = \Delta y/L_D$.

2.2.7 Angle and Wavelength Diversity

In this section, the correlation of speckle patterns is presented that are recorded with varying angles or illumination wavelengths. The discussion follows J. W. Goodman, 2020, chap. 6.3, pp. 188f for an imaging geometry in the reflection and transmission case, which are depicted in fig. 2.3. The scattering plane (α, β) is located just next to the diffuser in the downstream direction. A lens is placed a distance z away in the (ξ, η)—plane. The observation plane (x, y) is again positioned a distance z downstream. All planes are parallel.

We start with the discussion of the reflection case. The scattering diagram is shown in fig. 2.4. Light is originating from an average illumination direction $\hat{i}$ with a wave vector $\vec{k_i}$ of magnitude $|k| = 2\pi/\lambda$. It is incident on a finite scattering spot, which is small compared to the distance z. The scattered light emerges from the scattering plane $h(\alpha, \beta)$ and is observed from an average direction $\hat{o}$ having an analog wave vector $\vec{k_o}$. The angular range around the illumination and observation directions is considered small, for which the wave vectors describe the geometry sufficiently well. The phase shift due to the surface roughness $h(\alpha, \beta)$ can be

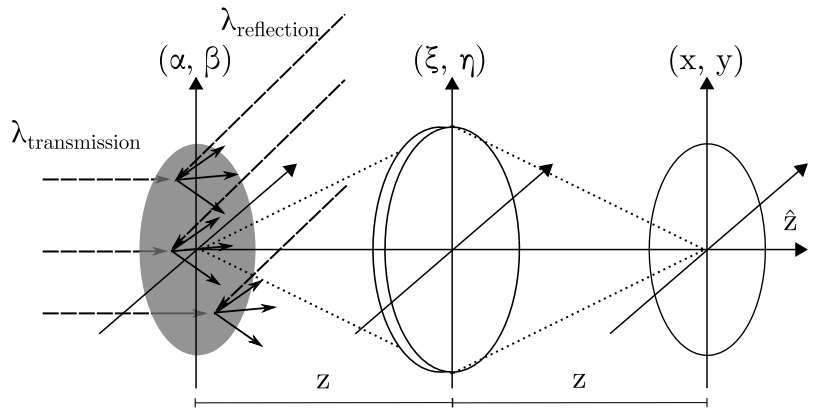

Figure 2.3: Imaging geometry showing both the transmission and reflection case. Scattered light emerging from plane (α, β) just downstream of the diffuser is imaged by a lens in the (ξ, η)—plane a distance z away. The observation plane (x, y) is located a distance z behind it. Adapted from J. W. Goodman, 2020.

expressed with

$$\phi(\alpha, \beta) = \left[\left(-\vec{k_i} + \vec{k_o}\right)\hat{z}\right] h(\alpha, \beta). \tag{2.109}$$

We define a scattering vector originally proposed by Parry, 1975 with

$$\vec{q} = \vec{k_o} - \vec{k_i} = q_\alpha \hat{\alpha} + q_\beta \hat{\beta} + q_z \hat{z} = \vec{q_t} + q_z \hat{z} \tag{2.110}$$

which can be split into a transverse and a normal component with respect to $\hat{z}$. Their magnitudes can be written as

$$|\vec{q_t}| = |k||\sin(\theta_o) - \sin(\theta_i)|, \tag{2.111}$$

$$q_z = |k||\cos(\theta_o) + \cos(\theta_i)|, \tag{2.112}$$

where θ_i and θ_o are the respective angles of the wave vectors subtended with surface normal $\hat{z}$. For the phase shift in eq. (2.109) follows

$$\phi(\alpha, \beta) = q_z h(\alpha, \beta). \tag{2.113}$$

The imaging system can be described by its point-spread function $\mathbf{k}(\alpha, \beta, x, y)$ (see

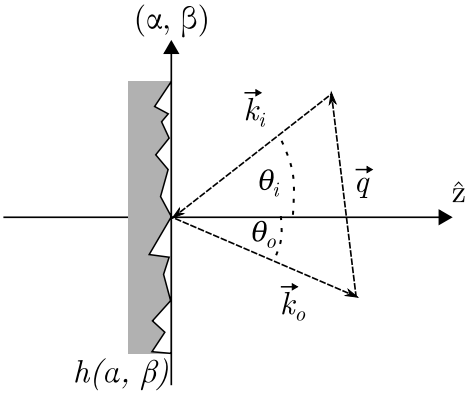

Figure 2.4: The scattering diagram in the reflection case. Light originating from an average illumination direction $\hat{i}$ is incident on a finite scattering spot in the (α, β)–plane just right to diffuser surface with an average wave vector $\vec{k_i}$. The scattered light with an average wave vector $\vec{k_o}$ is reflected in the observation direction $\hat{o}$. $\vec{q} = \vec{k_o} - \vec{k_i}$ is the scattering vector and $h(\alpha, \beta)$ denotes the surface roughness. θ_i and θ_o are the respective angles of the wave vectors subtended with the surface normal. Adapted from J. W. Goodman, 2020.

J. W. Goodman, 2017, p. 113)

$$\mathbf{k}(\alpha, \beta, x, y) = \frac{1}{\lambda^2 z^2} e^{j\frac{\pi}{\lambda z}\left(\alpha^2+\beta^2\right)} \iint_{-\infty}^{\infty} \mathbf{P}(\xi, \eta)\, e^{-j\frac{2\pi}{\lambda z}[\xi(\alpha+x)+\eta(\beta+y)]}\, d\xi\, d\eta\,, \tag{2.114}$$

where $\mathbf{P}(\xi, \eta)$ is the pupil function of the imaging lens. The field $\mathbf{a}(\alpha, \beta)$ at the diffuser surface is therefore related to the field at the observation plane by

$$\mathbf{A}(x, y) = \iint_{-\infty}^{\infty} \mathbf{k}(\alpha, \beta, x, y)\, \mathbf{a}(\alpha, \beta)\, d\alpha\, d\beta\,. \tag{2.115}$$

A quadratic phase term in $x^2 + y^2$ was dropped in eq. (2.114), since we are only interested in the intensity of the fields in the observation plane (x, y). Now we want to examine how two fields $\mathbf{A}_1(x_1, y_1)$ and $\mathbf{A}_2(x_2, y_2)$ change, if one or all of the following parameters are changed:

- wavelength of illumination λ,
- angle of illumination θ_i,
- and angle of observation θ_o.

The change can be quantified by the cross correlation

$$\Gamma_{\mathbf{A}}\left(x_1, y_1, x_2, y_2\right) = \overline{\mathbf{A}_1\left(x_1, y_1\right)\mathbf{A}_2^*\left(x_2, y_2\right)}, \tag{2.116}$$

where the variations in λ, θ_i, and θ_o are implicit. An explicit derivation of the following can be found in J. W. Goodman, 2020, Appendix D. The result is the normalized cross-correlation function μ_A given by

$$\mu_A\left(\Delta x, \Delta y\right) = \frac{\overline{\mathbf{A}_1\left(\Delta x, \Delta y\right)\mathbf{A}_2^*\left(\Delta x, \Delta y\right)}}{\sqrt{\overline{\left|\mathbf{A}_1\left(\Delta x, \Delta y\right)\right|^2}}\sqrt{\overline{\left|\mathbf{A}_2\left(\Delta x, \Delta y\right)\right|^2}}} = F\left(\Delta q_z\right)\Psi\left(\Delta x, \Delta y\right) \tag{2.117}$$

with

$$\Psi\left(\Delta x, \Delta y\right) = \frac{\iint_{-\infty}^{\infty}\left|\mathbf{P}\left(\xi, \eta\right)\right|^2 e^{-j\frac{2\pi}{\lambda_2 z}\left(\xi\Delta x + \eta\Delta y\right)}\, d\xi\, d\eta}{\iint_{-\infty}^{\infty}\left|\mathbf{P}\left(\xi, \eta\right)\right|^2 d\xi\, d\eta} \tag{2.118}$$

and

$$\Delta q_z = \left|\frac{2\pi}{\lambda_1}\left[\cos(\theta_{o1}) + \cos(\theta_{i1})\right] - \frac{2\pi}{\lambda_2}\left[\cos(\theta_{o2}) + \cos(\theta_{i2})\right]\right|. \tag{2.119}$$

F represents the characteristic function of the diffuser's effective surface height fluctuations and Ψ the geometric extent of a speckle in the observation plane. Both contributions need to be specified depending on the used diffuser and imaging system to enable any further calculations beyond this general expression, which will be done in later sections.

We continue with the transmission case. The overall result from above remains the same. The needed adjustments in the derivation ultimately influence only the scattering component q_z as will be shown in the following. Consider the scattering diagram in fig. 2.5 (a): light from an average direction $\hat{i}$ is incident on a scattering slab with refractive index n under an angle θ_i with the surface normal. Inside the diffuser, it is refracted in the direction $\hat{r}$ and emerges from the (α, β)–plane just right of the diffuser's surface from where it is observed in an average direction $\hat{o}$ having an angle θ_o with the surface normal. In this case, $h\left(\alpha, \beta\right)$ describes the cause of the phase shift the light suffers inside the diffuser. It can be intuitively thought of as an effective surface roughness like in the reflection case but is due to

a more complex process. In (b) the wave vectors of the incident and refracted light as well as the in the observation direction are depicted. For simplicity, we assume that all of them lie in the (β, z)–plane. The difference to the reflection geometry is that $\vec{k_i}$ and $\vec{k_o}$ point in the same half-space and $\vec{k_i}$ is transformed into $\vec{k_r}$ by Snell's law (see Hecht and Lippert, 2018, chap. 4.4.1). The continuity of the underlying fields requires that β (or surface parallel) components of both the incident and refracted wave vectors are equal, i.e. $\vec{k_i}\hat{\beta} = \vec{k_r}\hat{\beta}$. This increases the length of $\vec{k_r}$ in the $\hat{z}$–direction. Overall $\vec{k_r}$ is n times longer than $\vec{k_i}$ and $\vec{k_o}$, which have the magnitude $|k| = 2\pi/\lambda$, where λ is the free-space wavelength. We can write the phase shift as

$$\phi(\alpha, \beta) = |k| \left(-n\hat{r}\hat{z} + \hat{o}\hat{z}\right) h(\alpha, \beta) \tag{2.120}$$

and define a scattering vector

$$\vec{q} = \vec{k_o} - \vec{k_r} = \vec{q_t} + q_z\hat{z} \tag{2.121}$$

which again split up into a transverse and normal component. For the transverse component we have

$$\vec{q_t} = \left(\vec{k_o} - \vec{k_r}\right)_t = \left(\vec{k_o} - \vec{k_i}\right)_t, \tag{2.122}$$

where we have used the above mentioned continuity of the parallel components of the wave vectors on the refractive boundary. For the magnitude we get

$$|\vec{q_t}| = q_t = \frac{2\pi}{\lambda}\left[\sin(\theta_o) - \sin(\theta_i)\right]. \tag{2.123}$$

The normal component is given by

$$\begin{aligned} q_z &= k_{oz} - k_{or} = k_{oz} - \sqrt{k_r^2 - k_{r\alpha}^2 - k_{r\beta}^2} \\ &= k_{oz} - \sqrt{k_r^2 - k_{i\alpha}^2 - k_{i\beta}^2} = k_{oz} - |k|\sqrt{n^2 - \left(\hat{i}\hat{\alpha}\right)^2 - \left(\hat{i}\hat{\beta}\right)^2} \\ &= k_{oz} - \frac{2\pi}{\lambda}\sqrt{n^2 - \sin^2(\theta_i)} = \frac{2\pi}{\lambda}\left[\cos(\theta_o) - \sqrt{n^2 - \sin^2(\theta_i)}\right]. \end{aligned} \tag{2.124}$$

From this follows for the difference of the normal component of two fields $\mathbf{A}_1(x_1, y_1)$ and $\mathbf{A}_2(x_2, y_2)$

$$\Delta q_z = \left| \frac{2\pi}{\lambda_1} \left[\cos(\theta_{o1}) - \sqrt{n^2 - \sin^2(\theta_{i1})} \right] - \frac{2\pi}{\lambda_2} \left[\cos(\theta_{o2}) - \sqrt{n^2 - \sin^2(\theta_{i2})} \right] \right| \tag{2.125}$$

which is the final result. On a closing note, it is mentioned in J. W. Goodman, 2020 that in a simple imaging geometry, the contributions of the term Ψ can be neglected with respect to the discussed parameter changes. However, dispersive imaging spectrometers induce a wavelength-dependent lateral shift on the speckle patterns that can not be neglected. Also, to which extent angular changes may be insignificant in terms of Ψ should be carefully examined for a specific instrument's geometry.

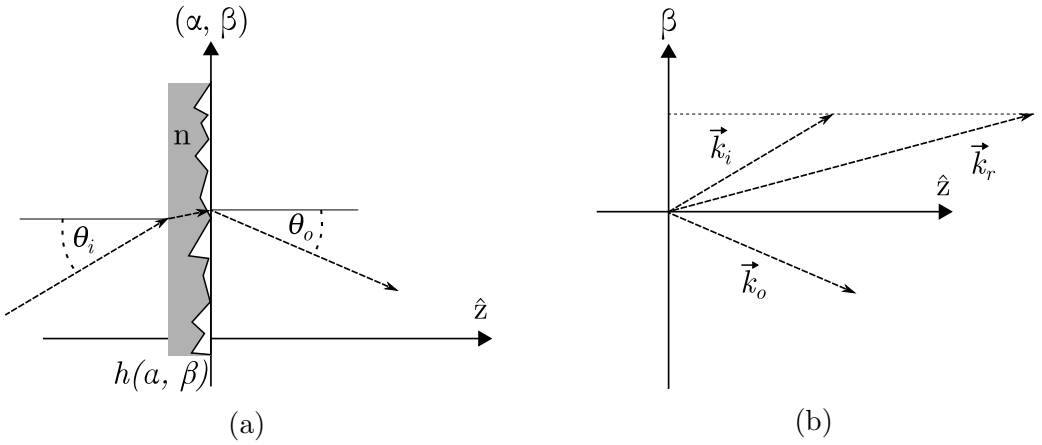

Figure 2.5: Scattering in the transmission case: (a) light originating from an average illumination direction $\hat{i}$ is incident on a finite scattering slab with refractive index n having an angle θ_i with the slab's normal. The ray is refracted in the direction $\hat{r}$ and emerges from the (α, β)–plane just right to diffuser's surface. The scattered light is observed from an average direction $\hat{o}$ under an angle θ_o with the diffuser normal. Again, $h(\alpha, \beta)$ denotes the effective surface roughness. (b) wave vectors of the incident and refracted light $\vec{k_i}$ and $\vec{k_r}$ as well as $\vec{k_o}$ in the observation direction. Adapted from J. W. Goodman, 2020.

2.3 Speckle Summation and Averaging in Imaging Spectrometers

In sections 2.2.2 to 2.2.4 and 2.2.6 several effects are discussed that can lead to a reduction of the speckle contrast C compared to fully developed speckles with unity contrast. The standardized measure to quantify the magnitude of the speckle impact is the *Spectral Features Amplitude* (SFA) Brug and Courrèges-Lacoste, 2007, which is mathematically equal to the speckle contrast C. It describes the amplitude of the features in the perceived spectrum that are solely caused by the diffuser. The features are due to a net speckle pattern that is integrated at the detector. Predicting the exact position of this pattern at the detector plane can be unreliable since it depends on various geometric conditions. Instead, it can be quantified by the speckle contrast introduced in section 2.2, eq. (2.31). In doing so no further knowledge about the positions of individual speckles is required. In fact, the contrast C at detector level can solely be determined by factoring in any relevant speckle averaging effects that reduce it from an initial value which is assumed to be unity as established in eq. (2.32). To every reduction effect one can assign an averaging factor $M_{1,2}$ which reduces a contrast C_1 to C_2 by

$$M_{1,2} = \frac{C_1^2}{C_2^2}. \tag{2.126}$$

It is well established and important to note that a contrast reduction can only be achieved if speckle patterns are summed on intensity basis and if they exhibit a correlation that is smaller than unity J. W. Goodman, 2007. Correlation can be understood as similarity. The summation of partially correlated and completely uncorrelated (independent) speckle patterns is discussed in previous sections. If, however, speckles are summed on amplitude basis, no reduction will take place. This is the case if individual speckle patterns can interfere. Therefore, it is sufficient to treat effects for which the underlying summation is on intensity basis for which only in this case the contrast or SFA is impacted.

Chapter 3

Measurement of Diffuser-Speckle

In this chapter, an experimental approach for quantifying the impact of speckles in an imaging spectrometer as an alternative to common representative end-to-end setups is presented. Compared to the latter method, it features several advantages: it can be adjusted to represent different instruments quickly, the experimental complexity is reduced, ensuring that only speckle contributions are measured, small speckle error amplitudes are detectable, and one is able to track the progression of the speckle statistics through the instrument. These advantages are the premises for a better understanding of the speckle effect and the development of the theoretical model in the following chapter. In section 3.1 the basic principle is explained. Afterward, the experimental means and procedures are shown in section 3.2 followed by a discussion about the mitigation of stray light and a constraint on the setup set by the diffuser illumination in section 3.3. In section 3.4 the image post-processing steps are described.

3.1 Experimental Approach

The measurement method to quantify the impact of Spectral Features in imaging spectrometers used in this work is based on the determination of speckle statistics at intermediate steps in the instrument (Burns et al., 2017; Richter et al., 2018), rather than just at the detector plane (Brug and Courrèges-Lacoste, 2007). This

allowed for the derivation of a comprehensive prediction model (Richter et al., 2021), which is presented later (chapter 4).

Figure 3.1 shows the optical setup of an imaging spectrometer during the solar calibration as described previously in section 1.1. Incoming Sunlight is scattered by a diffuser in transmission at the plane with spatial coordinates g and h, thereby homogeneously filling the aperture and field of view of the instrument. The scattered field distribution is imaged to the slit plane with spatial coordinates x and y by the telescope. Here, the slit cuts the image, and only light emerging from points within the slit aperture is collimated onto the dispersive element, such as a grating, separating its spectral components to different angles depending on the wavelength λ. The focusing lens converts the various angles to positions b at the detector plane. The relations between slit and detector plane coordinates are summarized by the simplified linear spectrometer equations given by Burns et al., 2017

$$a = M_x x, \tag{3.1}$$

$$b = M_y y + k\lambda, \tag{3.2}$$

where M_x and M_y are the magnification factors in the x- and y-direction, respectively, and $k = db\,/\,dy$ is the dispersion. A few assumptions are made by Burns et al. (2017) and Richter et al. (2021) that simplify the measurement but should not impact speckle related effects appreciably. First, the magnification factors in eqs. (3.1) and (3.2) as well as the dispersion are assumed constant with wavelength and spatial coordinates x and y. Further, the instrument point spread function is neglected. Finally, the Sun's light is spatially coherent, which allows the approximation of collimated light incident on the diffuser. Also, the Sun is considered to be a point source. At this point, an argumentation is anticipated regarding the treatment of the net speckle distribution in the slit and detector plane as a superposition of monochromatic speckle intensities (see Richter et al., 2021) and will be detailed in chapter 4. So far, we have discussed the general structure of an imaging spectrometer consisting of various optical components and the simplification made

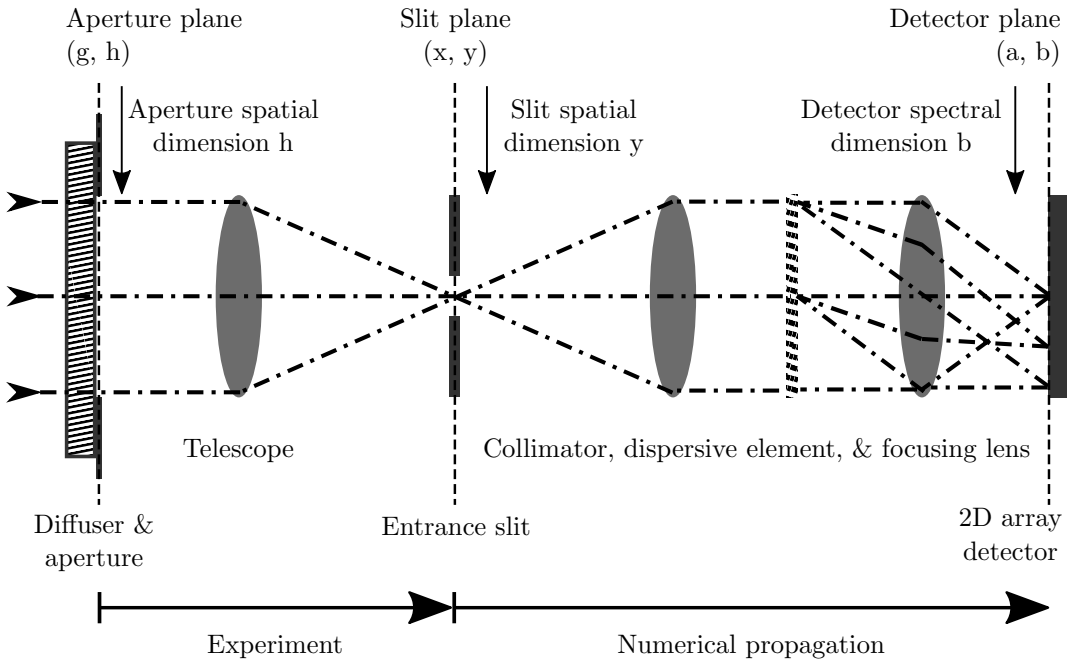

Figure 3.1: Optical setup of an imaging spectrometer during solar calibration. The sequence of optical components is subdivided into two parts. The first part is covered by the experimental setup in the lab, starting at the illuminated diffuser and ending at the slit in the telescope focal plane. The second part numerically propagates the images recorded in the slit plane to the instrument detector plane. Adapted from Richter et al., 2021.

for this measurement technique. Let us take a look at how this experimental approach reflects these components. The complete optical setup of an imaging spectrometer is mimicked by two separate parts, as illustrated in fig. 3.1. The first part is covered by the experiment in the lab ranging from the illuminated diffuser over the telescope to the entrance slit. The second part is a numerical simulation and consists of the optical components from the slit to the detector. The acquired data in the first part is used as input for the numerical propagation through the rest of the instrument. During the first part, monochromatic speckle intensities are recorded subsequently over a wavelength range $\lambda_1 ... \lambda_N$ at the slit plane (x, y). The spectral step size $\Delta\lambda$ needs to be sufficiently small in order to sample the changing speckle patterns appropriately. In chapter 4 it will be shown on the basis of the measured data that the respective sampling chosen for the measurements is adequate. Following the acquisition in the first part of the measurement chain,

the intermediate result is a three-dimensional data set $I_{slit}(x, y, \lambda)$ consisting of a spectrum of monochromatic speckle images. The speckle images are rescaled in order to properly match the optical system of the spectrometer that is being mimicked. This process is detailed in section 3.4. In fig. 3.2 (a) and (b) examples of measured speckle patterns are shown. In the numerical simulation, these speckle images are mapped to detector positions (a, b) and summed in intensity (Burns et al., 2017) with

$$I_{det}\,(a,b) = \frac{\Delta\lambda}{\lambda_{res}} \sum_{\lambda=\lambda_1}^{\lambda_N} I_{slit}\left(\frac{a}{M_x}, \frac{b-k\lambda}{M_y}\right) \Theta\,(b-k\lambda)\,\Theta\,(k\lambda_{res}-b+k\lambda)\,, \qquad (3.3)$$

where eqs. (3.1) and (3.2) are used to express slit plane coordinates as detector coordinates, $\Theta(y) = 0, y < 0$ and $\Theta(y) = 1, y \geq 0$, which is known as the Heaviside function, and λ_{res} is the spectral resolution of the instrument. The two Heaviside functions omit wavelengths greater and smaller than intended for a spectral detector coordinate b. The equation illustrates the limited amount of speckle intensities contributing to the sum at a single detector element. The result of the summation is a two-dimensional intensity distribution as illustrated in fig. 3.2 (c) and (d). Finally, $I_{det}\,(a, b)$ is integrated according to the instrument's detector pixel grid $(\tilde{a}, \tilde{b})$ which is depicted in fig. 3.2 (e) and (f). As described in section 2.3 the speckle averaging effects are of interest, which lead to different contrasts at intermediate steps in the measurement chain. There are three mechanisms to be accounted for according to Richter et al., 2021, for which averaging factors are defined in the following:

1. Depolarization of diffuse light generated by the diffuser given by

$$M_{polarization} = \frac{1^2}{\overline{c_{slit}}^2}, \qquad (3.4)$$

where the numerator is the initial contrast in the absence of any reduction, which is expected to be unity (see section 2.2.1) and $\overline{c_{slit}}$ is the average measured contrast in the slit plane determined from all recorded speckle

patterns $I_{slit}(x, y, \lambda)$ (see section 4.4 for details). Refer to section 3.4.3 for an explanation, why the actually measured contrast in the slit is not unity. This constant offset from unity, however, can be compensated for and does not change the final measurement result.

2. Spectral averaging due to the summation of speckle patterns using eq. (3.3) given by

$$M_{spectral} = \frac{\overline{c_{slit}}^2}{c^2_{spectral}}, \tag{3.5}$$

where $c_{spectral}$ is the measured contrast of the intensity distribution $I_{det}(a, b)$.

3. Integration of speckles with instrument detector pixel when applying the grid $(\tilde{a}, \tilde{b})$ yields the intensity distribution of the detector pixels $I_{det}\left(\tilde{a}, \tilde{b}\right)$ is given by

$$M_{detector} = \frac{c^2_{spectral}}{c^2_{detector}}, \tag{3.6}$$

where $c_{detector}$ is the measured contrast of $I_{det}\left(\tilde{a}, \tilde{b}\right)$.

At last, the measured SFA is calculated as the reduced speckle contrast by compounding the three averaging effects according to J. W. Goodman, 2007 as

$$SFA = \frac{1}{\sqrt{M_{polarization} M_{spectral} M_{detector}}}. \tag{3.7}$$

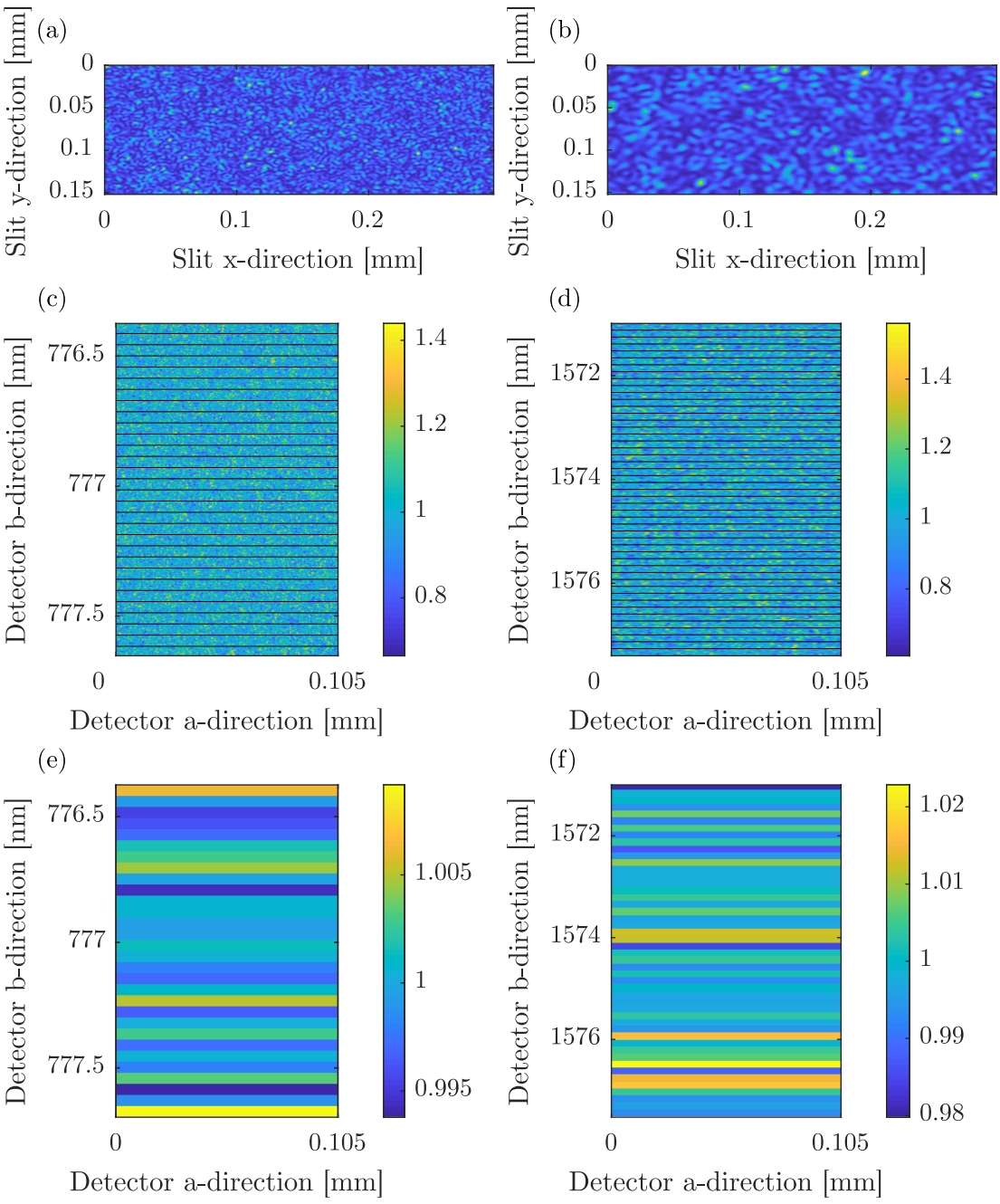

Figure 3.2: Speckle patterns in the NIR band (a, c, and e) and SWIR band (b, d, and f) at different stages in the measurement chain: (a/b) is an example of a monochromatic speckle pattern in the slit plane; (c/d) is the speckle pattern integrated at the detector plane using eq. (3.3) and normalized by the mean. Horizontal lines denote the instrument detector pixel grid $(\tilde{a}, \tilde{b})$, and (e/f) is the final normalized pixel integrated detector image. The standard deviation taken over the pixel rows is the SFA. Adapted from Richter et al., 2021.

3.2 Materials and Procedure

Measurements are performed for different wavelength bands that are commonly encountered in Earth observation missions, such as the visible band (VIS), the near-infrared band (NIR), and the short-wave-infrared band (SWIR) (Irizar et al., 2019; Meijer et al., 2019; Voors et al., 2017; Wenig et al., 2004). First, the materials that are used for all bands are presented; everything wavelength-specific is shown later. The measurement setup covering a spectrometer instrument from the diffuser to the entrance slit is depicted in fig. 3.3. A tunable external cavity diode laser with a narrow linewidth serves as a light source. A small portion of the laser light is tapped into a Fizeau interferometer, which spectrally stabilizes the laser via a proportional-integral-derivate (PID) feedback loop. All fiber connections are single-mode (SM) fibers, which can be used because the spectral tuning ranges are only a few nanometers. Also, SM fibers introduce no additional speckle contribution to their outputs in contrast to multi-mode fibers. A linear polarizer ensures polarization stability after the fiber output. The divergent laser beam illuminates the diffuser at normal incidence with respect to the diffuser plane, thereby overfilling it significantly (see section 3.3 for details on the illumination). The diffuser has a diameter of 70 mm and a thickness of 3 mm if not mentioned otherwise. It is made out of highly scattering fused silica HOD®-500 material featuring inhomogeneities of 20 µm or less. It has been selected for the Sentinel-5/UVNS instrument by Irizar et al., 2019 and is therefore deemed a suitable choice for the wavelengths used in this work. The power meter is illuminated by a representative portion of the divergent laser beam. The power readings are used to calibrate the acquired images in intensity, which is detailed in section 3.4. The round apertures control the size of individual speckle correlation areas. Aperture 2 blocks any unwanted angular contributions (see details in section 3.3). The telescope's focal length is $f_{tel} = 1100\,\mathrm{mm}$ and images the diffuse light onto a 2D array detector positioned in the focal plane. Note that the focal plane in fig. 3.3 represents the slit plane in fig. 3.1 and the diffuser plane is tilted by 10° with respect to aperture and slit planes

in order to ensure that only scattered light reaches the detector. The telescope is aligned perpendicular to the aperture and slit plane. Tables 3.1 to 3.3 shows the

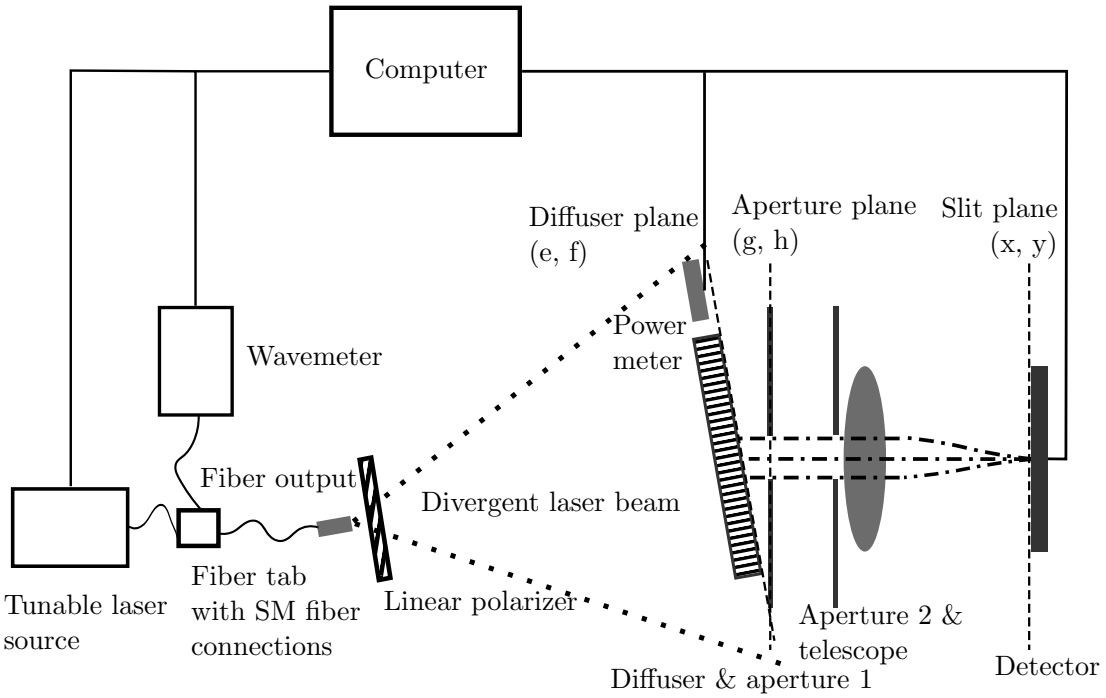

Figure 3.3: The layout of the experimental setup for measuring diffuser-induced monochromatic speckle patterns in the slit plane is depicted. The diffuser is illuminated with a divergent beam of monochromatic laser light out of a single-mode fiber. The laser source is spectrally stabilized with feedback from a wavemeter. The divergent beam is polarized by a linear polarizer. A portion of the beam is captured by a power meter for later intensity calibration. The speckle field originating from the diffuser is imaged by a telescope through two apertures onto a two-dimensional array detector. The diffuser plane is tilted with respect to the other planes in order to minimize specular light contributions at the detector. All components are controlled and synchronized via a computer. Adapted from Richter et al., 2021.

laser sources, detectors, and SM fiber types used in the measurements throughout this work for the NIR, SWIR, and VIS band, respectively, with a few important parameters. Note that the CCD camera is used for both the NIR and VIS bands. All other experimental parameters specific to a certain measurement such as the spectral tuning range $\lambda_1 ... \lambda_N$, the step size $\Delta\lambda$, the diameters of both apertures D, and the diffuser thickness d are given in the respective result section. The power of the laser sources needs to be adjusted so that the dynamic range of the respective

detector is utilized best without altering the to be measured speckle statistic in terms of the intensity and the speckle size. In the following, we derive the expected speckle intensity PDF in the slit plane. For that, we anticipate a result of section 4.3: the intensity in the slit plane I_{slit} is the sum of two independent speckle patterns, which we denote here by I_1 and I_2. They arise from the depolarization of the light by multi-scattering inside the volume diffuser. We assume unbiased scattering properties with respect to the two polarization components, which implies them having equal average intensities, i.e. $\overline{I_1} = \overline{I_2} = I_0$, and that $I_{slit} = I_1 + I_2$. Consider the PDF in eq. (2.38) describing the sum of N independent speckle patterns I_n with total intensity I_S and equal component mean $\overline{I_n} = I_0$. We set $I_S = I_{slit}$ and $N = 2$ for the case of the slit plane, which gives

$$f_{slit}\left(I_{slit}\right) = \frac{I_{slit}}{\Gamma(2) I_0^2} \exp\left(-\frac{I_{slit}}{I_0}\right) = \frac{I_{slit}}{I_0^2} \exp\left(-\frac{I_{slit}}{I_0}\right), \tag{3.8}$$

where the definition of the gamma function for positive integer arguments, $\Gamma\left(N\right) = \left(N-1\right)!$, is used. The probability that the speckle intensity exceeds the detector's dynamic range threshold I_t can be calculated with

$$P\left(I > I_t\right) = \frac{1}{I_0^2} \int_{I_t}^{\infty} I \exp\left(-\frac{I}{I_0}\right) dI = \left(1 + \frac{I_t}{I_0}\right) \exp\left(-\frac{I_t}{I_0}\right). \tag{3.9}$$

This implies that the average component intensity, which is given by $I_0 = \frac{\overline{I_{slit}}}{2}$, needs to be chosen as low as possible without diminishing the measured speckle contrast by a small signal-to-noise ratio. If the laser power is adjusted so that the average image intensity $\overline{I_{slit}}$ amounts to 25 % of the dynamic range of the detector I_t, then the chance of intensities not being properly recorded is 0.3 %. This condition is satisfied for all measurements.

Toptica Laser	Center λ	Tuning range	Line width
DL Pro 780	780 nm	765 nm...805 nm	6×10^{-7} nm
CTL 1550	1550 nm	1510 nm...1630 nm	2×10^{-6} nm
DL Pro HP461	460 nm	457 nm...461 nm	1×10^{-7} nm

Table 3.1: Laser sources used in this work with center wavelength, available tuning range, and typical line width according to the supplier.

Camera model	Detector type	Active area	Pixel size
Atik 460ex	CCD (Si)	2750 px × 2200 px	4.54 µm
Photonic Science	CMOS (InGaAs)	640 px × 512 px	15.5 µm

Table 3.2: Camera models used in this work with detector type, active area, and pixel size.

Fiber model	Operating λ	λ_{cutoff}	Core diam.	NA
Thorlabs 780HP	780 nm...970 nm	(730 ± 30) nm	4.4 µm	0.13
Thorlabs SMF-28-J9	1260 nm...1625 nm	1260 nm	8.2 µm	0.14
Thorlabs 460HP	450 nm...600 nm	(430 ± 3020) nm	2.5 µm	0.13

Table 3.3: Fiber types used in this work with operating wavelength range, cut-off wavelength, core diameter, and numerical aperture (NA) according to the supplier.

3.3 Straylight and Diffuser Illumination

The idea of the measurement setup, as shown in fig. 3.3, is to resolve individual speckle correlation areas with a camera in the slit plane. The recorded data is used as starting point for a numerical propagation of the monochromatic speckle patterns from the slit plane to a virtual detector plane of an instrument. The diffuse light is focused at the slit plane with a telescope featuring a long focal length of $f_{tel} = 1100\,\text{mm}$ and a clear aperture of $D_{tel} = 102\,\text{mm}$. A telescope is images objects from infinity, e.g. when they are far away, with a high f-number, which is $f/\# = \frac{f_{tel}}{D_{tel}} \approx 11$. This also means for the numerical aperture $NA \approx \frac{1}{2f/\#} = 0.1$ or an acceptance angle of $\alpha \approx 5°$. The spatial limitations in the laboratory only allow for distances between diffuser and telescope of about 300 mm. Due to its proximity, some light scattered by the diffuser may reach the telescope at angles exceeding its numerical aperture, which leads to light being scattered at part of the inner housing of the telescope. Those additional contributions appear as fine speckles at the focal plane. In an earlier study by Richter et al., 2018 the residuals are filtered using Fourier analysis of the recorded speckle patterns. For every acquired image, the higher frequency components of the power spectral density, which is well known for a given aperture (J. W. Goodman, 2007, p.77-79), is removed, leaving only frequencies that originated from the diffuser aperture. This approach involves additional post-processing of the acquired images, which may change the speckle statistics unintentionally. Thus, in this work, a different method is used. In order to block far off-axis scattering angles, two apertures are placed between diffuser and telescope, as proposed by Richter et al., 2021. The second aperture is placed directly upstream of the telescope lens, thereby a priori keeping stray light contributions from propagating to the focal plane. The effective aperture diameter determining the speckle size is the exit pupil (see J. W. Goodman, 2007, p. 82). Its size and position define the effective f-number of the telescope. The symmetry is illustrated in fig. 3.4: The apertures have a diameter d_1 and d_2, where the smaller sized one defines the exit pupil on the image side of the system (J. W. Goodman,

2017). For all measurement the condition $d_1 \leq d_2$ holds, which implies that the effective aperture size is $D = d_1$. First, knowing the exact size of the exit pupil

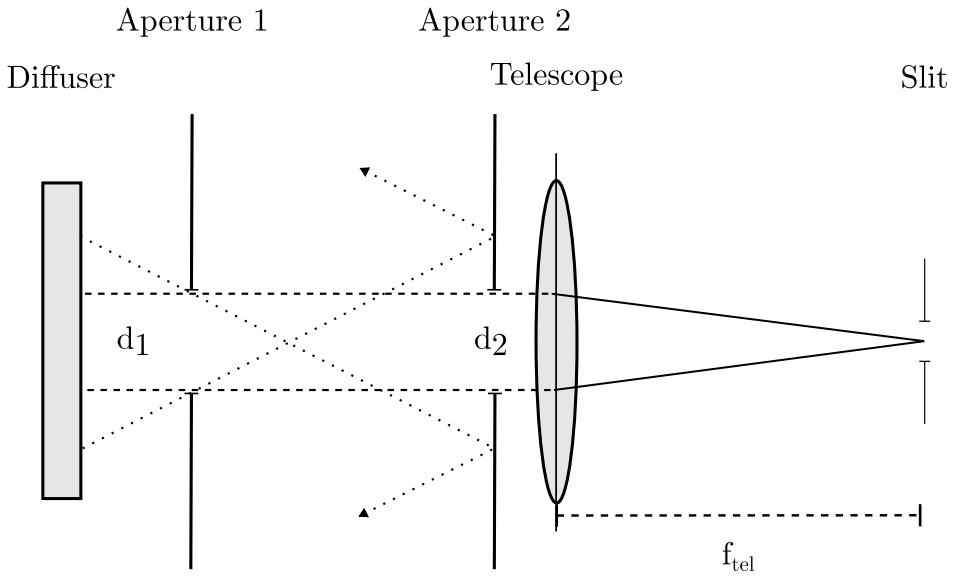

Figure 3.4: Geometry between the diffuser and the focal plane of the telescope is shown. The slit plane is located in the focal plane of the telescope; thus only rays parallel to the optical axis are imaged. The exit pupil on the imaging side is defined by a smaller diameter of d_1 and d_2. Angular contributions originating from far off-axis locations are blocked by aperture 2.

of the imaging system is important since it directly determines the size of the speckle correlation areas (see section 2.2.5). Secondly, the size of the scattering spot at the diffuser needs to be matched to the area of the diffuser, which can be assumed to be illuminated homogeneously by the divergent laser beam. In the following, the method used to determine the uniformity of the laser beams is presented. A power meter is placed on a translation stage a distance downstream from the fiber output, where normally the diffuser is positioned. The Gaussian beam originating from the single-mode fiber is centered on the power meter head, which has a round sensitive area with a diameter of 9.5 mm. The head is then successively translated perpendicularly to the optical axis by small steps of 0.1 mm. In this way, the transversal intensity profile $I(r)$ of the beam at the distance r from the optical axis is measured for all three laser sources used throughout this work. The results are depicted in figs. 3.5 to 3.7 for the VIS, NIR, and SWIR

laser source, respectively. The uniformity $U(D)$ over the aperture diameter D is characterized by the equation

$$U(D) = \frac{I(0) - I\left(\frac{D}{2}\right)}{\overline{I(r)}},\ 0 \leq |r| \leq \frac{D}{2}, \tag{3.10}$$

where it is assumed without loss of generality that the maximum intensity is centered at $r = 0$. Table 3.4 depicts the beam uniformities calculated with eq. (3.10) and the intensity profiles of figs. 3.5 to 3.7 for various aperture diameters. For a diameter up to 15 mm the assumption of uniform illumination of the diffuser is reasonably met. Diameters beyond 20 mm, especially in the SWIR case, should be avoided.

	$D = 10\,\text{mm}$	$D = 15\,\text{mm}$	$D = 20\,\text{mm}$	$D = 28\,\text{mm}$
$U_{VIS}(D)$	3.5 %	7.6 %	13.2 %	24.9 %
$U_{NIR}(D)$	3.5 %	7.5 %	13.0 %	23.2 %
$U_{SWIR}(D)$	2.8 %	8.5 %	17.4 %	31.0 %

Table 3.4: Calculated beam uniformities $U(D)$ from transversal intensity profiles $I(r)$ of figs. 3.5 to 3.7 for a distance downstream of the fiber output of 470 mm.

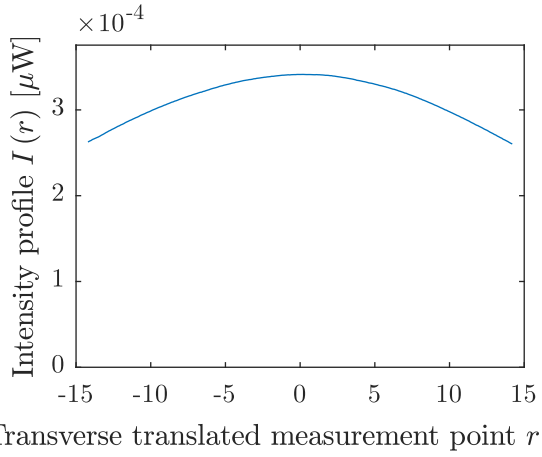

Figure 3.5: Measured beam intensity of the divergent VIS laser beam 470 mm after the fiber output at different positions perpendicular to the optical axis.

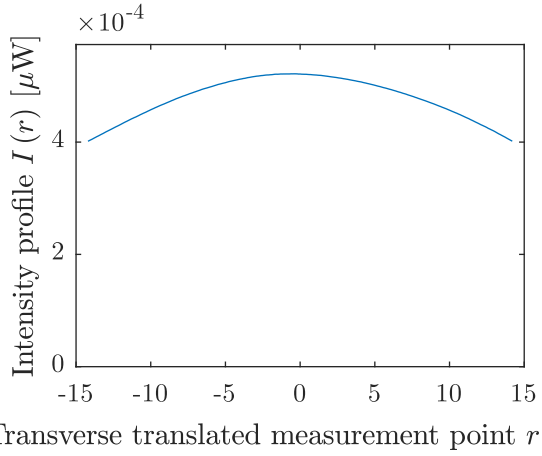

Figure 3.6: Measured beam intensity of the divergent NIR laser beam 470 mm after the fiber output at different positions perpendicular to the optical axis.

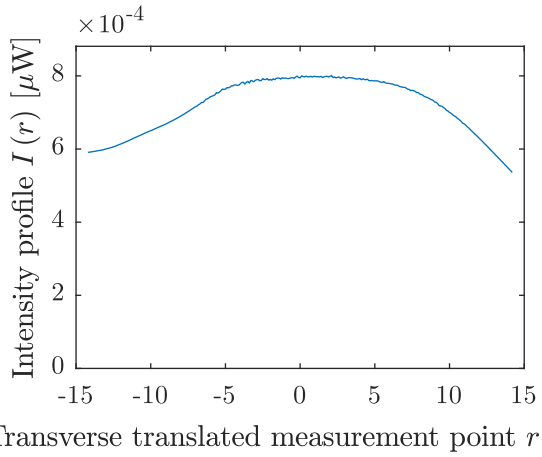

Figure 3.7: Measured beam intensity of the divergent SWIR laser beam 470 mm after the fiber output at different positions perpendicular to the optical axis.

3.4 Image Calibration Strategy

The intention of the measurement chain presented in this chapter is to simulate the speckle effect in a virtual imaging spectrometer. Consequently, the dimensions of the recorded images need to be matched in accordance with the optical parameters of the target instrument. Also, since the speckle effect is quantified relative to an otherwise constant mean intensity over the acquired spectrum, any systematic fluctuations between the measured speckle images need to be calibrated to minimize their contribution to the SFA result. In this section, the procedures, which deal

with those two aspects of the image post-processing, are presented.

3.4.1 Slit Image Scaling

For the appropriate resizing of the acquired speckle images, which serve as input for the numerical spectrometer propagation, the speckle extent L_c needs to be sized with respect to the instruments' slit dimensions. In section 2.2.5 it is shown that the speckle size in the slit plane depends on the f-number of the preceding imaging optics, which in this case, is defined by the aperture diameter D and the telescope focal length f_{tel}. With eq. (2.88) one can estimate the average speckle sizes of the measurement chain $L_{c,meas}$ and the virtual instrument $L_{c,instr}$ for a circular aperture. Let $W_{x,instr}$ and $W_{y,instr}$ denote the slit size of the instrument in x- and y-direction, then the dimensions of the sub-images are given by

$$W_{x,im} = L_{c,meas}\frac{W_{x,instr}}{L_{c,instr}}, \tag{3.11}$$

$$W_{y,im} = L_{c,meas}\frac{W_{y,instr}}{L_{c,instr}}. \tag{3.12}$$

Although it seems like that virtually, every configuration is possible as long as $W_{x,im}$ and $W_{y,im}$ do not exceed the pixel values of the recording camera, in reality, some limitations arise due to the finite pixel width of the recording cameras. For example, the target instrument features a dispersion k, which causes an offset between the speckle images at the detector plane Δb. The numerical propagation demands that this offset has an integer value corresponding to a complete pixel. Given the constant wavelength step size $\Delta\lambda$ and the fact that the slit width corresponds to the spectral resolution λ_{res} one can infer for the image height

$$W_{y,im} = \Delta b\frac{\lambda_{res}}{\Delta\lambda}.$$

This immediately defines $W_{x,im}$, too, because the aspect ratio of the entrance slit is conserved. Now, the speckle size needs to be adjusted so that it matches the

numerically constrained image dimensions. This can be achieved by tuning the aperture diameter D to an appropriate size or changing $\Delta\lambda$. In summary, the experimental parameters should be carefully evaluated before a measurement in order to minimize deviations from the optimal image dimensions.

3.4.2 Image Flat-Field Correction

In the following, the second step of the image post-processing is described, which aims at the equalization of the recorded data to the same mean intensity and the elimination of intensity structures introduced by the used detector or imaging system (Richter et al., 2018). Therefore, after the acquisition of the speckle images $I_{speckle}(\lambda_n)$ the same wavelength range is traversed again and a flat field or calibration image $I_{cal}(\lambda_n)$ is recorded. During the integration, the diffuser is translated and rotated simultaneously in order to average out the diffuser speckle. In doing so, only characteristics caused by the optical system of the measurement chain without the speckle contributions are selected. For every image on both runs the laser output power $P_{speckle}(\lambda_n)$ and $P_{cal}(\lambda_n)$ is recorded by the power meter, which are used to calibrate for laser power fluctuations caused by the wavelength tuning. After the calibration run 100 dark images are taken and averaged, yielding a noise-reduced background BG. The calibrated speckle image $I_{speckle,cal}$ is according to Richter et al., 2018, given by

$$I_{speckle,cal}(\lambda_n) = \frac{(I_{speckle}(\lambda_n) - BG)\, P_{cal}(\lambda_n)}{(I_{cal}(\lambda_n) - BG)\, P_{speckle}(\lambda_n)}. \tag{3.13}$$

3.4.3 Speckle Statistic in the Slit Plane

There is one important implication for the statistic of the speckle images that are recorded in the focal plane of the telescope, namely the slit plane. According to J. Goodman, 1975 the speckle field in the focal plane of an imaging lens does not follow circular Gaussian statistics since the otherwise complex pupil function becomes real-valued. This gives rise to a non-zero specular component at the point

where the optical axis of the imaging system meets the focal plane. This specular component effectively reduces the speckle contrast. In order to avoid recording this component in an actual spectrometer, the detector is usually positioned off-axis, which is also done for this setup. From speckle theory, the actual contrast for fully developed circular Gaussian speckle fields is known to be unity (see section 2.2.1), which allows for a simple compensation. Even without this effect, it is challenging to actually acquire speckle images with unity contrast since, for this intensity, values close to zero are needed, which is unrealistic for most detectors.

Chapter 4

Prediction Model for Diffuser-Speckle

In this chapter, a theoretical prediction model of the impact of diffuser speckle in imaging spectrometer is given. It can be understood as a mathematical representation of the measurement technique in chapter 3. The basic theoretical concepts of speckle are established in section 2.2. An introduction to the approach of quantifying the diffuser induced speckle effect in spectrometers is given in section 2.3. The goal of the prediction model is to determine the result of the measurement technique presented in chapter 3, namely eq. (3.7). Therefore, one needs to determine all three reduction factors $M_{polarization}$, $M_{spectral}$, and $M_{detector}$, which is presented in section 4.1. In section 4.2 a method to characterize the employed diffusers in this work is given. Finally, in section 4.3 the SFA results determined with the measurement chain (see chapter 3) are presented and compared to the prediction model.

4.1 Model Description

The SFA prediction model has been first introduced by Richter et al., 2021 and is presented in the following. At this point, let us recall that a contrast reduction can

only be achieved if speckle intensities are summed on intensity basis, that is, they can not interfere with each other, and that they show a correlation smaller unity (J. W. Goodman, 2007, Section 3.3.1). For each of the averaging factors, it will be shown that both conditions are met. In the following, all references to the optical setup of the spectrometer in question, including diffuser, slit, and detector planes, are depicted in fig. 3.1, section 3.1.

4.1.1 Polarization Averaging

The first reduction effect is due to *polarization averaging*. Sunlight has two orthogonal polarization states, which are incoherent (Hecht and Lippert, 2018, p. 656). The volume diffuser generates depolarized light due to multi scattering (Lorenzo, 2012, p. 85), which yields two equally strong independent speckle patterns for every polarization configuration per orthogonal state as shown in section 2.2.4. They can not interfere and are therefore summed on intensity basis. This yields a total of four independent contributions for Sunlight,

$$M_{polarization}^{(sun)} = 4. \tag{4.1}$$

Note that for measurements conducted in chapter 3 employing a laser source, there are only two independent speckle patterns (Richter et al., 2021), since a laser features only one polarization state. The monochromatic light incident on the diffuser is, again, depolarized when exiting it due to multi scattering, hence

$$M_{polarization} = 2. \tag{4.2}$$

4.1.2 Spectral Averaging

The finite bandwidth of the light, which is collected in the spectral channels of a spectrometer, is called spectral resolution and gives rise to *spectral averaging*. Consider a speckle intensity $I_n(x, y, \lambda_n)$ generated by the diffuser with monochro-

matic light at a wavelength λ_n in the slit plane (x, y) of the instrument. The underlying field $\mathbf{A}_n(x, y, \lambda_n)$ gives rise to the speckle intensity, and they are related by $I_n = |A_n|^2$, where A_n is the field amplitude. Now, the wavelength is changed gradually to λ_m, thus increasing the difference $\Delta\lambda_{n,m} = |\lambda_n - \lambda_m|$. As the wavelength changes so does the underlying field $\mathbf{A}_m(x, y, \lambda_m)$. In section 2.2.7 a general formulation of the cross-correlation function is given, which describes the relation between the two fields. It consists of two components, one of which is defined by the scattering properties of the diffuser denoted by F and one, which is given by the imaging system denoted by Ψ. In the following, both contributions are specified for the volume diffuser used throughout this work in transmission geometry. We start with the diffuser part. In the slit plane, the correlation is influenced by changing light paths through the diffuser medium at different wavelengths, which we will denote by $F(\lambda_n, \lambda_m)$. In order to model the correlation contribution, the approach by Zhu et al., 1991 is used. They presented an analytic equation for the wavelength correlation function in a slab geometry of a scattering media:

$$F(\lambda_n, \lambda_m) = \frac{(d+2B)/(z_0+B)\left[\sinh\left(z_0\sqrt{q^2+\alpha^2}\right) + B\sqrt{q^2+\alpha^2}\cosh\left(z_0\sqrt{q^2+\alpha^2}\right)\right]}{[1+B^2(q^2+\alpha^2)]\sinh\left(d\sqrt{q^2+\alpha^2}\right) + 2B\sqrt{q^2+\alpha^2}\cosh\left(d\sqrt{q^2+\alpha^2}\right)}, \tag{4.3}$$

where d is the thickness of the material, $q = \sqrt{i6\pi\left|\frac{1}{\lambda_n} - \frac{1}{\lambda_m}\right|\beta n_s/l_t}$ is the magnitude of the scattering vector, n_s denoting the refractive index of the scattering material, l_t the transport mean free path, and $\beta = \left|\cos(\theta_o) - \sqrt{n_s^2 - \sin^2(\theta_i)}\right|$ the in this case constant angular contribution from section 2.2.7, eq. (2.125) taking into account the tilted diffuser plane (e, f) with respect to the other planes. A method to determine the parameter l_t experimentally is shown in section 4.2. The symbol z_0 describes the average penetration depth after which the light is scattered for the first time. Since it does not have a great impact in a transmission geometry, it is approximated

with l_t. By setting $\alpha = 0$ absorption is ignored. The parameter for the boundary condition is given by $B = l_t \frac{2(1+R)}{3(1-R)}$, where R is the reflection coefficient which is calculated using the Fresnel equations (Zhu et al., 1991). It accounts for internal reflection due to index of refraction mismatch at the boundaries.

The speckle intensities in the slit plane (x, y) are imaged to the detector plane (a, b) using eqs. (3.1) and (3.2). Here, they are subject to a spatial offset in the b-direction induced by the dispersive element, which amounts to $\Delta b = k\Delta\lambda_{n,m}$. This contribution to the correlation is denoted as $\Psi(\Delta b)$ and is the second contribution to the cross-correlation of the two fields $\boldsymbol{A}_n$ and $\boldsymbol{A}_m$ discussed in section 2.2.7:

$$\Psi(\Delta a, \Delta b)|_{\Delta a=0} = \left. \frac{\int_{-\infty}^{\infty} |P(g,h)|^2 \, e^{-i\frac{2\pi}{\lambda z}(g\Delta a + h\Delta b)} dg\, dh}{\int_{-\infty}^{\infty} |P(g,h)|^2 \, dg\, dh} \right|_{\Delta a=0}, \tag{4.4}$$

where $P(g, h)$ is the aperture function of the imaging system. For a circular aperture of diameter D, the result from eq. (2.88) can be used to get for a one-dimensional offset immediately

$$\Psi(0, k\Delta\lambda_{n,m}) = 2\frac{J_1\left(\frac{\pi D}{\overline{\lambda_{n,m}} f_{tel} M_y} k\Delta\lambda_{n,m}\right)}{\frac{\pi D}{\overline{\lambda_{n,m}} f_{tel} M_y} k\Delta\lambda_{n,m}}, \tag{4.5}$$

where J_1 is the Bessel function of first kind, first order, $\overline{\lambda_{n,m}}$ is the mean of the neighboring wavelengths involved, and f_{tel} is the focal length of the telescope. It is established in section 2.2.7, eq. (2.117) that the "magnitude of change" between individual speckle fields can be described by the first order field correlation. In the current case it depends on wavelengths λ_n and λ_m,

$$\begin{aligned} \mu_{n,m}(\lambda_n, \lambda_m) &= \frac{\overline{\boldsymbol{A}_n(x, y, \lambda_n)\, \boldsymbol{A}_m^*(x, y, \lambda_m)}}{\sqrt{\overline{I_n(x, y, \lambda_n)}\,\overline{I_m(x, y, \lambda_m)}}} \\ &= F(\lambda_n, \lambda_m)\, \Psi(0, k\Delta\lambda_{n,m}) \end{aligned} \tag{4.6}$$

where in the second step eqs. (4.3) and (4.5) are used. The symbol $*$ denotes the complex conjugate. $\mu_{n,m}$ is related to the correlation on intensity basis $\rho_{n,m}$ by

eq. (2.49). The accumulation of a number of N speckle intensities $I_n\left(\frac{a}{M_x}, \frac{b-k\lambda_n}{M_y}\right)$ per spectral channel at the detector plane is given by

$$I_{det}\left(a,b\right) = \sum_{n=1}^{N=\lambda_{res}/\Delta\lambda} I_n\left(\frac{a}{M_x}, \frac{b-k\lambda}{M_y}, \lambda_n\right). \tag{4.7}$$

Similarly, for the average detector intensity, we have

$$\overline{I_{det}} = \sum_{n=1}^{N=\lambda_{res}/\Delta\lambda} \overline{I_n}. \tag{4.8}$$

The correlations between the speckle intensities in the sum are given by $\mu_{n,m}\left(\lambda_n, \lambda_m\right)$, which allows the description with the formalism presented in section 2.2.3. The entries $\boldsymbol{J}_{n,m} = \overline{\boldsymbol{A}_n \boldsymbol{A}_m^*}$ of the coherency matrix $\underline{\mathcal{J}}$ are given by

$$\boldsymbol{J}_{n,m} = \sqrt{\overline{I_n}\,\overline{I_m}}\mu_{n,m}, \tag{4.9}$$

where eq. (4.6) is used, $n, m = 1...N$, and spatial positions are in terms of detector coordinates. After the diagonalization of $\underline{\mathcal{J}}$, the eigenvalues $\overline{\tilde{I}_n}$ are used to calculate the spectral averaging factor

$$M_{spectral} = \left(\frac{\overline{I_{det}}}{\sigma_{det}}\right)^2 = \frac{\left(\sum_{n=1}^{N} \overline{\tilde{I}_n}\right)^2}{\sum_{n=1}^{N} \overline{\tilde{I}_n}^2}. \tag{4.10}$$

In the following, the limit of very small spectral sampling steps $\Delta\lambda$ is discussed, which represents the case of a continuous spectrum. Two aspects need to be considered. First, is the accumulation of speckle patterns in eq. (4.17) on intensity basis and second, is $M_{spectral}$ independent of spectral sampling $\Delta\lambda$? An argument for the latter is given by Richter et al., 2021, which cite a property of the coherency matrix $\underline{\mathcal{J}}$ called *Toeplitz*. A Toeplitz matrix shows an asymptotic behavior of its eigenvalues (Grenander and Szegö, 1958). One can see that by decreasing the spectral sampling one increases the number summations N in eq. (4.7), and thus

in eq. (4.10), as well as the size of the coherency matrix $\underline{\mathcal{J}}$. (Gray, 2006) gives proof of the fact that both, the numerator and denominator in eq. (4.10) converge for large N. Richter et al., 2021 also show that the summation is on intensity basis by invoking the short temporal coherence of sunlight Δt_{sun}, which is on the order of femtoseconds (Hecht and Lippert, 2018) in comparison to the substantially greater integration time Δt_{int} of a realistic detector, which is on the order of microseconds or higher. The resultant intensity of two speckle fields $\mathbf{A}_n(\lambda_n)$ and $\mathbf{A}_m(\lambda_m)$ perceived by a detector is the time average of the underlying fields given by

$$\langle I_{det,nm}\rangle_{\Delta t_{int}} = |A_n|^2 + |A_m|^2 + 2\langle \mathrm{Re}\{\mathbf{A}_n\mathbf{A}_m^*\}\rangle_{\Delta t_{int}} \tag{4.11}$$

The coherence term $2\langle \mathrm{Re}\{\mathbf{A}_n\mathbf{A}_m^*\}\rangle_{\Delta t_{int}}$ is an oscillatory beat which varies on the order of Δt_{sun}. Thus, in good approximation, contributions by this term average out,

$$\langle \mathrm{Re}\{\mathbf{A}_n\mathbf{A}_m^*\}\rangle_{\Delta t_{int}} \to 0, \quad \frac{\Delta t_{sun}}{\Delta t_{int}} \to 0,$$

which implies a summation of monochromatic speckle patterns on intensity basis (see also George and Jain, 1974). A similar argument by Caron, 2020 can be made using a property of the diffuser. Its correlation function F approaches zero for large wavelength shifts $\Delta\lambda_{nm}$,

$$\lim_{\Delta\lambda_{nm}\to\infty} F(\lambda_n, \lambda_n + \Delta\lambda_{nm}) = 0. \tag{4.12}$$

Let us define a wavelength shift $\Delta\lambda_{decorr}$, for which the correlation falls to a value of e^{-3},

$$F(\lambda_n, \lambda_n + \Delta\lambda_{decorr}) = e^{-3}, \tag{4.13}$$

which we call *spectral decorrelation length*. Strictly speaking, it is itself wavelength dependent, because the width of F is coupled to the mean free path length $l_t(\lambda)$, which in turn is anti-proportional to the scattering cross-section, $l_t \sim 1/\sigma^{(t)}$ (see Bertolotti, 2007, p. 29). However, in the following it is assumed, that $\Delta\lambda_{decorr}$ is appreciably constant over the width of the spectral resolution λ_{res}. Let us consider

two waves with different wavelengths separated by $\Delta\lambda_{coh}$. The coherence between them is bound to the condition (Hecht and Lippert, 2018)

$$c\frac{\Delta\lambda_{coh}}{\overline{\lambda}^2}\Delta t_{coh} \lesssim 1, \tag{4.14}$$

where $\overline{\lambda}$ is the average wavelength of the two waves, c is the speed of light, and Δt_{coh} is the coherence time. For a realistic integration time of $\Delta t_{int} = 1\,\mu s$ and a wavelength of $\overline{\lambda} = 1\,\mu m$ the wavelength shift required to violate this coherence condition is

$$\Delta\lambda_{coh} \lesssim \frac{\overline{\lambda}^2}{c\Delta t_{int}} \approx 4 \times 10^{-6}\,nm \tag{4.15}$$

Let us discuss three cases of the finite spectral sampling $\Delta\lambda$:

$\Delta\lambda < \Delta\lambda_{coh}$ Wavelength shifts smaller than $\Delta\lambda_{coh}$ lead to a summation on amplitude basis,

$\Delta\lambda_{coh} < \Delta\lambda < \Delta\lambda_{decorr}$ for wavelength shifts greater than $\Delta\lambda_{coh}$ the summation is on intensity basis but with no appreciable decorrelation,

$\Delta\lambda_{decorr} < \Delta\lambda$ summation is on intensity basis and speckle intensities are decorrelated.

We have already established, a summation on amplitude basis can not reduce speckles and therefore needs no further attention. In fact, only the third case has a significant impact on the speckle contrast. As a consequence, for a continuous spectrum, we need no infinitely dense sampling for F. Instead, we can derive one from the cases above and the sampling theorem (Jähne et al., 1999, section 2.4.2) to be

$$\Delta\lambda = \frac{\Delta\lambda_{decorr}}{2}. \tag{4.16}$$

4.1.3 Detector Averaging

The third averaging effect occurs at the detector plane (a, b). Here, the individual speckle patterns are summed to a net intensity denoted by $I_{det}(a, b)$ in eq. (4.7). As

a final step, the instrument detector integrates this speckle pattern by summation of all intensities within a detector pixel. The pixel grid is denoted by $\left(\tilde{a}, \tilde{b}\right)$ and gives rise to *detector averaging*. The principle of this speckle reduction effect is detailed in section 2.2.6. In summary, the average speckle size compared to a detector pixel determines the number of speckles that are averaged per pixel. The analytic expression for the detector averaging factor for stationary speckle in a detector pixel with relative coordinates $(\Delta a, \Delta b)$ is given by

$$M_{detector} = \left[\frac{1}{A_D^2} \iint_{-\infty}^{\infty} K_D\left(\Delta a, \Delta b\right) \left|\mu_{det}\left(\Delta a, \Delta b\right)\right|^2 d\Delta a \; d\Delta b \right]^{-1}, \tag{4.17}$$

where A_D is the area of a detector pixel, $K_D\left(\Delta a, \Delta b\right)$ is the autocorrelation function of the detector pixel, and $\mu_{det}\left(\Delta a, \Delta b\right)$ is the correlation of the speckle field at the detector plane. An intuitive approximation for the common case in a spectrometer is a speckle correlation area $\mathcal{A}_c$ much smaller than the pixel area A_D:

$$M_{detector} \approx \frac{A_D}{\mathcal{A}_c} \quad A_D \gg \mathcal{A}_c. \tag{4.18}$$

Key for the correct calculation is the determination of the speckle correlation function μ_{det} which determines the speckle size. Therefor, one needs to consider how this size evolves during the summation in eq. (4.7). For the following explanation refer to fig. 4.1. It is instructive to think about a single correlation area $\mathcal{A}_c$ of respective 1D sizes L_a and L_b in the detector plane centered at coordinates (a_n, b_n). The spatial correlation relative to this position is given by eq. (4.4),

$$\Psi\left(\Delta a, \Delta b\right) = \frac{\int_{-\infty}^{\infty} \left|P\left(g,h\right)\right|^2 e^{-i\frac{2\pi}{\lambda z}\left(g\Delta a + h\Delta b\right)} \, dg \, dh}{\int_{-\infty}^{\infty} \left|P\left(g,h\right)\right|^2 dg \, dh}, \tag{4.19}$$

with $\Delta a = a - a_n$ and $\Delta b = b - b_n$ being relative coordinates, as before. We have established previously that the spatial distribution of a speckle pattern decorrelates after a spectral shift of λ_{decorr}. An equal statement would be that a single speckle correlation area can only persist within one length of this spectral

interval. Therefore, the speckle correlation area "exists" at the detector plane of the instrument at every intermediate position between the coordinates (a_n, b_n) and $(a_n, b_n + k\lambda_{decorr})$ simultaneously and is summed by the detector. This effectively elongates the speckle in the spectral direction. Thus, we can write the intensity correlation function $|\mu_{det}|^2$ as a symbolic convolution of the geometric speckle size $|\Psi|^2$ with diffuser correlation function $|F|^2$:

$$|\mu_{det}(\Delta a, \Delta b)|^2 = |\Psi(\Delta a, \Delta b)|^2 \circledast |F(\lambda_n, \lambda_m)|^2, \tag{4.20}$$

where $\circledast$ denotes the convolution operation.

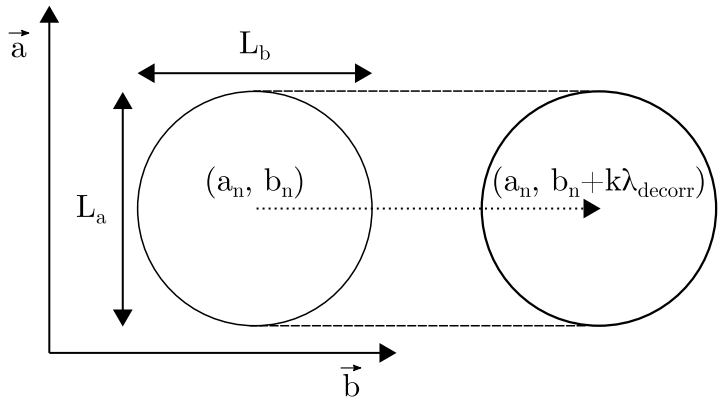

Figure 4.1: Schematic illustration of the elongation of the speckle correlation function μ_{det} due to the instrument's dispersion k at the detector plane (a, b).

4.2 Diffuser Characterization

The diffusers used in this work play an integral part in all conducted measurements. In the previous section 4.1 an approach by Zhu et al., 1991 is shown that gives a relation, $F(\lambda_n, \lambda_m)$, between the fields of speckle patterns $\mathbf{A}_n(x, y, \lambda_n)$ and $\mathbf{A}_m(x, y, \lambda_m)$ for neighboring wavelengths λ_n and λ_m by eq. (4.3) in the slit plane (x, y). An intuitive interpretation of the diffuser function F is, that it constitutes a measure of the diffuser's sensitivity to wavelength change. In other words, it tells us how fast a speckle pattern changes spectrally. Apart from the wavelength and the thickness d of the diffuser the key parameter is the transport mean free path

$l_t(\overline{\lambda})$, which depends on the scattering cross-section of the material and is therefore wavelength dependent. It is the typical distance after which the initial direction of the light is completely randomized due to anisotropic scattering (Bertolotti, 2007). $l_t(\overline{\lambda})$ is determined for the following parameters:

- $\lambda = 776\,\mathrm{nm}$; $d = 3\,\mathrm{mm}$,
- $\lambda = 1572\,\mathrm{nm}$; $d = 3\,\mathrm{mm}$,
- $\lambda = 460\,\mathrm{nm}$; $d = 0.5\,\mathrm{mm}$,
- $\lambda = 460\,\mathrm{nm}$; $d = 1.0\,\mathrm{mm}$,
- $\lambda = 460\,\mathrm{nm}$; $d = 2.0\,\mathrm{mm}$.

The three latter results in the VIS range are used in section 5.2. A speckle field $\mathbf{A}_n$ is related to the measured intensity by $I_n = |A_n|^2$. With this relation we can use the Pearson correlation $\rho_{Pearson}\left(I_n(\lambda_n), I_m(\lambda_m)\right)$ between recorded speckle intensities $I_n(\lambda_n)$ and $I_m(\lambda_m)$ to find a measure for F by

$$\begin{aligned} \left|F\left(\lambda_n, \lambda_m\right)\right|^2 &\sim \rho_{Pearson}\left(I_n(\lambda_n), I_m(\lambda_m)\right) \\ &= \frac{\sum_i \sum_j \left(I_{n,ij} - \overline{I_n}\right)\left(I_{m,ij} - \overline{I_m}\right)}{\sqrt{\left(\sum_i \sum_j \left(I_{n,ij} - \overline{I_n}\right)^2\right)\left(\sum_i \sum_j \left(I_{m,ij} - \overline{I_m}\right)^2\right)}}, \end{aligned} \tag{4.21}$$

where i, j are image pixel indices, $n, m = 1...N$ and N is total amount of images used for the calculation. The explicit wavelength dependency is dropped on the right-hand side. The similarity is justified with eq. (2.49). In figs. 4.2 to 4.5 the averaged measurement points are represented as blue stars. The error bars are omitted, because the error of the mean is smaller than 0.5 % thus too small to be displayed. The red graph is a fit to eq. (4.3) with the desired mean free path length l_t as parameter. The results are depicted in table 4.1. The manufacturer of the HOD®-500 diffuser material gives an additional value with $l_t\,(500\,\mathrm{nm}) = 56\,\mu\mathrm{m}$ with an unspecified thickness (Heraeus Conamic, 2021). The measured values are in

good agreement with this specification except for thicknesses below 2 mm, for which there seems to be an effect, which reduces l_t beyond the wavelength dependence.

Parameters (λ, d)	l_t
776 nm, 3 mm	(59.3 ± 0.4) µm
1572 nm, 3 mm	(67.8 ± 0.5) µm
460 nm, 0.5 mm	(21.5 ± 0.4) µm
460 nm, 1.0 mm	(38.8 ± 0.3) µm
460 nm, 2.0 mm	(51.0 ± 0.5) µm

Table 4.1: Experimentally determined transport mean free path parameter l_t for different diffuser thicknesses and illumination wavelengths conducted with the measurement setup presented in chapter 3. It depends on the thickness of the diffuser and the illumination wavelength. It is the typical distance after which the initial direction of the light is completely randomized due to anisotropic scattering (Bertolotti, 2007).

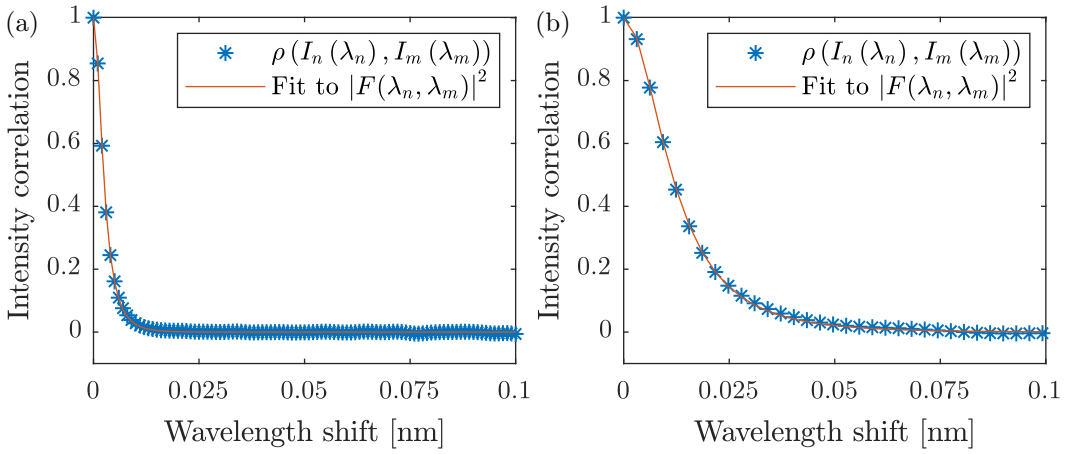

Figure 4.2: Measurement of the correlation function $|F\left(\lambda_n, \lambda_m\right)|^2$ for a 3 mm thick diffuser in (a) the NIR (776 nm) and (b) the SWIR band (1571 nm). Blue stars denote the measured Pearson correlations between speckle patterns $I_n(\lambda_n)$ and $I_m(\lambda_m)$. All wavelength shift combinations up to 0.1 nm are averaged for 120 images. Error bars are omitted, because the standard error of the mean value is too small to be displayed. The red graph denotes the fit of the measured data points to eq. (4.3) with (a) $l_t(\bar{\lambda}) = (59.3 \pm 0.4)\,\mu\text{m}$ and (b) $l_t(\bar{\lambda}) = (67.8 \pm 0.5)\,\mu\text{m}$. Adapted from Richter et al., 2021.

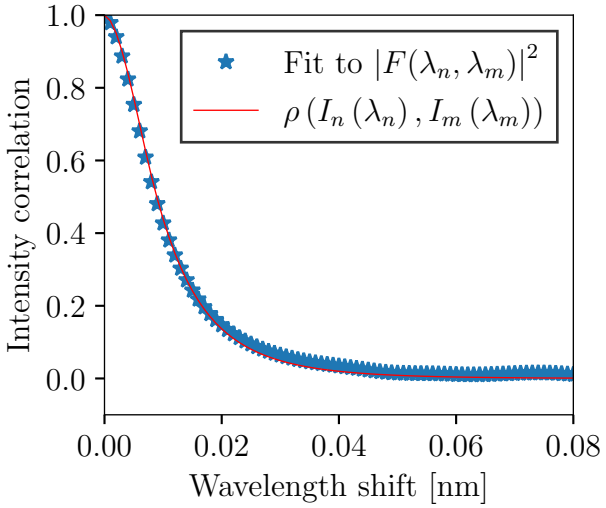

Figure 4.3: Measurement of the correlation function $|F\left(\lambda_n, \lambda_m\right)|^2$ for a 0.5 mm thick diffuser at 460 nm. Blue stars denote the measured Pearson correlations between speckle patterns $I_n(\lambda_n)$ and $I_m(\lambda_m)$. All wavelength shift combinations up to 0.08 nm are averaged for 21 images. Error bars are omitted, because the standard error of the mean value is below 0.5 % and therefore too small to be displayed. The red graph denotes the fit of the measured data points to eq. (4.3) with (a) $l_t(\bar{\lambda}) = (21.5 \pm 0.4)\,\mu\text{m}$.

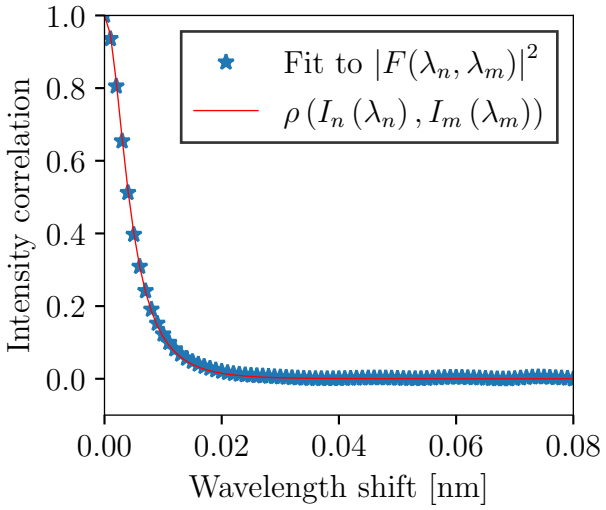

Figure 4.4: Measurement of the correlation function $|F\left(\lambda_n, \lambda_m\right)|^2$ for a 1.0 mm thick diffuser at 460 nm. Blue stars denote the measured Pearson correlations between speckle patterns $I_n(\lambda_n)$ and $I_m(\lambda_m)$. All wavelength shift combinations up to 0.08 nm are averaged for 81 images. Error bars are omitted, because the standard error of the mean value is below 0.5 % and therefore too small to be displayed. The red graph denotes the fit of the measured data points to eq. (4.3) with (a) $l_t(\bar{\lambda}) = (38.8 \pm 0.3)\,\mu\text{m}$.

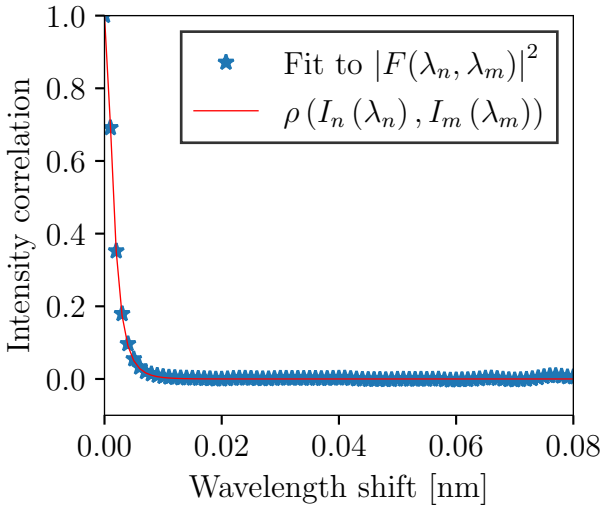

Figure 4.5: Measurement of the correlation function $|F\left(\lambda_n, \lambda_m\right)|^2$ for a 2.0 mm thick diffuser at 460 nm. Blue stars denote the measured Pearson correlations between speckle patterns $I_n(\lambda_n)$ and $I_m(\lambda_m)$. All wavelength shift combinations up to 0.08 nm are averaged for 81 images. Error bars are omitted, because the standard error of the mean value is below 0.5 % and therefore too small to be displayed. The red graph denotes the fit of the measured data points to eq. (4.3) with (a) $l_t(\bar{\lambda}) = (51.0 \pm 0.5)\,\mu\text{m}$.

4.3 Results and Comparison to Measurement

In this section, the results by Richter et al., 2021 of the SFA measurements conducted in the manner described in chapter 3 are presented and compared to the results of the SFA prediction model presented in this chapter. The basis for the experiment and the model are parameters representing a proposed spectrometer instrument for the CO2 Monitoring mission by the European Space Agency (see Meijer et al., 2019) depicted in table 4.2. The values for the refractive index $n_s(\lambda)$ of the diffuser material (fused silica) are calculated using the dispersion formula by Malitson, 1965. In section 4.2 the determination of the diffuser parameter l_t is detailed. The experimental parameters used for the measurements are displayed

Parameter	**Value**
Magnification M_x	0.34
Magnification M_y	0.30
Aperture diameter	40.0 mm
Slit dimensions (x, y–direction)	295 µm, 152 µm
Detector dimensions (a, b–direction)	105 µm, 45 µm
Detector pixel size	15 µm
Telescope focal length f	131 mm
Diffuser thickness d	3 mm
NIR specific	
Spectral resolution λ_{res}	0.128 nm
Average wavelength $\overline{\lambda}$	777.1 nm
Refractive index of diffuser material $n_s(\overline{\lambda})$	1.454
Mean free path $l_t(\overline{\lambda})$	(59.3 ± 0.4) µm
SWIR specific	
Spectral resolution λ_{res}	0.4 nm
Average wavelength $\overline{\lambda}$	1574.25 nm
Refractive index of diffuser material $n_s(\overline{\lambda})$	1.444
Mean free path $l_t(\overline{\lambda})$	(67.8 ± 0.5) µm

Table 4.2: The sample spectrometer parameters that are used for the measurement and prediction are shown. They were chosen to represent a proposed instrument for ESA's CO2M mission (Meijer et al., 2019). Adapted from Richter et al., 2021.

in table 4.2 for both bands. The spectral tuning range needs to be as wide as possible in order to reduce statistical uncertainties. However, the measurement quality also suffers from systematic time-dependent influences such as temperature

fluctuations. This effectively limits the tuning range. Both effects are discussed in section 4.4. Comparing the tuning step size $\Delta\lambda$ with fig. 4.2 in section 4.2, one can see that the change of the recorded speckle patterns with wavelength denoted by the diffuser correlation function F is sampled appropriately. The diameter D of the round apertures are chosen to achieve an optimum between detector signal and sampling of the speckle patterns. Using eq. (2.88) to calculate the average speckle size in the slit plane of the measurement chain with the telescope focal length $z = f_{tel}$ and the average wavelengths $\overline{\lambda}$ yields 96 µm and 150 µm for the NIR and SWIR bands, respectively. Comparing the expected speckle sizes with the employed detector pixel dimensions of 4.5 µm and 15.5 µm reveals that the speckles are sampled in one dimension with approximately 20 pixel in the NIR and 10 pixel in the SWIR band, which seems sufficient since detector averaging effects become significant if the speckle sizes are approx equal to the detector pixel size or smaller (see section 2.2.6). Figures 4.6 and 4.7 depict a comparison between the

Parameter	**NIR**	**SWIR**
Spectral tuning range $\lambda_1 ... \lambda_N$	776.4 nm...777.7 nm	1571 nm...1577.5 nm
Tuning step size $\Delta\lambda$	1 pm	3.1 pm
Diameter of apertures D	10 mm	13 mm

Table 4.3: Experimental parameters for the measurement setup presented in chapter 3.

measured and the predicted speckle correlation function μ_{det} at the detector plane for the NIR and SWIR band. They show very good agreement. In the spatial direction, the function follows the diffraction-limited Bessel function introduced in section 2.2.5. In the spectral direction, however, the correlation is elongated due to the dispersion of the instrument. In the following, the three speckle averaging factors $M_{polarization}$, $M_{spectral}$ and $M_{detector}$ as determined by Richter et al., 2021 are given using the SFA prediction model as presented in the previous section and compared to their counterparts determined with the SFA measurement chain. The values are depicted in table 4.4. The measurement and the prediction show good agreement within the margin of the 1σ uncertainty. The thorough discussion

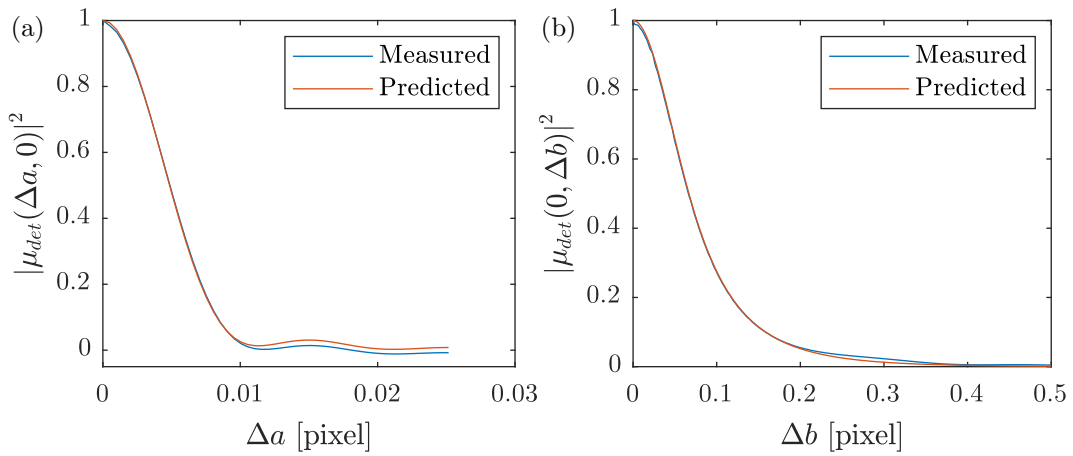

Figure 4.6: Cross-section of the detector correlation function $|\mu_{det}|^2$ in the NIR band for (a) the spatial dimension and (b) the spectral dimension. The blue lines represent the measured correlations; the red lines the predicted ones.

regarding the subjects of uncertainties can be found in the following section 4.4. The measured values are obtained by comparing the speckle contrast levels at different stages in the virtual instrument's measurement process. $M_{polarization} = 2$ is verified by placing a linear polarizer after the diffuser. The measured contrast in the slit plane rises by the factor of $1/\sqrt{2}$. Rotating the polarization axis without changing the measured contrast confirms that the light exiting the diffuser is, in fact, depolarized. $M_{spectral}$ is determined by comparing the average contrast in the slit plane $\overline{c_{slit}}$ with the one of the accumulated intensity at the detector before the pixel integration $c_{spectral}$ by using eq. (2.126)

$$M_{spectral,meas} = \frac{\overline{c_{slit}}^2}{c^2_{spectral}}. \tag{4.22}$$

$M_{spectral}$ can be interpreted as the number of independent speckle patterns present in one spectral channel due to its bandwidth. The total number of speckle patterns incident on the detector is equal to the product of $M_{spectral}$ and $M_{polarization}$. Similarly, the averaging factor due to detector pixel aperture is calculated as,

$$M_{detector,meas} = \frac{c^2_{spectral}}{c^2_{detector}}. \tag{4.23}$$

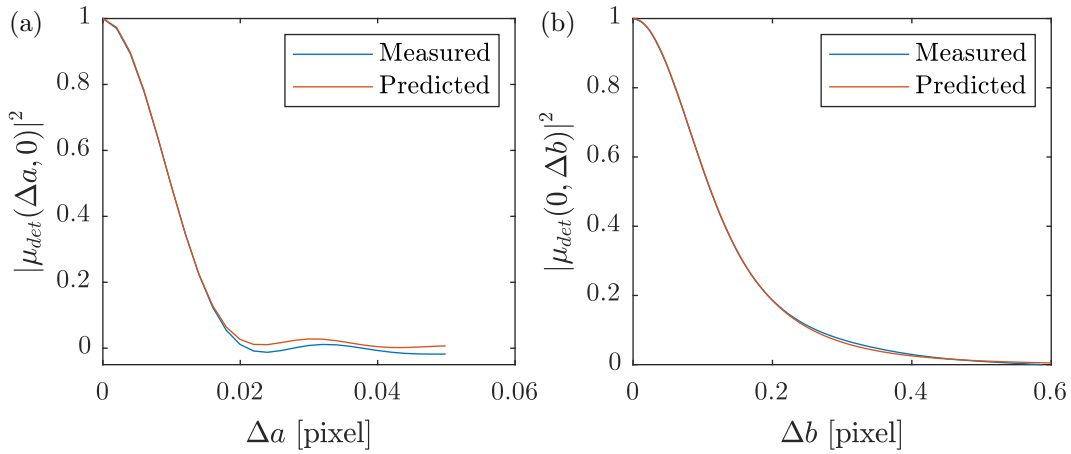

Figure 4.7: Cross-section of the detector correlation function $|\mu_{det}|^2$ in the SWIR band for (a) the spatial dimension and (b) the spectral dimension. The blue lines represent the measured correlations; the red line the predicted ones.

$M_{detector}$ is the number of speckles contributing to the measurement in a pixel. For details on the calculations of the contrast levels above, refer to section 4.4. From the results presented, it becomes clear that the SFA is higher for longer wavelengths because the diffuser's decorrelation wavelength becomes smaller, i.e., its' sensitivity to wavelength change gets smaller, resulting in less independent speckle patterns. Also, the geometric size of speckle scales with wavelength (see eq. (2.88)) decreasing the number of speckles per detector pixel and thus reducing detector averaging. The only constant contribution can be expected by polarization. The value for $M_{polarization}$ may be different for other diffusers and geometries if the scattered light is not depolarized entirely. Figure 4.8 depicts the SFA scaling with wavelength over the representative spectral region for a CO2I like instrument (Meijer et al., 2019), which is the subject of the study by Richter et al., 2021 using the prediction model in the NIR and SWIR band. Linear scaling with the simplified assumptions about the underlying instrument, such as the wavelength-independent dispersion k and magnifications M_x and M_y, over the spectral range in question seems to be a good approximation. Note that the SFA value calculated with the presented model for a specific wavelength is only valid for a small spectral bandwidth around it. Otherwise, the wavelength scaling effects can not be considered constant anymore.

Type	$M_{polarization}$	$M_{spectral}$	$M_{detector}$	SFA [%]
Measurement NIR	2	55.9 ± 0.6	$(6.1 \pm 1.8) \times 10^2$	0.38 ± 0.08
Prediction NIR	2	56.5	5.7×10^2	0.39
Measurement SWIR	2	29.9 ± 0.6	$(1.7 \pm 0.5) \times 10^2$	0.99 ± 0.21
Prediction SWIR	2	30.0	1.8×10^2	0.96

Table 4.4: Comparison of the SFA results from the measurement chain with the prediction model from Richter et al., 2021. The measurement uncertainties are given in the 1σ interval.

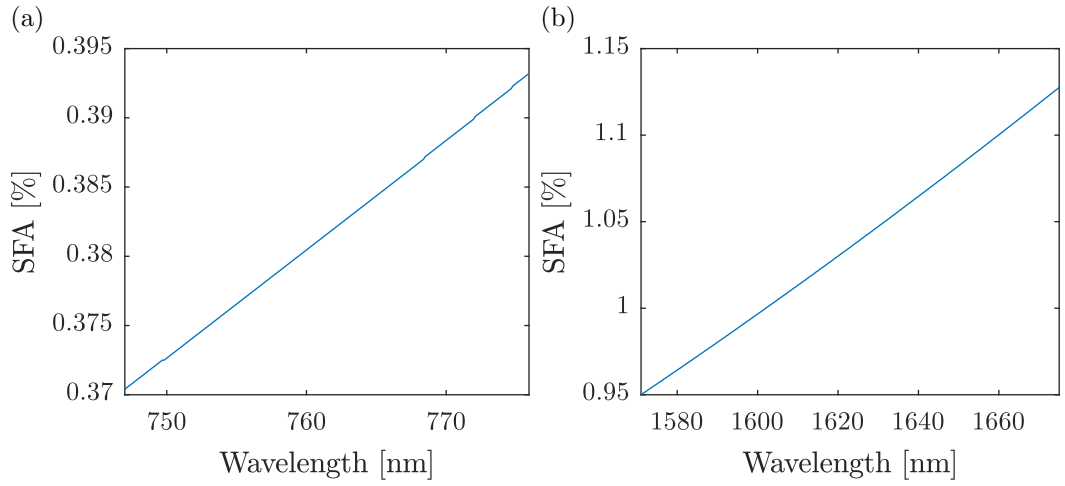

Figure 4.8: Scaling of the SFA with wavelength of a CO2I like instrument in the (a) NIR and (b) SWIR band using the prediction model. For both bands the scaling with wavelength can be approximated as linear. Adapted from Richter et al., 2021.

4.4 Discussion of Measurement Uncertainties

In this section, the calculation of uncertainties of the averaging factors, which are calculated with the measurement chain introduced in chapter 3 is presented. Two different approaches to determining the errors are shown, both of which cover distinct aspects of the measurement. The first approach is a rigorous Gaussian error propagation starting with fluctuations of contrast and intensity between images in the data set. The second approach uses the prediction model shown in the previous sections to quantify the impact of fluctuations in the functions that directly contribute to averaging factors. These fluctuations are then propagated with a Monte Carlo method.

4.4.1 Gaussian Error Propagation

This section describes the Gaussian error propagation of uncertainties between individual speckle images. The speckle contrast level c_i for every recorded image I_i is determined by

$$c_i = \frac{\sigma_i}{\overline{I_i}} = \frac{\sqrt{\frac{1}{N_{pixel}-1}\sum_{h=1}^{N_{pixel}}\left(I_{i,h}-\overline{I_i}\right)^2}}{\frac{1}{N_{pixel}}\sum_{h=1}^{N_{pixel}} I_{i,h}}, \tag{4.24}$$

where $\overline{I_i}$ and σ_i are the mean value and the standard deviation of I_i, respectively, and each image consists of N_{pixel}. The average speckle contrast in the slit is calculated by taking the mean over all individual image contrasts,

$$\overline{c_{slit}} = \frac{1}{N_{images}} \sum_{i=1}^{N_{images}} c_i, \tag{4.25}$$

where N_{images} is the number of images. The error of the average contrast $\overline{c_{slit}}$ is estimated as the standard error of the mean estimator (Ahn and Fessler, 2003). Hence,

$$\Delta\overline{c_{slit}} = SE_{\overline{c_{slit}}} = \frac{\sigma_{c_{slit}}}{\sqrt{N_{images}}}, \tag{4.26}$$

where $\sigma_{c_{slit}} = \left(\frac{1}{N_{images}-1}\sum_{i=1}^{N_{images}}\left(c_i - \overline{c_{slit}}\right)^2\right)^{1/2}$ is the standard deviation of the image contrasts, hence, the uncertainty for the contrast of a single image. In a next step $\overline{c_{slit}}$ is compared to the measured contrast $c_{spectral}$ of the intensity distribution accumulated at the detector plane $I_{spectral}$, given by

$$c_{spectral} = \frac{\sigma_{spectral}}{\overline{I_{spectral}}}. \tag{4.27}$$

In analogy to $\sigma_{c_{slit}}$ the uncertainties for the standard deviation and mean intensity of a single image σ_{σ_i} and $\sigma_{\overline{I_i}}$, respectively, are estimated by taking the standard deviation over the image series,

$$\sigma_{\sigma_i} = \sqrt{\frac{1}{N_{images}-1}\sum_{i=1}^{N_{images}}\left(\sigma_i - \overline{\sigma}\right)^2}, \tag{4.28}$$

$$\sigma_{\overline{I_i}} = \sqrt{\frac{1}{N_{images}-1}\sum_{i=1}^{N_{images}}\left(\overline{I_i} - \overline{I}\right)^2}, \tag{4.29}$$

where $\overline{I}$ and $\overline{\sigma}$ are the average mean and standard deviation over all images. Then the uncertainty for $\sigma_{spectral}$ and $\overline{I_{spectral}}$ is taken as

$$\Delta\sigma_{spectral} = \frac{\sigma_{\sigma_i}}{\sqrt{N_{res}}} \tag{4.30}$$

$$\Delta\overline{I_{spectral}} = \frac{\sigma_{\overline{I_i}}}{\sqrt{N_{res}}}, \tag{4.31}$$

where $I_{spectral}$ is composed out of N_{res} images. $N_{res} = \lambda_{res}/\Delta\lambda$ is the amount of images taken with a sampling $\Delta\lambda$ for a spectral interval equal to the spectral resolution λ_{res} of the instrument. For the contrast uncertainty it follows

$$\Delta c_{spectral} = c_{spectral}\sqrt{\left|\frac{\Delta\sigma_{spectral}}{\sigma_{spectral}}\right|^2 + \left|\frac{\Delta\overline{I_{spectral}}}{\overline{I_{spectral}}}\right|^2}. \tag{4.32}$$

The averaging factor $M_{spectral}$ is given by

$$M_{spectral} = \frac{\overline{c_{slit}}^2}{c_{spectral}^2}. \tag{4.33}$$

The uncertainty of the first approach for $M_{spectral}$ is therefore

$$\begin{aligned}
\frac{\Delta M_{spectral}^{(Gauss)}}{M_{spectral}} &= \frac{1}{M_{spectral}} \sqrt{\left| \frac{\partial M_{spectral}}{\partial \overline{c_{slit}}} \Delta \overline{c_{slit}} \right|^2 + \left| \frac{\partial M_{spectral}}{\partial c_{spectral}} \Delta c_{spectral} \right|^2} \\
&= \frac{1}{M_{spectral}} \sqrt{\left| \frac{2\overline{c_{slit}}}{c_{spectral}^2} \Delta \overline{c_{slit}} \right|^2 + \left| \frac{-2\overline{c_{slit}}^2}{c_{spectral}^3} \Delta c_{spectral} \right|^2} \\
&= \sqrt{\left| 2\frac{\Delta \overline{c_{slit}}}{\overline{c_{slit}}} \right|^2 + \left| 2\frac{\Delta c_{spectral}}{c_{spectral}} \right|^2}
\end{aligned} \tag{4.34}$$

For the uncertainty of the speckle contrast at the detector level, there is no direct access to the component uncertainties as there is for the previously stated contrasts. Therefore, the statistical uncertainty is calculated using the error of the standard deviation estimator (Ahn and Fessler, 2003) as

$$\frac{\Delta c_{detector}}{c_{detector}} \approx \frac{\Delta \sigma_{detector}}{\sigma_{detector}} = \frac{1}{\sqrt{2\left(N_{detector} - 1\right)}}, \tag{4.35}$$

where $N_{detector}$ is the number of detector pixels for the calculation of $c_{detector}$. For the approximation, it is used that $\frac{\Delta \sigma_{detector}}{\sigma_{detector}} \gg \frac{\Delta \overline{I_{detector}}}{\overline{I_{detector}}}$. Similar to eq. (4.34) the uncertainty of the first approach for the corresponding averaging factor $M_{detector}$ is then given by

$$\frac{\Delta M_{detector}^{(Gauss)}}{M_{detector}} = \sqrt{\left| 2\frac{\Delta c_{spectral}}{c_{spectral}} \right|^2 + \left| 2\frac{\Delta c_{detector}}{c_{detector}} \right|^2}. \tag{4.36}$$

4.4.2 Monte Carlo Error Propagation

This section describes the an alternative error propagation using Monte Carlo methods. In the previous section 4.4.1 the uncertainties for both averaging factors are derived by comparing a large amount of acquired images. This method,

however, does not take into account effects on pixel level within single images, because one image consists of a large amount of pixel. The uncertainties on pixel level are estimated indirectly by calculating fluctuations in those functions that mathematically contribute to $M_{spectral}$ and $M_{detector}$ (see Richter et al., 2021). From chapter 4 we know that the spatial speckle extent L_c, given by Ψ, and the diffuser correlation function, given by F, are the governing factors. For a subset of $\lambda_{res}/\Delta\lambda \approx 120$ images contributing to a single spectral channel, the average speckle size is determined by numerically calculating the width of the autocorrelation function, which is proportional to $L_{c,n}$ with $n \in \{1...120\}$, yielding a measure of the average fluctuations of Ψ, $\Delta L_c = \sigma_{L_{c,n}}$. The variations in F are estimated by using eq. (4.21) to calculate $\rho_{Pearson}\left(I_n(\lambda_n), I_m(\lambda_m)\right) \equiv \rho_{n,m}$ with $n, m \in \{1...120\}$. In a Monte Carlo simulation normal distributed random values are drawn from $\mathcal{N}\left(\overline{\rho_{n,m}}, \sigma_{\rho_{n,m}}\right)$ and $\mathcal{N}\left(\overline{L_{c,n}}, \sigma_{L_{c,n}}\right)$. They are taken as an input to calculate $M_{spectral}$ and $M_{detector}$ several thousand times (see eqs. (4.7), (4.9), (4.10), (4.17), (4.19) and (4.20)). In a final step the contribution given by the sampling of the detector intensity by a limited amount of pixel $N_{detector}$ (see eq. (4.35)) is estimated. On this account, we use the fact that the detector intensity is normal distributed with $\mathcal{N}\left(\mu = 1, \sigma = SFA\right)$ due to the addition of many speckle patterns, which individually follow a negative exponential distribution, but together, according to the Central Limit Theorem, approach a Normal distribution (see J. W. Goodman, 2020, section 3.3.3, p.51). From the normal distributed detector intensity a random sample $I_{detector}\left(N_{detector}\right)$ of size $N_{detector}$ is drawn. $M_{detector}\left(N_{detector}\right)$ is then calculated by using eq. (2.126) as

$$M_{detector}\left(N_{detector}\right) = \frac{c^2_{spectral}}{c^2_{detector}\left(N_{detector}\right)}, \tag{4.37}$$

where $c_{detector}\left(N_{detector}\right) = \frac{\sigma_{I_{detector}(N_{detector})}}{I_{detector}(N_{detector})}$. Figure 4.9 shows the resulting distribution of occurrences from 50 000 repetitions for $M_{spectral}$ and $M_{detector}$ with both an infinitely large pixel sample and one corresponding to the actual measurement in the NIR band. The average variations $\sigma_{\rho_{n,m}}$ in F are determined

to be 1.5 % and $\sigma_{L_{c,n}} = 1.3\,\%$ for Ψ. The results are, again, normal distributed with $\mathcal{N}\left(\mu = 56.6, \sigma = \Delta M^{(MC)}_{spectral} = 0.7\right)$ and $\mathcal{N}\left(\mu = 5.8 \times 10^2, \sigma = 0.1 \times 10^2\right)$ for $M_{spectral}$ and $M_{detector}$ in case of many pixels, respectively. In the case of the 30 pixels used in the actual measurement the distribution becomes significantly wider and asymmetric towards the upper flank. This can be explained with the inverse square dependency of eq. (4.37), which allows only for positive outliers and the proximity of the mean value to zero. The mean value shifts to $\mu\left(N_{detector}\right) = 6.4 \times 10^2$ and the standard deviation is calculated as $\sigma\left(N_{detector}\right) = \Delta M^{(MC)}_{detector} = 1.8 \times 10^2$. For the SWIR band after 50 000 runs with uncertainty parameters $\sigma_{\rho_{n,m}} = 2.5\,\%$ and $\sigma_{L_{c,n}} = 2.7\,\%$ the resulting normal distributions are $\mathcal{N}\left(\mu = 30.2, \sigma = \Delta M^{(MC)}_{spectral} = 0.6\right)$ for $M_{spectral}$ and $\mathcal{N}\left(\mu = 1.88 \times 10^2, \sigma = 0.04 \times 10^2\right)$ for $M_{detector}$. Again, in the case of an limited amount of pixels the similar behavior as in the NIR case is seen: the mean value shifts to $\mu\left(N_{detector}\right) = 2.0 \times 10^2$ and the standard deviation is calculated as $\sigma\left(N_{detector}\right) = \Delta M^{(MC)}_{detector} = 0.5 \times 10^2$. The described method of quantifying the impact on the measurement result indirectly accounts for any error contributors like pointing instabilities, detector noise, temperature fluctuations, if they have an influence on either F or Ψ. Conversely, if they do not impact these functions, they need no further consideration. The SFA scales with wavelength, since F or Ψ do (see section 4.3). This implies that the uncertainties estimated with the Monte Carlo approach also reflect this scaling over a wavelength range.

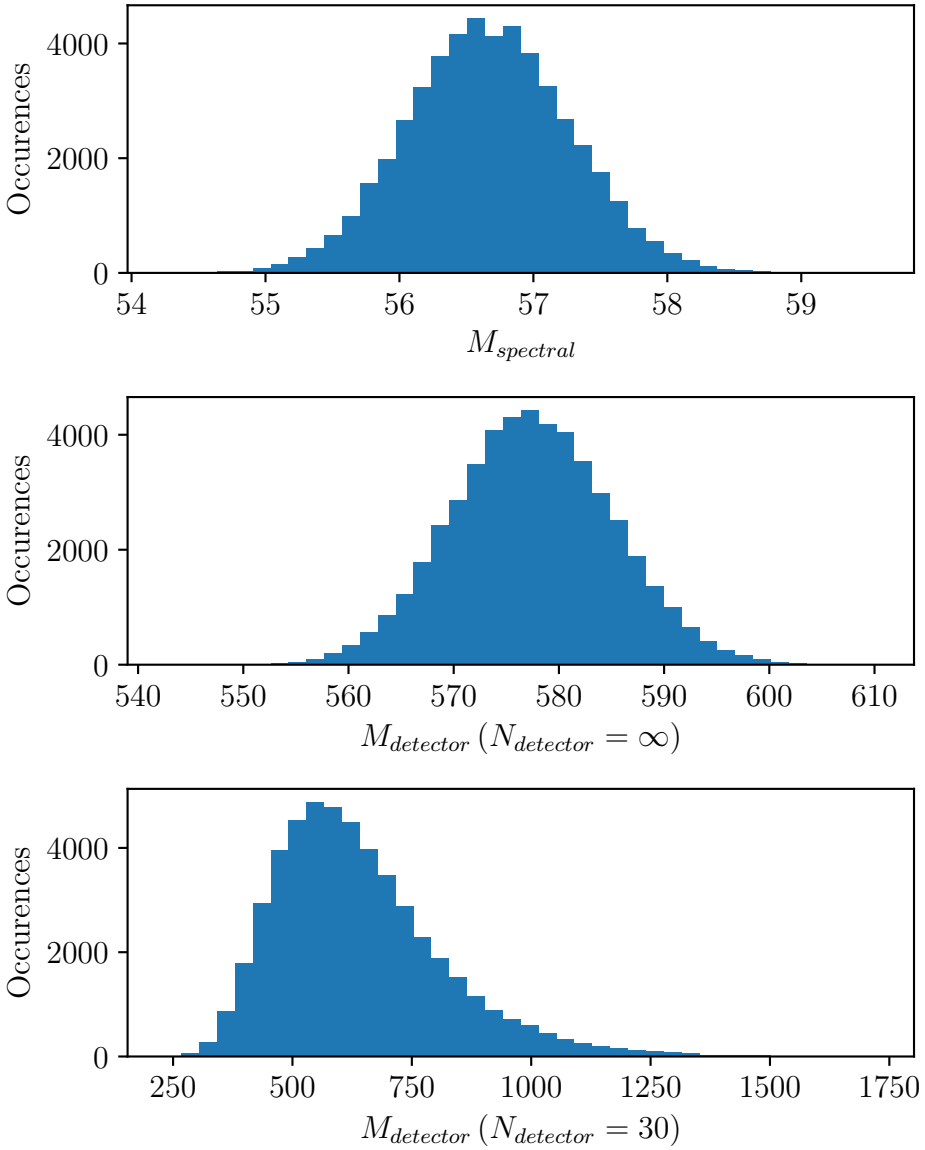

Figure 4.9: Histogram of 50 000 Monte Carlo occurrences following a normal distribution of (top) $M_{spectral}$ with $\mathcal{N}\left(\mu = 56.6, \sigma = \Delta M_{spectral}^{(MC)} = 0.7\right)$ and (middle) $M_{detector}$ with $\mathcal{N}\left(\mu = 5.8 \times 10^2, \sigma = 0.1 \times 10^2\right)$ by using normal distributed fluctuations $\sigma_{\rho_{n,m}}$ of 1.5 % in F and $\sigma_{L_{c,n}} = 1.3\,\%$ in Ψ for the NIR band. The bottom pane includes the contribution from the limited amount of pixels the final contrast level is calculated from. The 1σ width of this distribution is taken as uncertainty $\Delta M_{detector}^{(MC)}$.

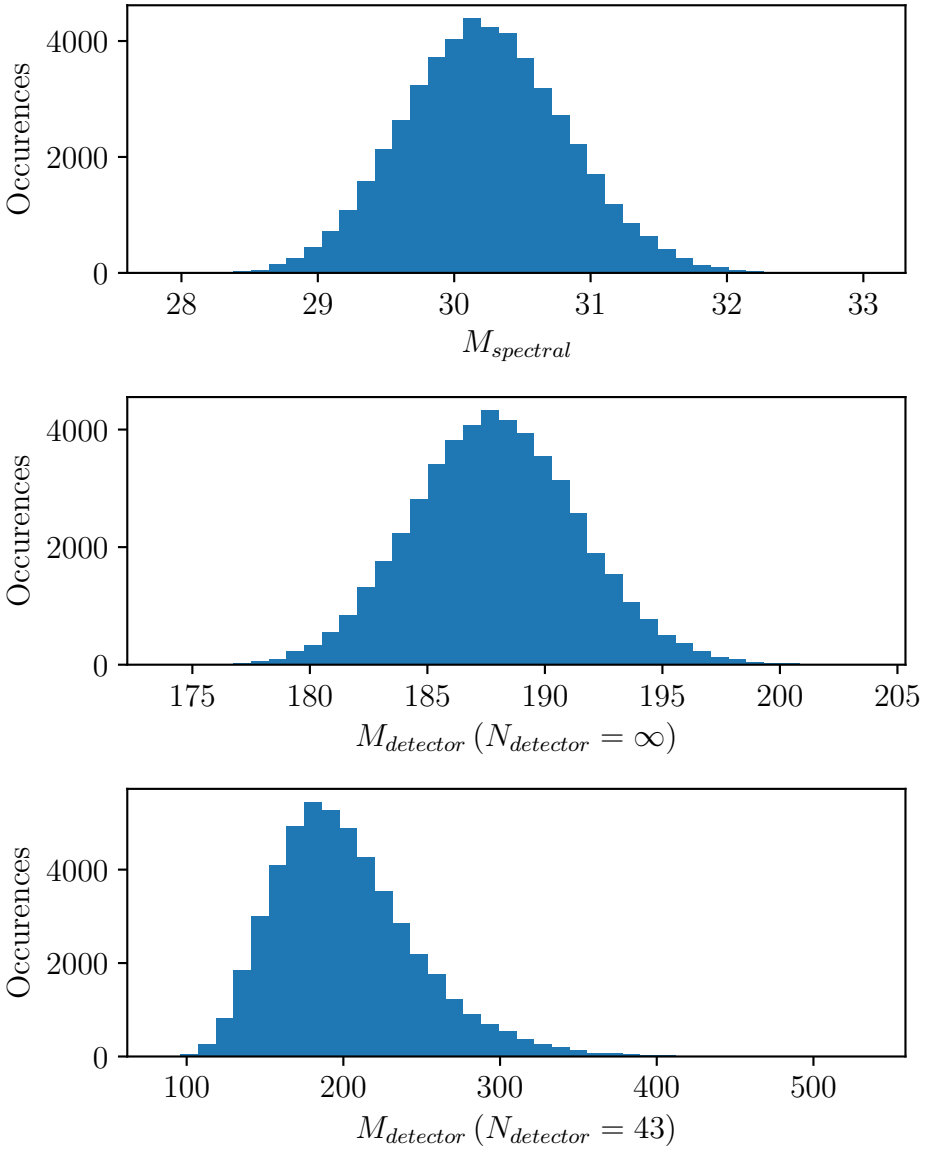

Figure 4.10: Histogram of 50 000 Monte Carlo occurrences following a normal distribution of (top) $M_{spectral}$ with $\mathcal{N}\left(\mu = 30.2, \sigma = \Delta M_{spectral}^{(MC)} = 0.6\right)$ and (middle) $M_{detector}$ with $\mathcal{N}\left(\mu = 1.88 \times 10^2, \sigma = 0.04 \times 10^2\right)$ by using normal distributed fluctuations $\sigma_{\rho_{n,m}}$ of 2.5 % in F and $\sigma_{L_{c,n}} = 2.7\,\%$ in Ψ for the SWIR band. The bottom pane includes the contribution from the limited amount of pixels the final contrast level is calculated from. The 1σ width of this distribution is taken as uncertainty $\Delta M_{detector}^{(MC)}$.

4.4.3 Comparison and Interpretation

In table 4.5 the estimations of the absolute uncertainties for $M_{spectral}$ and $M_{detector}$ with both approaches are given from the data of the study by Richter et al., 2021. Comparing the estimated values for $\Delta M_{spectral}^{(Gauss)}$ and $\Delta M_{spectral}^{(MC)}$ it is evident that only the latter one appreciably reflects the error contribution by the internal structure of individual images. As a consequence, the value from the Monte Carlo method is chosen for the final error estimation. On the other hand, for $\Delta M_{detector}^{(Gauss)}$ and $\Delta M_{detector}^{(MC)}$ both estimations show very good agreement, since the error from the under-sampling of the intensity distribution dominates. The Gaussian error propagation accounts for the highest contribution, which is the sampling of normal distribution by a limited amount of pixel. This effect can be reduced by the enlargement of the spectral tuning range. Acquiring data over a wider spectral range, however, increases uncertainties by wavelength scaling effects and time-dependent environmental influences. The SFA is given by eq. (3.7); $M_{polarization}$ is considered free of uncertainties; thus the final error on the SFA is

$$\frac{\Delta SFA}{SFA} = \sqrt{\frac{1}{2}\left|\frac{\Delta M_{spectral}^{(MC)}}{M_{spectral}}\right|^2 + \frac{1}{2}\left|\frac{\Delta M_{detector}^{(MC)}}{M_{detector}}\right|^2}. \tag{4.38}$$

Band	$\Delta M_{spectral}^{(Gauss)}$	$\Delta M_{spectral}^{(MC)}$	$\Delta M_{detector}^{(Gauss)}$	$\Delta M_{detector}^{(MC)}$	$\frac{\Delta SFA}{SFA}$
NIR	0.03	0.7	1.7×10^2	1.8×10^2	0.21
SWIR	0.03	0.6	0.4×10^2	0.5×10^2	0.21

Table 4.5: Absolute uncertainties calculated from the measurement data of the study by Richter et al., 2021 and the relative SFA uncertainty determined with eq. (4.38).

Chapter 5

Diffuser-Speckle in Test Spectrometer

The measurements presented in chapter 3 mimic the spectrometer up to the entrance slit. The imaging optics, including the dispersive element up to the detector, are simulated by numerical propagation of the data acquired in the entrance slit. Also, a number of simplifying assumptions are made to reduce the complexity of the optical system further. In this part, the SFA is measured with a complete spectrometer setup to verify that the complexity reduction is, in fact, minor, and the prediction model presented in chapter 4 can therefore be applied to real spectrometers. Compared to earlier end-to-end setups, it does not represent an actual instrument for a Remote-Sensing mission but is purposely design to yield a distinct speckle error signal for reliable measurement results. In section 5.1 the relevant spectrometer parameters are determined, which are needed as input for the prediction model. In section 5.2 the results of the SFA measurements are presented and discussed.

5.1 Test Spectrometer Characterization

The instrument parameters needed as input for the prediction model are derived in the following. As the manufacturer of the test spectrometer was not able to provide most of them. The unknown parameters of the instrument are therefore inferred given the principle layout of the instrument and the known basic parameters as provided by the manufacturer as follows. The optical layout of the spectrometer, which is known as crossed *Czerny-Turner* configuration, is depicted in fig. 5.1. The optical setup is the same as in previous sections, with the test spectrometer's entrance slit plane placed in the focal plane of the telescope. See fig. 3.3 in section 3.2 for details. The light field at the entrance slit of width W_{slit} is collimated onto the diffraction grating by a spherical mirror. It is positioned a distance after the slit, defining the entrance arm length L_a. The incident angle relative to the normal of the grating plane is denoted by α; the angle of the diffracted light with the normal by β. The grating is illuminated over a width of W_g. The diffracted light is focused on a linear detector array, which is positioned a distance after the focusing mirror, denoted by the exit arm length L_b. The angle γ denotes the inclination with respect to the normal of the detector plane. Initially, the following design parameters are known:

Holographic grating Groove density $n_g = 2400\,\mathrm{mm}^{-1}$.

f-number $f/\# = 4$.

Entrance/exit arm lengths The entrance and exit arms have the same length, $L_a = L_b = 102\,\mathrm{mm}$.

Detector $N_{px} = 3648\,\mathrm{px}$, $h_{pixel} = 200\,\mu\mathrm{m} \times w_{pixel} = 8\,\mu\mathrm{m}$ pixel size.

Wavelength range 434 nm to 517 nm, centered at 460 nm.

Slit dimensions Interchangeable slit widths $W_{slit} = \{10, 25, 50, 100\}\,\mu\mathrm{m}$ and slit height $H_{slit} = 1\,\mathrm{mm}$ available.

The angle of incidence α and the angle of diffraction β are related to the diffracted wavelength λ and groove density n_g of the grating by (Lerner, 2006)

$$\sin(\alpha) + \sin(\beta) = n_g \lambda, \tag{5.1}$$

where we assume that the spectrometer uses the first diffraction order from now on. The linear dispersion is given by (Lerner, 2006)

$$k \equiv \frac{d\lambda}{dx} = \frac{\cos(\beta)\cos(\gamma)}{n_g L_b}. \tag{5.2}$$

Strictly speaking, the exit arm length L_b and the inclination γ are wavelength dependent. Here, the fact is used that the spectrometer is centered around 460 nm to assume $\gamma \approx 0$ and $L_b = const$ if we consider only measurement data ranging a few nanometers around this center wavelength. For example, given the initial parameters by the supplier above, the wavelength of 475 nm hits the detector at an inclination of $\gamma \approx 3°$, which would result in an error of around 0.2 %. The magnification in spectral direction M_y and in spatial direction M_x are given by (Lerner, 2006)

$$M_x = \frac{L_b}{L_a} = 1, \tag{5.3}$$

$$M_y = \frac{\cos(\alpha) L_b}{\cos(\beta) L_a}. \tag{5.4}$$

The magnification of unity in spatial direction implies that only a fraction of the total entrance slit height is captured by the detector. From this, we can derive that the effective slit height is equal to the detector pixel height, $H'_{slit} = 200\,\mu m$. The spectral resolution of the instrument is the magnified slit width multiplied by the linear dispersion (Lerner, 2006), hence

$$\lambda_{res} = k M_y W_{slit} = \frac{W_{slit}\cos(\alpha)}{n_g L_a}. \tag{5.5}$$

By measuring the dispersion and the spectral resolution with the tunable monochromatic VIS laser source, presented in section 3.2, one can use eqs. (5.1) to (5.5) to establish the values for α and β required to describe the instrument. However, let us first formalize the measurement process of a spectrometer. Consider a function of intensity dependent on wavelength $S(\lambda)$ as input. The instrument assigns a finite wavelength interval from $\lambda(i)$ to $\lambda(i+1)$ to a discrete number of pixels N_{px} with index i (see Stutz et al., 2008, p. 157), which convert it to a signal S_i by

$$S_i = \int_{\lambda(i)}^{\lambda(i+1)} S(\lambda')\, d\lambda' . \tag{5.6}$$

Assuming a linear dispersion, the wavelength-pixel-mapping can be described by

$$\Omega : \lambda(i) = \lambda(0) + \Delta\lambda(i) \cdot i, \tag{5.7}$$

where $\lambda(0)$ is an offset representing the wavelength for pixel $i = 0$ and $\Delta\lambda(i) = \lambda(i+1) - \lambda(i)$. A second transformation of an original signal to be considered is a spectral broadening of a monochromatic stimulus (see Lerner, 2006), which in this case is due to the bandpass defining the spectral resolution given by the entrance slit. As one can see from eq. (5.5), the spectral resolution is proportional to the slit width W_{slit}. This implies that even for a spectral infinitely narrow input signal it will be measured with a width of λ_{res}. In order to estimate the dispersion of the spectrometer, the laser source is tuned over a wavelength range several times the spectral resolution. At every step j, the spectrum $S_{i,j}(\lambda_j)$ of the monochromatic laser line for the wavelength λ_j is acquired. During the acquisition the diffuser is rotated and translated simultaneously to average out the speckles. The technique is described in detail in section 3.4. Figure 5.2 depicts the intensity values of two chosen pixels with indices $i = 1020$ and $i = 1075$, which lie within the tuned wavelength range, with an installed slit width of $W_{slit} = 50\,\mu\text{m}$ and a step size $\Delta\lambda = 0.01\,\text{nm}$. The peaks are centered at $\lambda_1 = 460.35\,\text{nm}$ and $\lambda_2 = 461.69\,\text{nm}$.

Considering the detector pixel width of 8 µm the linear dispersion calculates as

$$k = \frac{461.69\,\text{nm} - 460.35\,\text{nm}}{(1075 - 1020) \cdot 0.008\,\text{mm}} = 3.046\,\frac{\text{nm}}{\text{mm}} = 0.0244\,\frac{\text{nm}}{\text{px}}.$$

The full width at half maximum of the two peaks is taken as the spectral resolution $\lambda_{res} = 0.179\,\text{nm}$ (Lerner, 2006). This procedure is repeated for all available slit widths. The results are summarized in table 5.1. The average estimated linear dispersion around 460 nm is determined to be $\overline{k} = (0.0244 \pm 0.0002)\,\text{nm/px}$ over nine separate measurements. By using eq. (5.2) the angle of diffraction is determined to be $\beta = 42°$. The interchangeable slits underlie manufacturing uncertainties regarding their width W_{slit}. Using an inverse linear regression (Freund et al., 2006), the actual slit widths W'_{slit} are estimated. The angle of incidence is iterated to $\alpha = 26.8°$ for the best fit with the smallest residuals. Table 5.1 shows the results with the 95 % confidence interval. All values are within a reasonable manufacturing uncertainty. The test spectrometer can now be fully described.

Nominal slit width W_{slit}	10 µm	25 µm	50 µm	100 µm
Estimated λ_{res}	0.035 nm	0.087 nm	0.178 nm	0.368 nm
Estimated W'_{slit}	(9.6 ± 1.3) µm	(24 ± 4) µm	(49 ± 4) µm	(101 ± 4) µm

Table 5.1: Measurement results of the spectral resolution λ_{res} for the available slit widths and the best inverse linear regression fit with the 95 % confidence interval for $\alpha = 26.8°$.

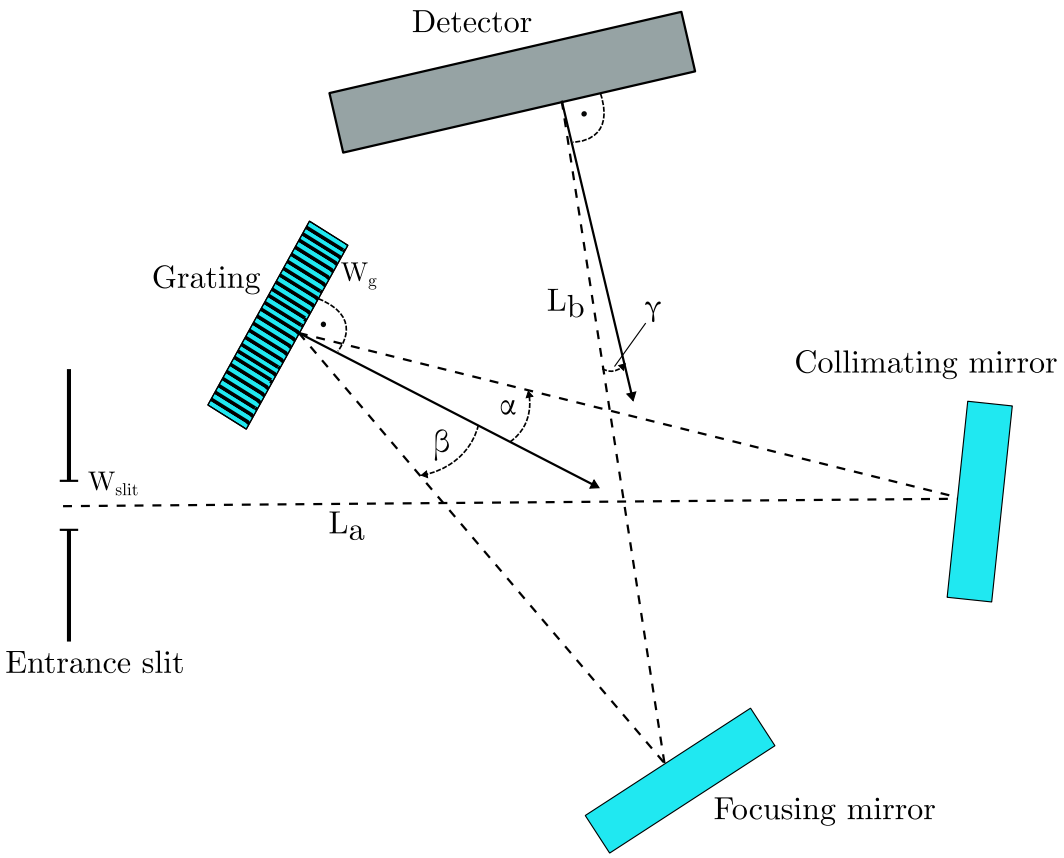

Figure 5.1: Optical bench of the crossed Czerny-Turner type test spectrometer. The light field at the entrance slit of width W_{slit} is collimated onto the diffraction grating by a spherical mirror. It is positioned a distance after the slit, defining the entrance arm length L_a. The incident angle relative to the normal of the grating plane is denoted by α; the angle of the diffracted light with the normal by β. The grating is illuminated over a width of W_g. The diffracted light is focused on a linear detector array, which is positioned a distance after the focusing mirror, denoted by the exit arm length L_b. The angle γ denotes the inclination with respect to the normal of the detector plane.

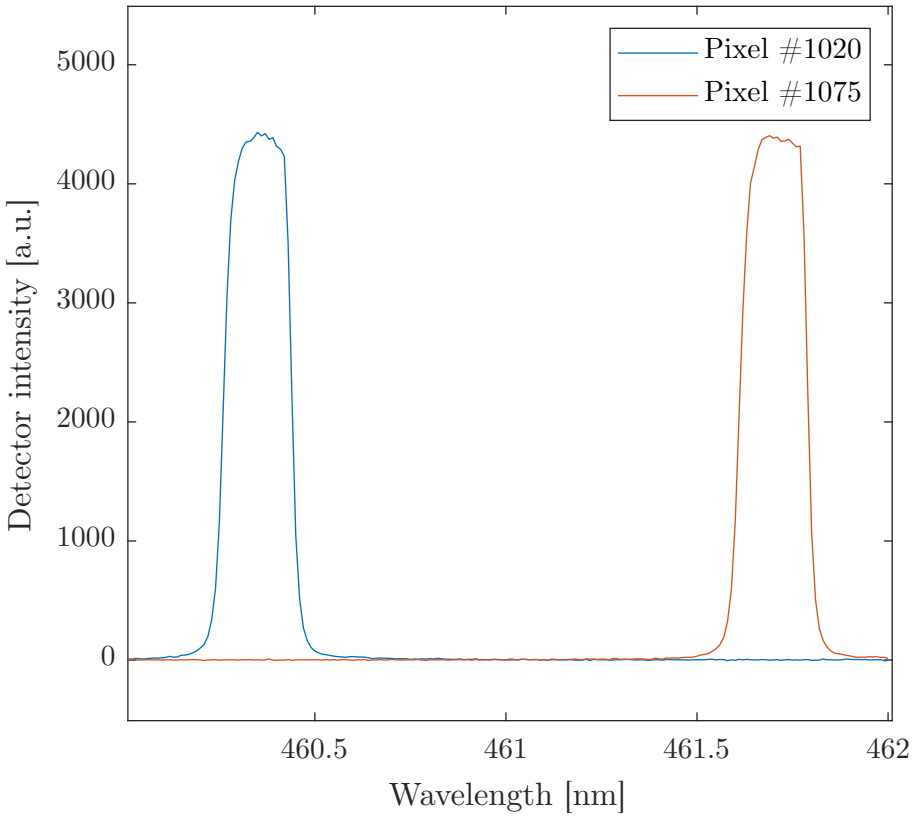

Figure 5.2: Plot of intensity values of the detector pixel #1020 and #1075 over a wavelength range of 2 nm with a slit width $W_{slit} = 50\,\mu m$ and a step size $\Delta\lambda = 0.01\,nm$. The spectral distance between the peaks of the two graphs at $\lambda_1 = 460.35\,nm$ and $\lambda_2 = 461.69\,nm$ is used to estimate the linear dispersion of $k = 3.046\,nm/mm$. The full widths at half maximum of the peaks are taken as the spectral resolution of $\lambda_{res} = 0.179\,nm$.

5.2 SFA Results and Comparison to Prediction Model

In this section, the speckle impact on measurements with the test spectrometer previously presented is determined and compared to the predictions of the model established in chapter 4. First, the generic measurement procedure is outlined. Then, the parameter space over which the test setup is varied is presented and justified. Finally, the measurement results are shown and discussed with respect to the predictions.

For every measurement, a spectral tuning step size $\Delta\lambda = 0.01\,\mathrm{nm}$ is chosen, which samples the instruments pixel dispersion of $k = 0.0244\,\mathrm{nm\,px^{-1}}$ (see eq. (5.2)). This is a compromise between the measurement time and the sampling condition as derived in section 4.1.2, eq. (4.16). From figs. 4.3 to 4.5 one can see that only for the last case of the 20 mm thick diffuser the sampling of the correlation function F is insufficient. However, we will see at the end of this section that the under-sampling has no significant effect in this case. The laser source is tuned twice over a wavelength range $\lambda_1 ... \lambda_N$. On the first run, the recorded spectra $S_{i,j,speckle}(\lambda_j)$ contain intensity fluctuations due to the diffuser speckles. On the second run, the diffuser is moved in order to suppress the speckles during every acquisition yielding the reference spectra $S_{i,j,ref}(\lambda_j)$. This is the same calibration method as employed in chapter 3. Every recorded spectrum is normalized with the simultaneously measured value of the power meter. In the post-processing, the spectra of both runs are subtracted with an averaged background spectrum consisting of 100 dark acquisitions. The monochromatic spectra $S'_{i,j,speckle}(\lambda_j)$ and $S'_{i,j,ref}(\lambda_j)$ of both runs are added,

$$S_{i,speckle} = \sum_{j=1}^{N} S'_{i,j,speckle}(\lambda_j)\,,$$

$$S_{i,ref} = \sum_{j=1}^{N} S'_{i,j,ref}(\lambda_j)\,,$$

yielding one spectrum $S_{i,speckle}$ containing speckles and one reference spectrum $S_{i,ref}$ with no speckles. Note that both are non-zero only for pixel corresponding to wavelengths in the interval $[\lambda_1, \lambda_N]$. Finally, the two spectra are divided, leaving us with the normalized speckle spectrum

$$\hat{S}_i = \frac{S_{i,speckle}}{S_{i,ref}}.$$

The SFA is calculated as the standard deviation of the measured wavelength range, hence

$$SFA\left(\hat{S}_i\right) = \sqrt{\frac{1}{i_N - i_1 - 1}\sum_{i=i_1}^{i_N}\left(\hat{S}_i - \overline{\hat{S}_i}\right)^2}, \tag{5.8}$$

where one can use the known dispersion k and fig. 5.2 from section 5.1 to calculate the pixel index i_0 corresponding to a wavelength $\lambda_0 = 460\,\text{nm}$. For the edge indices in the sum we have

$$i_1 = i_0 + \frac{\lambda_1 - \lambda_0}{k w_{pixel}}$$
$$i_N = i_1 + \frac{\lambda_N - \lambda_1}{k w_{pixel}}.$$

In contrast to earlier studies with setups, which are more representative of actual instruments (Brug et al., 2004; Brug and Courrèges-Lacoste, 2007), this test setup is chosen so that the speckle visibility is as high as possible to achieve more confident quantitative results concerning parameter changes. In chapter 4, it is established that the SFA is primarily governed by the geometrical extent of the speckle correlation areas Ψ and the diffuser correlation function F. The goal is to vary the two functions separately to show their dependency. With reference to eq. (4.5) the width of Ψ can be varied by choosing different pupil diameters D. Referring to eq. (4.3) one can adjust F by changing the diffuser thickness d. Figure 5.3 depicts an example for $S_{i,speckle}$, $S_{i,ref}$, and $\hat{S}_i$, respectively. The peaks and valleys present in $\hat{S}_i$ are due to the diffuser speckle. In order to verify this claim and to get a measure of the speckle correlation function at the detector μ_{det}, the

autocorrelation of $\hat{S}_i$ is determined numerically with a lagged correlation coefficient (see section 2.1, eq. (2.10))

$$|\mu_{det}|^2 \sim \rho_{\hat{S}_i}(\eta) = \frac{E\left[\left(\hat{S}_i - \mu\right)\left(\overline{\hat{S}_{i+\eta} - \mu}\right)\right]}{\sigma^2_{\hat{S}_i}}, \tag{5.9}$$

where $\mu = \overline{\hat{S}_i}$. The result for the exemplary measurement is shown in fig. 5.4. Thus, $\hat{S}_i$ can be analyzed in terms of μ_{det}, which essentially is the spectral extent of the speckles $L_{c,det}$, and the amplitude, which is the SFA.

In the following, a summary of all conducted measurements with their respective parameters is presented. They were all conducted with the 50 µm slit, which is a compromise between throughput of the spectrometer, the speckle extent at the slit, and detector plane, and the SFA. The findings in section 3.3 essentially restrict the usable aperture diameter D to values of 20 mm and smaller. The speckle size in the entrance slit plane should not exceed the slit width significantly to avoid effects from speckles being partially cut off. Using eq. (2.88) the expected speckle size for an aperture diameter of 10 mm at 460 nm wavelength and the known telescope focal length of $f_{tel} = 1100$ mm is 57 µm, thus constituting the lower diameter limit. The spectral tuning step size for all measurements is $\Delta\lambda = 0.01$ nm. The diffusers are characterized by the correlation function F, which is influenced by the thickness d and the transport mean free path l_t which are both determined in section 4.2. All

Parameter	**Value**
Magnification M_x	1
Magnification M_y	1.20
Slit dimensions (x, y–direction)	200 µm, 49 µm
Detector pixel dimension (a, b–direction)	200 µm, 8 µm
Telescope focal length f_{tel}	1100 mm
Spectral resolution λ_{res}	0.178 nm (7.3 px)

Table 5.2: Summary of the test spectrometer parameters used for the measurement and prediction.

measurement results (M) together with the corresponding predictions (P) are shown in table 5.3 for variations of the aperture diameter D and the diffuser thickness

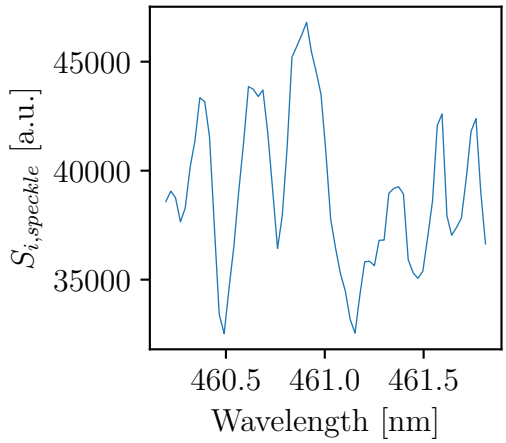

(a) Spectrum $S_{i,speckle}$ containing speckles.

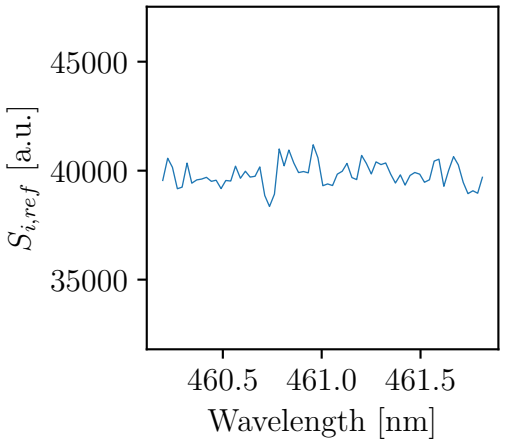

(b) Despeckled reference spectrum $S_{i,ref}$

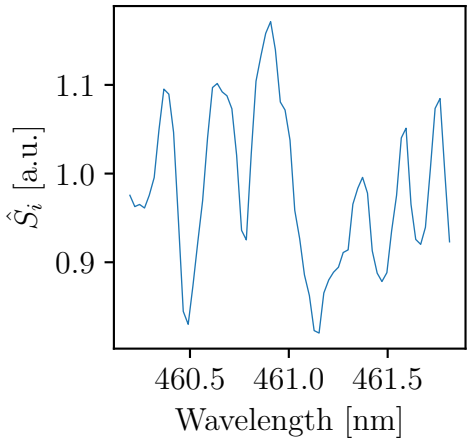

(c) Speckle spectrum $\hat{S}_i$ normalized with the reference.

Figure 5.3: Example of a spectrum (a) containing speckles, (b) without speckles, and (c) the ratio of speckle spectrum with the reference.

d. For every measurement, the tuning range is given. The SFA is calculated with eq. (5.8). The uncertainty is approximated with the error of the standard deviation estimator (Ahn and Fessler, 2003)

$$\frac{\Delta SFA}{SFA} \approx \frac{1}{\sqrt{2\,(i_N - i_1 - 1)}}, \tag{5.10}$$

which implies a dependence of the uncertainties to the spectral length of the measurement. This error estimation is similar to the component $\Delta M_{detector}^{(Gauss)}$ in

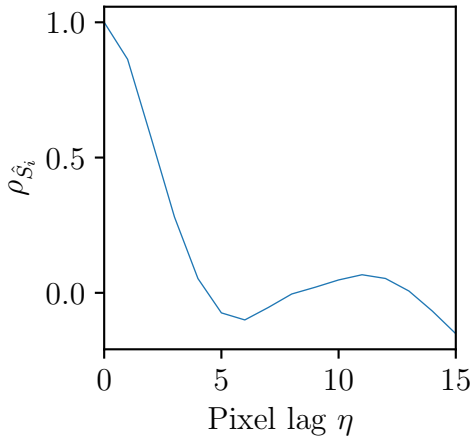

Figure 5.4: Numerically calculated autocorrelation coefficient $\rho_{\hat{S}_i}$ to estimate the width $L_{c,det}$ of the correlation function μ_{det} at the detector. See eq. (4.20) for reference. The autocorrelation falls to zero after approximately four pixels.

section 4.4 which is significantly greater than any other of the discussed error contributions. It is thus a good approximation for the total uncertainty. The speckle size $L_{c,det}$ is determined with eq. (5.9). All measured SFA values are in good agreement with the corresponding predictions within the estimated error interval. The speckle size is systematically smaller than predicted, except for the case with $D = 20\,\text{mm}$. An explanation could be the short tuning ranges, which make deviations from the actual speckle size more likely. From the measurements with $D = 15\,\text{mm}$, it seems that the speckle size is not dependent on the diffuser correlation F. This is expected since the geometric speckle size denoted by Ψ is much wider than F. Thus, for this instrument setup, F only influences the SFA appreciably. In summary, the presented results illustrate that the diffuser-induced speckle errors can be predicted with satisfactory accuracy for the selected test spectrometer.

Measurement (M) Prediction (P)	$\lambda_1...\lambda_N$ [nm]	D [mm]	d [mm]	$L_{c,det}$ [px]	SFA [%]
P	460	10	0.5	5.8	12.5
M	460.3...461.6	10	0.5	5.5	11.1 ± 1.8
	460.3...461.2			5.5	11.8 ± 1.7
P	460	15	0.5	4.5	10.5
M	460.2...462.3	15	0.5	4.1	10.3 ± 0.8
P	460	20	0.5	3.9	9.1
M	460.2...461.8	20	0.5	4.0	8.9 ± 0.8
	460.2...462.2			3.5	9.2 ± 0.9
P	460	15	1.0	4.5	7.4
M	460.2...462.2	15	1.0	4.2	7.7 ± 0.7
	460.2...461.8			4.0	7.4 ± 0.7
P	460	15	2.0	4.5	4.5
M	460.2...461.4	15	2.0	4.0	5.0 ± 0.6

Table 5.3: Measurements results (M) of the SFA and the speckle size $L_{c,det}$ for various aperture diameters D and diffuser thicknesses d over the wavelength tuning range $\lambda_1...\lambda_N$ compared with the corresponding prediction (P).

Chapter 6

Diffuser-Speckle Impact on DOAS Retrieval

In the previous chapters, the predictive model is tested on two different measurement methods and instruments. The speckle errors are given in terms of the SFA, which is a measure on instrument detector level. In this chapter, the prediction model is used to estimate the impact of speckles on a retrieval of the NO_2 column via a method known as Differential Optical Absorption Spectroscopy (DOAS). For this purpose, the VIS-3 channel of the Global Ozone Monitoring Experiment (GOME) is used as a reference for the prediction model. This instrument is chosen as an extreme case for this study since the diffuser speckle error played a more distinct role than for more recent instruments. First, the DOAS retrieval technique is explained in section 6.1 followed by an introduction to Radiative Transfer Models (RTM) and the approach to solve the underlying Radiative Transport Equation (RTE) in section 6.2. The latter concept is needed to generate an artificial reflectance spectrum for which a measurement by the GOME instrument is mimicked, which is shown in section 6.3. After, the derivation of the diffuser speckle signal parameters from the GOME instrument is outlined in section 6.4 followed by section 6.5, which explains the preparation of the speckle-distorted error spectra. In the final section 6.6 the DOAS retrieval process is described incorporating speckle errors of

different severity. The results are compared to known column uncertainties from earlier studies of GOME retrieval data.

6.1 Differential Optical Absorption Spectroscopy

In this section the Differential Optical Absorption (DOAS) method is described, which is used to retrieve the NO_2 column density from an artificial Earth reflectance spectrum (see section 6.3). The following discussion is based on the comprehensive book about DOAS by Stutz et al., 2008. The absorption of light by trace gases in the atmosphere can be described by the Beer-Lambert law. It can be written as

$$I(\lambda) = I_0(\lambda) \exp\left(- \int \sigma(\lambda, T(s))\, c(s)\, ds \right), \tag{6.1}$$

where $I_0(\lambda)$ denotes the initial intensity of the light entering the atmosphere and $I(\lambda)$ is the intensity after the light has propagated through a column with concentration profile $c(s)$. The item $\sigma(\lambda, T(s))$ denotes the temperature dependent characteristic absorption cross-section of the respective trace gas species. The temperature dependency is usually omitted by using the temperature at the number density maximum of the climatological profile of the respective trace gas (see Burrows et al., 1999) or by applying other temperature corrections (Wenig et al., 2005). For an absorption measurement in the atmosphere eq. (6.1) has to be applied to all present trace gases and needs to consider all other influences:

$$I(\lambda) = I_0(\lambda) \exp\left(- \sum_i \sigma_i(\lambda)\, \mathrm{SCD}_i \right) A(\lambda), \tag{6.2}$$

where $I(\lambda)$ is the measured intensity, $I_0(\lambda)$ is the solar reference spectrum, and $A(\lambda)$ is an attenuation factor combining effects by *Mie* and *Rayleigh* scattering, the impact of the instrument, and all other broadband-constituted influences. The sum in the exponential function is over all present trace gases i with an absorption cross-section $\sigma_i(\lambda)$ and their respective *slant column density* SCD_i, which is given

by

$$\mathrm{SCD}_i = \int c_i(s)\, ds\,. \tag{6.3}$$

The concentration of the absorber i is denoted by $c_i(s)$ and needs to be integrated over the entire light path. The absorption cross-sections $\sigma_i(\lambda)$ are well-known from laboratory measurements and characteristic for the respective trace gas. Equation (6.2) can be rewritten by taking the logarithm on both sides:

$$\ln(I(\lambda)) = \ln(I_0(\lambda)) - \sum_i \sigma_i(\lambda)\,\mathrm{SCD}_i + \ln(A(\lambda)). \tag{6.4}$$

Usually, either the attenuation factor $A(\lambda)$ or the initial intensity $I_0(\lambda)$ are not *a priori* known, which essentially makes solving for the desired SCD_i impossible. However, this problem can be circumvented, which is the core idea behind the DOAS technique: the quantities combined in $A(\lambda)$ show very broad spectral characteristics, whereas certain absorbers' cross-sections $\sigma_i(\lambda)$ display narrow-band structures. Thus, we may split them up into a slow varying or low frequency (LF) part $\sigma_i^{LF}(\lambda)$ and a fast varying or high frequency (HF) part $\sigma_i'(\lambda)$ by

$$\sigma_i(\lambda) = \sigma_i^{LF}(\lambda) + \sigma_i'(\lambda)\,. \tag{6.5}$$

If one models all low frequency contributions by a set of suitable basis functions $\epsilon_j(\lambda)$ (Wenig et al., 2005),

$$\ln(I_0(\lambda)) - \sum_i \sigma_i^{LF}(\lambda)\,\mathrm{SCD}_i + \ln(A(\lambda)) = \sum_j a_j \epsilon_j(\lambda) =: \ln(I_0'(\lambda)), \tag{6.6}$$

eq. (6.4) becomes

$$\ln(I(\lambda)) = \underbrace{\sum_j a_j \epsilon_j(\lambda)}_{\mathrm{LF}} - \underbrace{\sum_i \sigma_i'(\lambda)\,\mathrm{SCD}_i}_{\mathrm{HF}}, \tag{6.7}$$

which is linear in the unknown quantities a_j and SCD_i and can be determined via a linear least-squares method (Wenig et al., 2005). The quantity $I'_0(\lambda)$ can be interpreted as the intensity in the absence of any HF absorbers. The HF part is called the differential optical density and is given by

$$D'(\lambda) = \ln\left(\frac{I'_0(\lambda)}{I(\lambda)}\right) = \sum_i \sigma'_i(\lambda)\,\mathrm{SCD}_i. \tag{6.8}$$

This summarizes the basic idea behind the DOAS method.

6.2 Radiative Transfer Modeling

In this section the basics of radiative transfer modeling (RTM) are described. This concept is used to generate an artificial Earth reflectance spectrum in section 6.3. Radiative transfer models approximate the propagation and extinction of light in the Earth's atmosphere, which is a complex process. Photons can be scattered multiple times into the light path under consideration from all directions as well as leave it in the same manner. Also, they can be absorbed. Additionally, at long wavelengths thermal emissions may play a role. The goal of any RTM is finding a solution for the *Radiative Transport Equation* (RTE), which in its general form in a steady-state can be written as (Stamnes, 1986):

$$(\hat{n}\cdot\nabla)\,I(\mathbf{r},\hat{n},\nu) = h\nu Q(\mathbf{r},\hat{n},\nu)\,. \tag{6.9}$$

The quantity $I(\mathbf{r},\hat{n},\nu)$ is the specific radiance of light of frequency ν at location $\mathbf{r}$ propagating in direction $\hat{n}$. The term $(\hat{n}\cdot\nabla)$ is called the *streaming term* and defines the geometry. The source term $Q(\mathbf{r},\hat{n},\nu)$ represents scattering and emission as the causes for the change in the radiance and can be expressed for a planetary

atmosphere as (Chandrasekhar, 2011):

$$\begin{aligned} h\nu Q\left(\mathbf{r},\hat{n},\nu\right) = h\nu Q\left(r,\theta,\phi,\nu\right) &= -\beta^{ext}\left(r,\nu\right) I\left(r,\theta,\phi,\nu\right) \\ &+ \frac{1}{4\pi}\int_0^{\infty} d\nu'\,\beta^{sca}\left(r,\nu,\nu'\right)\int_0^{2\pi} d\phi'\,p\left(r,\theta,\phi,\theta',\phi',\nu'\right) I\left(r,\theta',\phi',\nu'\right) \\ &+ \beta^{abs}\left(r,\nu\right) B\left[T\left(r\right),\nu\right]. \end{aligned} \tag{6.10}$$

The above equation consists of three terms – one with the negative sign representing the extinction of light in the current path by absorption and scattering, the second one with a positive sign denoting the addition of light to it's current path by other multi-scattering events, and the third one also with a positive sign called *emission term*, which is in the approximation of a thermodynamic equilibrium of the atmosphere proportional to the Planck function at temperature $T\left(r\right)$ and frequency ν, $B\left[T\left(r\right),\nu\right]$ (Mihalas, 1978, p. 26). By Kirchhoff's law the emission coefficient β^{emi} equals the absorption coefficient β^{abs}. The coefficients for absorption, scattering, and extinction are defined as (Stamnes, 1986):

$$\beta^{abs}\left(r,\nu\right) = \sum_i \beta_i^{abs}\left(r,\nu\right) \qquad \beta_i^{abs}\left(r,\nu\right) = n_i\left(r\right)\sigma_i^{abs}\left(\nu\right) \tag{6.11}$$

$$\beta^{sca}\left(r,\nu\right) = \sum_i \beta_i^{sca}\left(r,\nu\right) \qquad \beta_i^{sca}\left(r,\nu\right) = n_i\left(r\right)\sigma_i^{sca}\left(\nu\right) \tag{6.12}$$

$$\beta^{ext}\left(r,\nu\right) = \beta^{abs}\left(r,\nu\right) + \beta^{sca}\left(r,\nu\right), \tag{6.13}$$

where $n_i\left(r\right)$ is the density of the respective species i and $\sigma_i^{abs}\left(\nu\right)$ and $\sigma_i^{abs}\left(\nu\right)$ are the corresponding absorption and scattering cross-sections. The scattering phase function p is given by

$$p\left(r,\theta,\phi,\theta',\phi',\nu\right) = \frac{\sum_i \beta_i^{abs}\left(r,\nu\right) p_i\left(\theta,\phi,\theta',\phi',\nu\right)}{\sum_i \beta_i^{abs}\left(r,\nu\right)} \tag{6.14}$$

and the phase functions for the individual species p_i being

$$p_i\left(\theta,\phi,\theta',\phi',\nu\right) = p_i\left(\cos(\Theta),\nu\right) = \frac{\sigma_i^{sca}\left(\cos(\Theta),\nu\right)}{\int_{4\pi} d\Omega\, \sigma_i^{sca}\left(\cos(\Theta),\nu\right)}. \tag{6.15}$$

The scattering angle Θ is related to the polar and azimuth angle through the cosine law of spherical geometry by

$$\cos(\Theta) = \cos(\theta')\cos(\theta) + \sin(\theta')\sin(\theta)\cos(\phi-\phi'). \tag{6.16}$$

Due to the scattering term in the source of eq. (6.9) there is no direct analytic solution to it, except in very specific simplified cases. However, depending on the wavelength regime and complexity of the to be modeled atmosphere there are two general groups of approaches to numerical solutions that can be taken. The first one is of statistical nature, in which the paths of many individual photons with parameters randomly sampled from appropriate PDFs are traced through the atmosphere under the desired conditions. The second group relies on the calculation of a numerical solution for the resulting radiation field (Stutz et al., 2008). One approach of the former group is a *Discrete Ordinate Method*, for which an widely used algorithm called DISORT was put forward by Stamnes et al., 1988. Since this method is chosen for the calculations in section 6.3, it will be the sole focus of the following discussion. In Cartesian coordinates the streaming term can be written as (Kuo et al., 1996):

$$\begin{aligned}(\hat{n}\cdot\nabla) &= n_x\frac{\partial}{\partial x} + n_y\frac{\partial}{\partial y} + n_z\frac{\partial}{\partial z} \\ &= \cos(\phi)\sqrt{1-\cos^2(\theta)}\frac{\partial}{\partial x} + \sin(\phi)\sqrt{1-\cos^2(\theta)}\frac{\partial}{\partial y} + \cos(\theta)\frac{\partial}{\partial z},\end{aligned} \tag{6.17}$$

where (n_x, n_y, n_z) are the components of the unit vector, θ is the polar angle and ϕ is the azimuth angle. Following Stamnes, 1986 we use the plane-parallel geometry, which assumes a flat Earth surface and divides the atmosphere into parallel layers

of infinite size in x– and y–directions. The streaming term then becomes

$$(\hat{n} \cdot \nabla) = \cos(\theta) \frac{\partial}{\partial z}. \tag{6.18}$$

By making the above approximation, substituting $\mu = \cos(\theta)$ and introducing the vertical optical thickness $d\tau = \beta^{ext}\, dz$ eq. (6.9) can be written with the source from eq. (6.10) as follows:

$$\begin{aligned} \mu \frac{dI\left(\tau, \mu, \phi, \nu\right)}{d\tau} = & - I\left(\tau, \mu, \phi, \nu\right) \\ & + \frac{\omega\left(\tau, \nu\right)}{4} \int_0^{2\pi} d\phi' \int_{-1}^{1} d\mu'\, p\left(\tau, \mu, \phi, \mu', \phi', \nu\right), \end{aligned} \tag{6.19}$$

where we have dropped the emission term, since it can be neglected for the visible wavelength regime which is of interest for this study. The same goes for frequency redistributions due to Raman scattering. The photons are assumed to be monochromatic throughout the propagation. The item $\omega\left(\tau, \nu\right)$ is called the single scattering albedo and is defined by

$$\omega\left(\tau, \nu\right) = \frac{\beta_i^{sca}\left(r, \nu\right)}{\beta_i^{ext}\left(r, \nu\right)} = \frac{\beta_i^{sca}\left(r, \nu\right)}{\beta_i^{abs}\left(r, \nu\right) + \beta_i^{sca}\left(r, \nu\right)}. \tag{6.20}$$

Now, a technique known as the *direct/diffuse distinction* (Stamnes, 1986) is applied. For that, the intensity is split up into the direct beam portion $I^{dir}\left(\nu\right)$ and the diffuse or scattered part $I^{sca}\left(\nu\right)$ by

$$I\left(\nu\right) = I^{dir}\left(\nu\right) + I^{sca}\left(\nu\right). \tag{6.21}$$

If we assume that no multiple scattering occurs, then the direct portion remains, for which setting the scattering term to zero and integration of eq. (6.19) immediately yields

$$I^{dir}\left(\tau, \mu, \phi, \nu\right) = I^{inc}\left(0, \mu = -\mu_0, \phi = \phi_0, \nu\right) \exp\left(-\frac{\tau}{\mu_0}\right), \tag{6.22}$$

where $I^{inc}(0, -\mu_0, \phi_0, \nu)$ is the incident radiation on the top of atmosphere at $\tau = 0$. Equation (6.22) is the Lambert-Beer law. For a parallel beam of sunlight the boundary condition at the top is

$$I^{dir}(0, \mu, \phi, \nu) = I^{inc}(\nu)\,\delta(\mu - \mu_0)\,\delta(\phi - \phi_0) \tag{6.23}$$

The first term in eq. (6.21) is solved by eq. (6.22), while for the second term the solution can be found by solving the RTE

$$\begin{aligned}\mu\frac{dI^{sca}(\tau, \mu, \phi, \nu)}{d\tau} =& -I^{sca}(\tau, \mu, \phi, \nu) \\ &+ \frac{\omega(\tau, \nu)}{4}\int_0^{2\pi} d\phi' \int_{-1}^{1} d\mu'\, p(\tau, \mu, \phi, \mu', \phi', \nu) \\ &+ \frac{\omega(\tau, \nu)\, I^{inc}}{4} p(\tau, \theta, \phi, -\mu_0, \phi_0, \nu) \exp\left(-\frac{\tau}{\mu_0}\right).\end{aligned} \tag{6.24}$$

For these cases with multi-scattering events we need to specify the boundary conditions, which is

$$I(0, -\mu_0, \phi_0, \nu) = 0 \tag{6.25}$$

at the top, and

$$\pi I(\tau_g, \mu, \nu) = \mu_0 A I^{inc} \exp\left(-\frac{\tau_g}{\mu_0}\right) + 2\pi A \int_0^{2\pi} d\phi' \int_0^{1} d\mu'\, \mu' I(\tau_g, -\mu', \nu) \tag{6.26}$$

at the bottom in case of a Lambertain reflecting surface with albedo A. Now the fact is used, that for scattering processes in the atmosphere the phase function only depends on the scattering angle Θ. With this, the Θ–dependence in eq. (6.24) is isolated by expanding the known phase function as series of Legendre polynomials P_l (see Thomas, 1999, section 6.3),

$$p(\tau, \theta, \phi, \theta', \phi', \nu) = p(\tau, \Theta, \nu) \approx \sum_{l=0}^{2M-1} (2l + 1)\, g_l(\tau, \nu)\, P_l(\cos(\Theta)), \tag{6.27}$$

where l^{th} expansion coefficient g_l is given by

$$g_l(\tau,\nu) = \int_{-1}^{1} P_l(\cos(\Theta))\, p(\tau,\Theta,\nu)\, d\cos(\Theta)\,. \tag{6.28}$$

Then the addition theorem for spherical harmonics (see Gradshteyn, 2007, section 8) is applied to eq. (6.27) to give

$$p(\tau,\Theta,\nu) = \sum_{l=0}^{2M-1} (2l+1)\, g_l(\tau,\nu) \left[P_l(\mu)\, P_l(\mu') + 2\sum_{m=1}^{l} \Lambda_l^m(\mu)\, \Lambda_l^m(\mu') \cos(m(\phi_0-\phi)) \right], \tag{6.29}$$

where the normalized associated Legendre polynomials are defined by

$$\Lambda_l^m(\mu) = \sqrt{\frac{(l-m)!}{(l+m)!}} P_l^m(\mu)\,, \tag{6.30}$$

and $P_l^m(\mu)$ are the associated Legendre polynomials. The intensity is expanded as a cosine Fourier series with

$$I(\tau,\mu,\phi,\nu) = \sum_{l=0}^{2M-1} I^m(\tau,\mu,\nu)\cos(m(\phi_0-\phi)). \tag{6.31}$$

By inserting eqs. (6.29) and (6.31) into eq. (6.24) yields $2M$ independent input equations for the DISORT solver algorithm, for which the solution can be found via an eigenvalue problem:

$$\begin{aligned} \mu\frac{dI^m(\tau,\mu,\nu)}{d\tau} &= -I^m(\tau,\mu,\nu) \\ &+ \frac{\omega(\tau,\nu)}{2}\int_{-1}^{1} d\mu' \sum_{l=m}^{2M-1} (2l+1)\, g_l(\tau,\nu)\, \Lambda_l^m(\mu)\, \Lambda_l^m(\mu')\, I^m(\tau,\mu',\nu) \\ &+ \frac{\omega(\tau,\nu)\, I^{inc}}{4}(2-\delta_{m0}) \sum_{l=0}^{2M-1} (2l+1)\, g_l(\tau,\nu)\, \Lambda_l^m(\mu)\, \Lambda_l^m(\mu') \exp\left(-\frac{\tau}{\mu_0}\right), \end{aligned} \tag{6.32}$$

where

$$\delta_{m0} = \begin{cases} 1 & m = 0 \\ 0 & m \neq 0. \end{cases}$$

In the entire derivation we have neglected polarization effects, which are not of interest for the following sections.

6.3 Generation of an Earth Reflectance Spectrum

In this section, the generation of an artificial Earth reflectance spectrum is described, which is used in the following sections for the retrievals of the NO_2 column density. For the RTM simulation the libRadtran software package version 2.0 is used (see Emde et al., 2016; Mayer and Kylling, 2005). For this study a wavelength range in the visible regime between 400 nm and 470 nm for the NO_2 retrieval is chosen. The following specimen with their respective cross-sections are included: NO_2 (Vandaele et al., 1998), O_3 (Serdyuchenko et al., 2014, version 25 July 2012), O_4 (Thalman and Volkamer, 2013), and water vapor (Rothman et al., 2010). The high-resolution extraterrestrial solar spectrum by Chance and Kurucz, 2010 serves as a reference. It is interpolated to a 1 pm sampling via a cubic spline interpolation. This ensures, that high frequency components of the O_3 and O_4 cross-sections are properly included into the calculations. Also, the US-standard atmosphere by Anderson et al., 1986 is used. The radiative transfer equation is solved via the Discrete-Ordinate Method with the DISORT algorithm (see section 6.2 for details), which was originally provided by Stamnes et al., 2000 and written in fortran77. In this case the optimized C portation by Buras et al., 2011 is used. We set up a geometry representative for a satellite by

- specifying a top of atmosphere (TOA) measurement height,
- pointing our sensor in nadir direction,
- and choosing an average solar zenith angle of 32°.

The surface albedo is set to 10 %. The complete input file can be found in the appendix, listing 7.1. With the above settings the high-resolution Earth reflectance spectrum is output. It is depicted in fig. 6.1. The slit function of the reference instrument is considered later in the retrieval procedure.

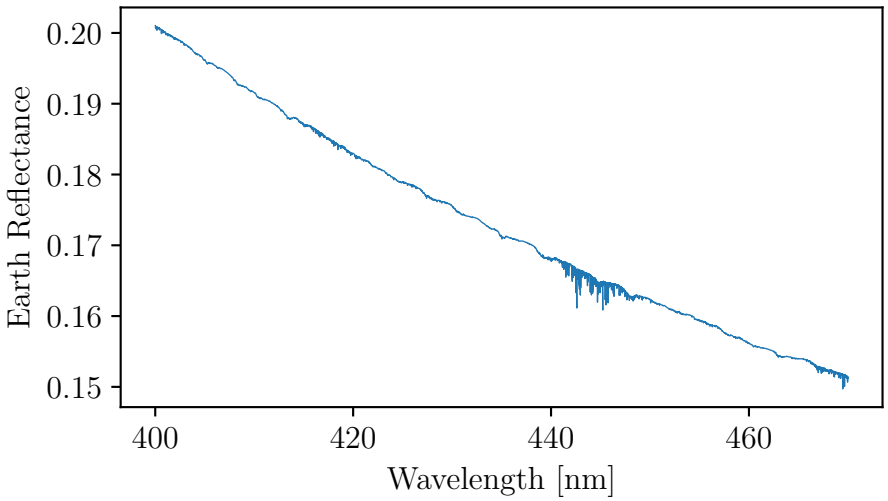

Figure 6.1: High-resolution simulated Earth reflectance spectrum as perceived by a downward looking sensor at TOA altitude for the wavelength range between 400 nm and 470 nm with incorporated cross-sections of NO_2, O_3, O_4, and water vapor in a standard US-atmosphere profile by Anderson et al., 1986. There is no instrument slit function considered.

6.4 Speckle Error Prediction for the GOME Instrument

In this section, the relevant input parameters of the GOME VIS-3 instrument channel for the prediction model and the SFA result are given. As a reference for the instrument parameters serves the GOME User Manual by the ESTEC Publishing Division, 1995. The values are shown in table 6.1. Since the diffuser is a sand-blasted Aluminum plate used in a reflection imaging geometry, we need to adjust the model for the diffuser correlation function F and the polarization of the scattered light compared to chapter 4. In the absence of any specific indications

about the GOME diffuser plate, we adopt a simple model of Gaussian surface height fluctuations (see J. W. Goodman, 2020, section 6.3.1, p. 193f) and combine it with the result of the discussion made in section 2.2.7 to the intensity correlation

$$|F(\Delta q_z)|^2 = \exp\big(-(\sigma_h \Delta q_z)^2\big), \tag{6.33}$$

where we repeat the equation for the normal component of the scattering vector at the diffuser Δq_z (see eq. (2.119)) for convenience:

$$\Delta q_z = \left| \frac{2\pi}{\lambda_1} \left[\cos(\theta_{o1}) + \cos(\theta_{i1})\right] - \frac{2\pi}{\lambda_2} \left[\cos(\theta_{o2}) + \cos(\theta_{i2})\right] \right|. \tag{6.34}$$

It depends on the difference in the wavelengths λ_1, λ_2, and the changes in the angle of illumination θ_{i1} and θ_{i2}. The angle of observation θ_o is assumed constant. With the GOME User Manual (ESTEC Publishing Division, 1995), p. 32 fig. 4.4-6b, the angle of incident, $\theta_{i1} = 12°$, and angle of observation, $\theta_o = 0°$ are deduced. The term σ_h denotes the RMS height of the diffuser's surface roughness. We set it to an intermediate value of $\sigma_h = 30\overline{\lambda} \approx 13\,\mu\text{m}$, which seems a realistic starting point according to Slatineanu et al., 2011; Draganovská et al., 2018. Variations of this parameter are discussed later. For the polarization, the argument is as follows: the Sunlight incident on the diffuser initially features two orthogonal polarization states. An effective volume diffuser, as used in experiments throughout this work, depolarizes each state due to multiple scattering events yielding two independent speckle intensities for each state. For a surface diffuser, multiple scattering events are less likely depending on the angle of incident and the surface roughness, meaning less depolarization can be expected (Elies et al., 1997). Therefore, we can infer that $2 < M_{polarization} < 4$. As a starting point an intermediate value of $M_{polarization} = 3$ is chosen. A summary of the GOME instrument parameter serving as inputs for the prediction model is given in table 6.1. They are taken from the GOME user manual (see ESTEC Publishing Division, 1995). The speckle error without averaging contribution due to the changing illumination angle during the calibration

is estimated to

$$SFA_{GOME} = 0.64\,\% \tag{6.35}$$

with a speckle extent at the detector of $L_{c,det} = 10\,\text{px}$. From p. 127 of the GOME

Parameter	**Value**
Magnification M_x	0.25
Magnification M_y	0.25
Slit dimensions (x, y–direction)	10.15 mm, 0.10 mm
Detector pixel dimensions (a, b–direction)	2.5 mm, 0.025 mm
Telescope focal length (x, y–direction)	200 mm, 40 mm
Aperture dimensions (x, y–direction)	24.1 mm , 17.0 mm
Spectral resolution λ_{res}	0.29 nm (1.5 px)
Average wavelength $\overline{\lambda}$	430 nm
Angle of illumination θ_i	12°
Angle of observation θ_o	0°

Table 6.1: Summary of the GOME VIS-3 spectrometer instrument parameters used as input for the prediction model taken from the GOME user manual (ESTEC Publishing Division, 1995).

User Manual one can see that the solar calibration takes $\Delta t_{cal} = 42\,\text{s}$ and that the angle of illumination changes roughly 3.5° during that time. Now, we want to find the averaging factor due to this angular change over time M_{time}. A similar approach is taken as in section 4.1.2. We need to find the correlation function μ between the speckle fields $\mathbf{A}(\theta_{i1})$ and $\mathbf{A}(\theta_{i2})$, where $\theta_{i1} = 12°$ as already established and $\theta_{i2} = 12°...15.5°$. From eq. (2.117) we get

$$\mu(\theta_{i1}, \theta_{i2}) = F(\Delta q_z(\theta_{i1}, \theta_{i2}))\,\Psi(\Delta x, \Delta y) \tag{6.36}$$

We adopt the approximation by J. W. Goodman, 2020, p. 205 that only the effective surface height fluctuations denoted by F affect the correlation appreciably, which yields with eqs. (6.33) and (6.34)

$$\mu(\theta_{i1}, \theta_{i2}) = \exp\left(-\sigma_h \left| \frac{2\pi}{\overline{\lambda}} \left[\cos(\theta_{i1}) - \cos(\theta_{i2})\right] \right|\right), \tag{6.37}$$

where $\overline{\lambda} = 430\,\text{nm}$ is the average wavelength in the considered range. We continue with the method described in section 4.1.2, where a coherency matrix is defined with values of $\mu\left(\theta_{i1}, \theta_{i2}\right)$. The time averaging factor due to angular change calculates to

$$M_{time} \approx 1.8. \tag{6.38}$$

The SFA including this effect is then

$$SFA'_{GOME} = \frac{SFA_{GOME}}{\sqrt{M_{time}}} = \frac{0.64\,\%}{\sqrt{1.8}} = 0.47\,\%. \tag{6.39}$$

Note that the angular dispersion of the speckle pattern at the detector may enlarge the speckle size $L_{c,det}$ as observed by Snel et al., 2009 in the SCIAMACHY diffuser characterization. Thus, the estimated speckle size is a lower limit. At last, let us discuss the effect of a larger surface roughness parameter σ_h, since it can only be roughly estimated with the information available (ESTEC Publishing Division, 1995). An increase in this parameter reduces the width of the spectral and angular correlation functions (see eqs. (6.33) and (6.37)) and in turn the speckle size $L_{c,det}$ and increases the angular time averaging factor M_{time}. In the following additional SFA results including the initial one from above are summarized for realistic values of $\sigma_h = 50\overline{\lambda} = 21.5\,\mu\text{m}$ and $\sigma_h = 70\overline{\lambda} = 30\,\mu\text{m}$:

$$\sigma_h = 30\overline{\lambda}: \quad SFA'_{GOME} = 0.47\,\% \quad L_{c,det} = 10.0\,\text{px} \tag{6.40}$$

$$\sigma_h = 50\overline{\lambda}: \quad SFA'_{GOME} = 0.39\,\% \quad L_{c,det} = 6.0\,\text{px} \tag{6.41}$$

$$\sigma_h = 70\overline{\lambda}: \quad SFA'_{GOME} = 0.34\,\% \quad L_{c,det} = 4.3\,\text{px}. \tag{6.42}$$

6.5 Speckle Distortion of the Solar Reference

In this section, the procedure of generating random speckle signals with parameters consistent with the predictions of the previous section 6.4 is outlined. The speckle error is characterized by two parameters, namely the amplitude SFA and the

speckle size $L_{c,det}$. The considered spectral regime for the NO_2 column retrieval is between 400 nm and 471 nm. The spectral resolution of the GOME instrument is $0.2\,\mathrm{nm\,px^{-1}}$, thus the 71 nm wide spectral range is sampled by $w = 355\,\mathrm{px}$, which should also be the spectral width of the speckle error signal. We follow the approach of Duncan and Kirkpatrick, 2008 to compute random complex gaussian speckle patterns as presented in section 2.2.1. In a two-dimensional array W of size $w \times w$ with zero amplitudes an aperture of dimension $g \times g$ is defined, where the size is chosen according to the desired speckle size with $g = \frac{w}{L_{c,det}}$. Inside this aperture, the elements of W are added with a random phase factor $\exp(j2\pi r)$, where $0 \leq r \leq 1$ is a uniformly distributed random number. Note that the exact position of the aperture in W does not matter and that $w > 2g$. The Fourier transform of W, $F_W = FT\{W\}$ yields a random 2D speckle pattern S with unity contrast by multiplying with the complex conjugate ($*$):

$$S = F_W F_W^*.$$

Two examples for S with different speckle sizes $L_{c,det}$ are shown in fig. 6.2. In

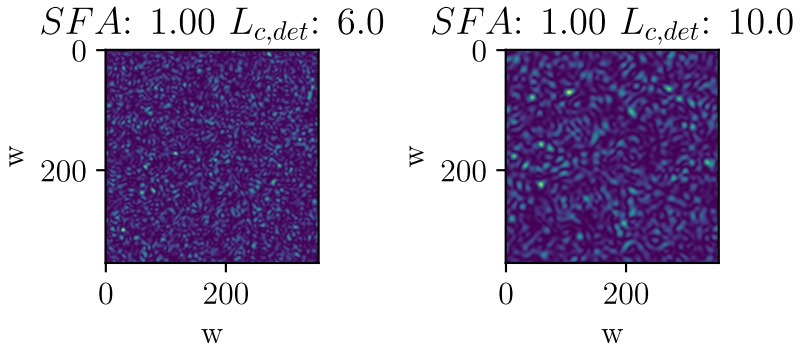

Figure 6.2: Example of generated speckle patterns: (left) with a speckle size of $L_{c,det} = 6.0\,\mathrm{px}$ and (right) with $L_{c,det} = 10.0\,\mathrm{px}$.

order to reduce the contrast of the images to the desired SFA, we use eq. (2.126) to determine the amount of M_{sum} independent speckle patterns that need to be

summed (see section 2.2.2 for details):

$$M_{sum} = \frac{1}{SFA^2}. \tag{6.43}$$

The speckle pattern having the target SFA is output after summation of M_{sum} individual random speckle patterns. As a last step we take a random row i or column j from the summed speckle pattern S_{sum} and set its mean to unity yielding the speckle error signal as shown fig. 6.3 for an amplitude of $SFA = 0.2\,\%$ and a speckle size of $L_{c,det} = 10.0\,\text{px}$. Multiple independent speckle error spectra can be

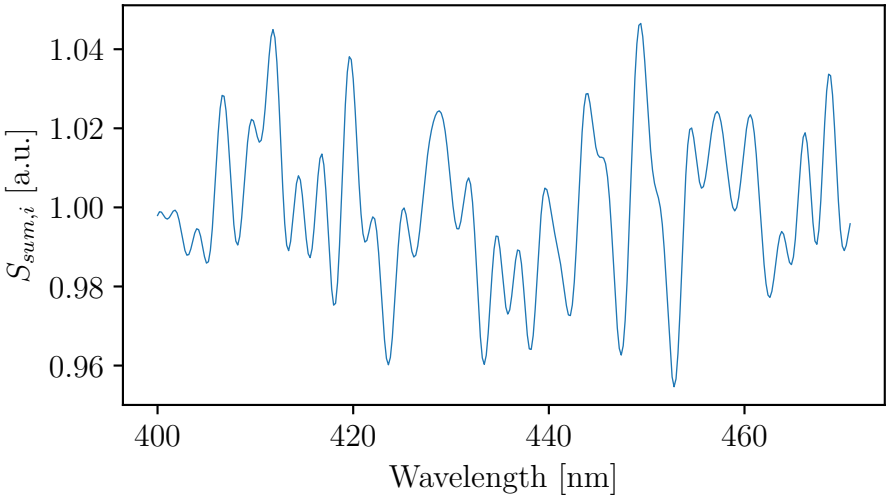

Figure 6.3: Example of generated speckle error spectrum with $SFA = 0.2\,\%$ and $L_{c,det} = 10.0\,\text{px}$.

extracted from a single 2D pattern if the row or column indices are at least $L_{c,det}$ apart. The simulated diffusers are therefore different in regard to their scattering centers but exhibit the same overall speckle statistic in terms of amplitude and size. In table 6.2 the parameter combinations are shown for which error spectra are generated. They are based on the prediction results of section 6.4. For every combination, 40 different spectra are generated, which means that peaks and valleys inside an individual spectrum are distributed differently every time. This ensures some degree of statistical independence from random features in the speckle spectra coinciding with absorption features in the Earth reflectance spectrum.

$L_{c,det}$	SFA
3.0 px	0.1 %
3.0 px	0.4 %
3.0 px	0.8 %
3.0 px	2.0 %
6.5 px	0.1 %
6.5 px	0.4 %
6.5 px	0.8 %
6.5 px	2.0 %
9.0 px	0.1 %
9.0 px	0.4 %
9.0 px	0.8 %
9.0 px	2.0 %

Table 6.2: Summary of the parameter combinations of artificial speckle error spectra. For every set 40 different spectra are generated.

6.6 Retrieval Results and Discussion

In this section, the DOAS retrieval results obtained with the data and methods described previously are presented and discussed. The goal is to estimate the deviation of a DOAS retrieval (see section 6.1) using various speckle-distorted solar reference spectra and compare them to a ground truth retrieval, for which no speckle error is applied. The parameters for the error spectra are chosen according to the predictions in section 6.4, which are derived from the parameters of the GOME instrument. In section 6.5 variations of speckle-distorted spectra around these predicted speckle error parameters are generated. In the following, the retrieval deviations are evaluated with respect to the prior derived prediction parameters and compared to actually observed diffuser errors in the retrieved NO_2 column density (see Richter and Wagner, 2001; Wenig et al., 2004). The retrieval is performed on an artificial Earth reflectance spectrum which is generated via an RTM (see section 6.2). In addition to the speckle error, random detector noise is included in the retrieval process as a comparable error source. In the following, the performed retrieval modes are described:

Ground truth: in this case, no detector noise or speckle distortion to any parts

of the retrieval inputs are applied.

Detector noise: only detector noise of various magnitudes $\sigma \in \{0.05, 0.1, 0.2, 0.5\}$ is added to the target signal, where σ is in % of the signal's mean. Target signals are the solar reference and the Earth reflectance spectrum. For every magnitude σ, the retrieval is repeated ten times with a newly generated noise signal. This totals a number of 40 retrievals for this mode.

Detector noise + speckle distortion: detector noise is added as in the previous case to both, the Earth reflectance spectrum and the solar reference with magnitudes $\sigma \in \{0, 0.05, 0.1, 0.2, 0.5\}$. Additionally, the speckle error signals from section 6.5 are multiplied to the solar reference. For every parameter combination of amplitude (SFA) and speckle size ($L_{c,det}$) the retrieval is performed with 40 independent error signals, which in turn are repeated ten times with different random detector signals. This totals a number of 400 retrievals for each of the twelve speckle parameter combinations from section 6.5, table 6.2.

The slit function used for the retrieval is Gaussian shaped with FWHM of 0.29 nm. The retrieved column densities were received by Ka Lok Chan (personal correspondence, 2021). For the retrieval, the slit function is convolved with the generated Earth reflectance spectrum (see section 6.3), after which they are resampled to the GOME instrument resolution. The same procedure is applied to the presented absorption cross-sections. They are then used for the DOAS fit. A fourth-order polynomial fit is included in the spectral fit in order to remove low-frequency structures due to Rayleigh scattering. In fig. 6.4 the relative retrieval deviation from the ground truth in terms of the NO_2 slant column density for the speckle-distortion parameter combination $L_{c,det} = 6.5\,\text{px}$, $SFA = 0.4\,\%$ and two different detector noise levels of 0.05 % and 0.5 % are depicted. The steps in the graphs are due to the fact that for each one of the 40 speckle error signals, the retrieval is repeated ten times with different random detector noise. The high-frequency variations are more notable for a higher detector noise. In table 6.3 the retrieval

deviations for all speckle-distortion and detector noise parameter combination are summarized. Every entry corresponds to the RMS value of the graphs as shown in fig. 6.4. Note that the first row's entries represent deviations with only detector noise present in the input data. This effectively corresponds to a speckle size of one pixel and an SFA of σ. The bold-faced entries are in agreement with originally observed deviations for the GOME instrument of 50 % (see Richter and Wagner, 2001; Wenig et al., 2004). From the presented data, one can derive that the SFA leading to a retrieval error matching the one observed for the GOME instrument is around 0.4 %, which is in very good agreement with the SFA model predictions from section 6.4. For the speckle size $L_{c,det}$ one can infer a lower limit which lies between 3 and 6 pixels, which is also in the prediction range. For speckle sizes above this threshold, the data suggest that the retrieval deviation does not increase further. The contribution of the detector noise appears to be fairly constant with only a slight increase towards cases with $\sigma = 0.5\,\%$ if the speckle-distortion has an amplitude of $SFA > 0.1\,\%$. For the other cases, it increases linearly with σ. In conclusion, we have shown that the prediction model for diffuser speckle is capable of estimating the parameters for an error signal from basic GOME instrument parameters, which in turn leads to an error in the retrieved NO_2 slant column density when incorporated in a DOAS retrieval. This error matches the actually observed deviation seen in retrieved columns from the real GOME instrument, which suggests a valid model prediction. We also give indications to what extent the speckle error signals of various severity impact the retrieval result and how this effect compares with detector noise.

$L_{c,det}$, SFA	$\sigma = 0.0\,\%$	$\sigma = 0.05\,\%$	$\sigma = 0.1\,\%$	$\sigma = 0.2\,\%$	$\sigma = 0.5\,\%$
1.0 px, σ	0	3.40	6.27	13.22	28.48
3.0 px, 0.1 %	9.97	10.31	11.53	15.94	28.48
3.0 px, 0.4 %	33.70	33.84	34.26	35.82	**45.91**
3.0 px, 0.8 %	80.28	83.43	81.77	85.00	92.17
3.0 px, 2.0 %	219.89	217.22	213.97	212.76	212.55
6.5 px, 0.1 %	11.83	12.06	12.96	16.97	31.36
6.5 px, 0.4 %	**47.94**	**47.77**	**46.93**	**48.50**	**55.28**
6.5 px, 0.8 %	118.09	117.51	117.41	114.21	111.53
6.5 px, 2.0 %	304.06	306.61	306.22	310.57	301.73
9.0 px, 0.1 %	15.33	15.52	16.35	19.58	32.69
9.0 px, 0.4 %	**44.55**	**43.54**	**44.02**	**46.65**	**55.30**
9.0 px, 0.8 %	110.08	107.90	108.36	106.12	110.63
9.0 px, 2.0 %	320.13	311.30	311.42	313.01	318.56

Table 6.3: Average retrieval deviations in % of the NO_2 column density performed with various speckle-distorted solar reference spectra with parameters ($L_{c,det}$, SFA) and random detector noise of magnitude σ compared with the ground truth. The calculated number is the standard deviation over all retrieved column densities subtracted with the ground truth. The bold-faced entries are in agreement with originally observed deviations for the GOME instrument of about 50 % (see Richter and Wagner, 2001; Wenig et al., 2004). They also match the theoretical expectation determined with the model in section 6.4, which indirectly suggests a reliable prediction.

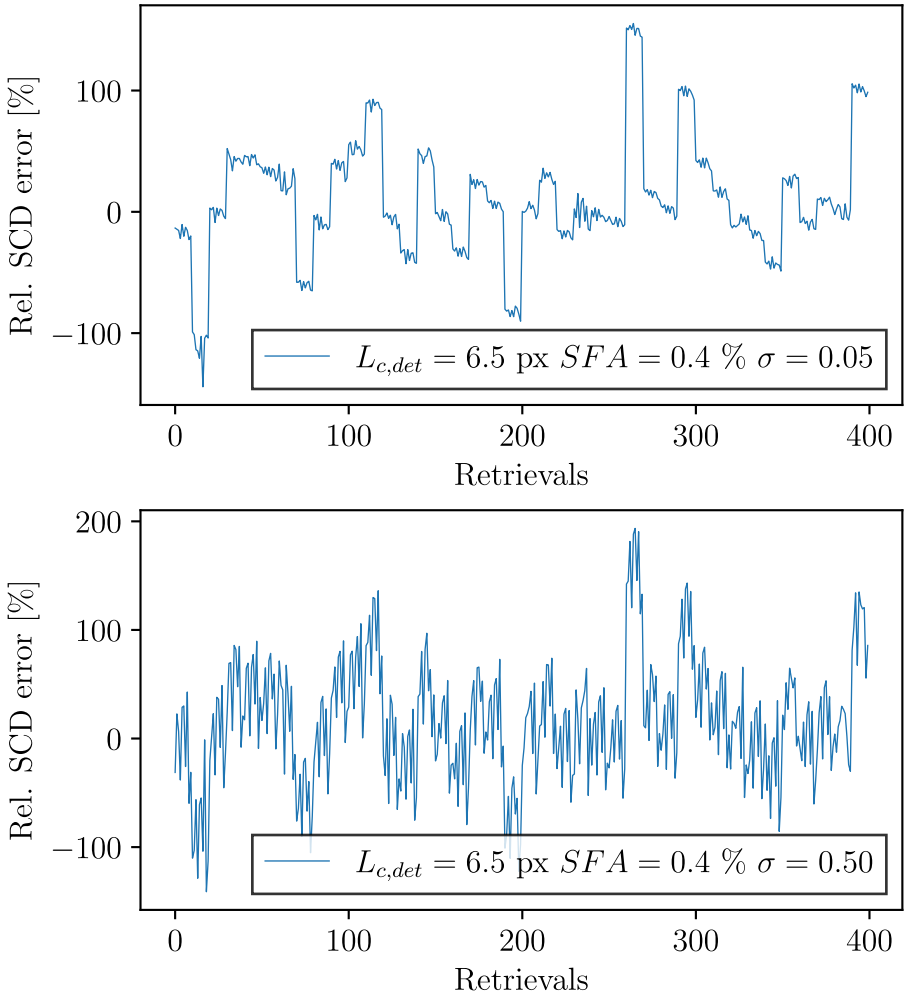

Figure 6.4: Two examples of the relative retrieval deviation from the ground truth in terms of the NO_2 slant column density for parameter combinations $L_{c,det} = 6.5\,\text{px}$, $SFA = 0.4\,\%$, and (top) $\sigma = 0.05\,\%$ and (bottom) $\sigma = 0.5\,\%$. The steps in the graph are due to the fact that for each of the 40 speckle error spectra, ten retrievals are performed with different random noise contributions. This ensures some degree of statistical independence from random features in the noise contributions coinciding with absorption features in the Earth reflectance spectrum. The 40 different speckle error spectra correspond to distinct simulated diffusers in regard to their scattering centers but exhibit the same overall speckle statistic in terms of amplitude and size. Depending on the spectral position of the diffuser features, they cause different retrieval deviations. Comparing both panels, the influence of random noise becomes evident. The bottom one represents the top one with a more pronounced random modulation.

Chapter 7

Conclusion and Outlook

In this thesis, novel experimental and theoretical methods of characterizing diffuser-induced Spectral Features by speckles in imaging spectrometers have been explored, improved, and developed. The Spectral Features cannot only diminish the quality of the in-orbit radiometric calibration but also cause significant errors when the speckle distorted solar reference spectrum is used in the context of the commonly used Differential Optical Absorption Spectroscopy method to retrieve the column densities of the trace gases. The Spectral Features are usually high-frequency contributions and will therefore appear as additional absorption features that essentially reduce the accuracy of the Differential Optical Absorption Spectroscopy fit to the cross-sections of the individual specimen. Until recently, the speckle error was mostly characterized with representative end-to-end setups for every new instrument. Besides the high costs, the underlying speckle effects leading to the measured diffuser signal at the detection plane remained hidden. For modern instrument designs, the speckle error amplitudes are so small that the diffuser signal cannot be reliably distinguished from other error sources, such as straylight. The optical system was a black box in terms of the speckle effect. This also made the development of reliable theoretical models a difficult task. Therefore, in this thesis, a recently developed alternative measurement method is explored, matured, and characterized in terms of uncertainties. It significantly reduces the complexity

of the experimental system and can be adjusted to different instruments quickly. One is able to measure even small speckle signals and track how the diffuser signal progresses through the instrument. Especially the last aspect allowed for the development of a standalone mathematical prediction model based on established speckle theory, which constitutes the key achievement of this work. With this model, no experimental efforts are needed in order to quantify the diffuser speckle signal at the detector plane. It requires a few basic instrument parameters as well as scattering parameters of the diffuser. The predictions of the model are compared to results acquired with the above-mentioned measurement method for a current instrument design. Both prediction and measurement are in good agreement. To further show the validity of the model, additional measurements are conducted with a complete end-to-end setup. In contrast to the representative setups for actual instruments mentioned above, it was purposely designed to yield a distinct diffuser signal, which allowed for a reliable comparison to the prediction. Also, in this experiment, the measurement results agree well with the developed theory. Finally, the impact of diffuser speckle signals on the Differential Optical Absorption Spectroscopy method is analyzed. For this, a measurement with a spectrometer of the Global Ozone Monitoring Experiment is simulated. The solar reference used for the retrieval of the trace gas concentrations is distorted with a range of diffuser signals featuring different severities. Only the diffuser signals with parameters predicted by the model led to the column density deviations that matched the ones found in literature. This constitutes another implicit validation of the prediction model.

The case of the Global Ozone Monitoring Experiment is an extreme example in terms of the diffuser speckle error. More recent instruments use other diffuser materials and geometries, which have less impact. However, the issue of quantifying the speckle error as part of the total error budget still remains. Especially in the early planning phases of future instruments the prediction model presented in this work can be used to estimate the speckle contributions quickly. It is the first model fundamentally based on known speckle theory concepts. With the trend to finer

spectral resolutions for prospective missions, the diffuser Spectral Features will potentially gain more significance. This thesis can serve as a solid basis for future investigations. For example, angular effects due to the satellite's movement during the solar calibration may have a significant impact on the perceived diffuser signal. Also, the contribution of the Sun as an extended light source is not fully understood. Any new insights can be incorporated into the current version of the prediction model. This work provides a good starting point for how future research can be conducted on this topic.

Bibliography

B. Ahlers et al. (2004). "In-orbit detection of spectral features in SCIAMACHY". *Sensors, Systems, and Next-Generation Satellites VIII*. Ed. by R. Meynart et al. Vol. 5570. International Society for Optics and Photonics. SPIE, pp. 401–410.

S. Ahn and J. Fessler (2003). "Standard Errors of Mean, Variance, and Standard Deviation Estimators".

G. P. Anderson et al. (1986). *AFGL atmospheric constituent profiles (0-120 km).* Tech. rep. AFGL-TR-86-0110. Hanscom Air Force Base, Bedford, Mass.: Air Force Geophys. Lab.

N. Baddour (2011). "Two-Dimensional Fourier Transforms in Polar Coordinates". *Advances in Imaging and Electron Physics*. Elsevier, pp. 1–45.

J. Bertolotti (2007). "Light transport beyond diffusion". PhD thesis. Università degli studi di Firenze.

V. Bianco et al. (2018). "Strategies for reducing speckle noise in digital holography". *Light: Science and Applications* **7**.1, p. 48.

H. van Brug and G. B. Courrèges-Lacoste (2007). "Spectral features, effects, and cures". *Earth Observing Systems XII*. Ed. by J. J. Butler and J. Xiong. SPIE.

H. van Brug and P. S. Scalia (2012). "New approach to spectral features modeling". *Earth Observing Systems XVII*. Ed. by J. J. Butler et al. SPIE.

H. van Brug et al. (2004). "Speckles and their effects in spectrometers due to on-board diffusers". *Earth Observing Systems IX*. Ed. by W. L. Barnes and J. J. Butler. SPIE.

R. Buras et al. (2011). "New secondary-scattering correction in DISORT with increased efficiency for forward scattering". *Journal of Quantitative Spectroscopy and Radiative Transfer* **112**.12, pp. 2028–2034.

T. Burns et al. (2017). "Sentinel-5: a novel measurement approach to quantify diffuser induced spectral features". *International Conference on Space Optics ICSO 2016*. Ed. by N. Karafolas et al. SPIE.

J. P. Burrows et al. (1999). "The Global Ozone Monitoring Experiment (GOME): Mission Concept and First Scientific Results". *Journal of the Atmospheric Sciences* **56**.2, pp. 151–175.

J. Caron (2020). "Personal correspondence". Theory of speckle averaging, 2017.

K. Chance and R. Kurucz (2010). "An improved high-resolution solar reference spectrum for earth's atmosphere measurements in the ultraviolet, visible, and near infrared". *Journal of Quantitative Spectroscopy and Radiative Transfer* **111**.9, pp. 1289–1295.

S. Chandrasekhar (2011). *Radiative Transfer*. DOVER PUBN INC. 416 pp.

J. C. Dainty et al. (1975). *Laser Speckle and Related Phenomena*. Springer Berlin Heidelberg.

D. Draganovská et al. (2018). *General Regression Model for Predicting Surface Topography after Abrasive Blasting*.

D. D. Duncan and S. J. Kirkpatrick (2008). "The copula: a tool for simulating speckle dynamics". *J. Opt. Soc. Am. A* **25**.1, pp. 231–237.

P. Elies et al. (1997). "Experimental investigation of the speckle polarization for a polished aluminium sample". *Journal of Physics D: Applied Physics* **30**.1, pp. 29–39.

C. Emde et al. (2016). "The libRadtran software package for radiative transfer calculations (version 2.0.1)". *Geoscientific Model Development* **9**.5, pp. 1647–1672.

A. Erdélyi et al. (1953). *Higher Transcendental Functions. Vol. II*. 2 vols. New York-Toronto-London: McGraw-Hill Book Company. eprint: `https://resolver.caltech.edu/CaltechAUTHORS:20140123-104529738`.

ESTEC Publishing Division (1995). *GOME User Manual*. ESA. eprint: `https://earth.esa.int/documents/10174/1596664/GOME05.pdf`.

K. Fletcher et al. (2015). *Report for Mission Selection: Carbonsat Flex*. ESA SP. ESA Communication Production Office.

R. J. Freund et al. (2006). *Regression Analysis : Statistical Modeling of a Response Variable*. Burlington, UNITED STATES: Elsevier Science & Technology.

N. George and A. Jain (1974). "Space and wavelength dependence of speckle intensity". *Applied Physics* **4**.3, pp. 201–212.

J. Goodman (1975). "Dependence of image speckle contrast on surface roughness". *Optics Communications* **14**.3, pp. 324–327.

J. W. Goodman (2007). *Speckle Phenomena in Optics: Theory and Application*. Roberts & Company Publishers.

J. W. Goodman (2015). *Statistical Optics*. New York: John Wiley & Sons, Incorporated.

J. W. Goodman (2017). *Introduction to Fourier optics*. English.

J. W. Goodman (2020). *Speckle phenomena in optics : theory and applications*. Bellingham, Washington: SPIE Press.

I. S. Gradshteyn (2007). *Table of integrals, series and products*. Oxford: Academic.

R. M. Gray (2006). "Toeplitz and Circulant Matrices: A review". eprint: `https://ee.stanford.edu/~gray/toeplitz.pdf`.

U. Grenander and G. Szegö (1958). "Toeplitz Forms and their Applications". *University of California Press*.

T. Guehne et al. (2017). "Sentinel-5 instrument: status of design, performance, and development". *Sensors, Systems, and Next-Generation Satellites XXI*. SPIE.

E. Hecht and K. Lippert (2018). *Optik*. Berlin, Boston: De Gruyter.

W. Heeman et al. (2019). "Clinical applications of laser speckle contrast imaging: a review". *Journal of Biomedical Optics* **24**.8, pp. 1–11.

G. C. Hegerl et al. (2019). "Causes of climate change over the historical record". *Environmental Research Letters* **14**.12, p. 123006.

G. Heraeus Conamic (2021). *HOD®-500 Datasheet*.

O. C. Ibe (2013). *Elements of Random Walk and Diffusion Processes*. Wiley-Blackwell. 276 pp.

IPCC (2014). *Climate Change 2013 - The Physical Science Basis: Working Group I Contribution to the Fifth Assessment Report of the Intergovernmental Panel on Climate Change*. Cambridge: Cambridge University Press.

IPCC (2015). *Climate Change 2014 : Synthesis Report. Contribution of Working Groups I, II and III to the Fifth Assessment Report of the Intergovernmental Panel on Climate Change*. Ed. by R. K. Pachauri. Ed. by L. A. Meyer. Geneva, Switzerland: Intergovernmental Panel on Climate Change. 151 pp.

J. Irizar et al. (2019). "Sentinel-5/UVNS". *International Conference on Space Optics 2018*. Ed. by Z. Sodnik et al. Vol. 11180. International Society for Optics and Photonics. SPIE, pp. 41–58.

B. Jähne et al. (1999). *Handbook of computer vision and applications*. Vol. 2. San Diego: Academic Press, Inc.

A. Klenke (2013). *Wahrscheinlichkeitstheorie*. Springer Berlin Heidelberg.

K.-S. Kuo et al. (1996). "The picard iterative approximation to the solution of the integral equation of radiative transfer—part II. Three-dimensional geometry". *Journal of Quantitative Spectroscopy and Radiative Transfer* **55**.2, pp. 195–213.

G. Landi and A. Zampini (2018). *Linear Algebra and Analytic Geometry for Physical Sciences*. Springer International Publishing.

J. M. Lerner (2006). "Imaging spectrometer fundamentals for researchers in the biosciences - A tutorial". *Cytometry Part A* **69A**.8, pp. 712–734. eprint: `https://onlinelibrary.wiley.com/doi/pdf/10.1002/cyto.a.20242`.

J. R. Lorenzo (2012). *Principles of Diffuse Light Propagation*. World Scientific Publishing Company. 356 pp.

I. H. Malitson (1965). "Interspecimen Comparison of the Refractive Index of Fused Silica∗,†". *J. Opt. Soc. Am.* **55**.10, pp. 1205–1209.

R. J. Marks (2009). *Handbook of Fourier Analysis & Its Applications*. Oxford University Press.

B. Mayer and A. Kylling (2005). "Technical note: The libRadtran software package for radiative transfer calculations - description and examples of use". *Atmospheric Chemistry and Physics* **5**.7, pp. 1855–1877.

Y. Meijer et al. (2019). *Copernicus CO2 Monitoring Mission Requirements Document*. Tech. rep. 2. European Space Agency, Earth and Mission Science Division. eprint: `https://esamultimedia.esa.int/docs/EarthObservation/CO2M_MRD_v2.0_Issued20190927.pdf`.

D. Middleton (1960). *An introduction to statistical communication theory*. International series in pure and applied physics. McGraw-Hill.

D. Mihalas (1978). *Stellar atmospheres*. San Francisco: W.H. Freeman.

C. Olij et al. (1997). "Spectralon diffuser calibration for MERIS". *Sensors, Systems, and Next-Generation Satellites*. Ed. by H. Fujisada. SPIE.

G. Parry (1975). "Speckle patterns in partially coherent light". PhD thesis. Imperial College of Science and Technology, Physics Department, University of London.

A. Richter and T. Wagner (2001). *Diffuser plate spectral structures and their influence on GOME slant columns*. Tech. rep. paper presented to the GOME Science Advisory Group, Bremen, Germany.

F. Richter et al. (2021). "Prediction model for diffuser-induced spectral features in imaging spectrometers". *Atmospheric Measurement Techniques* **14**.2, pp. 1561–1571.

F. Richter et al. (2018). "A novel measurement approach to quantify diffuser induced Spectral Features". *Sensors, Systems, and Next-Generation Satellites XXII*. Ed. by S. P. Neeck et al. SPIE.

L. Rothman et al. (2010). "HITEMP, the high-temperature molecular spectroscopic database". *Journal of Quantitative Spectroscopy and Radiative Transfer* **111**.15, pp. 2139–2150.

A. Serdyuchenko et al. (2014). "High spectral resolution ozone absorption cross-sections – Part 2: Temperature dependence". *Atmospheric Measurement Techniques* **7**.2, pp. 625–636.

L. Slatineanu et al. (2011). "Surface Roughness at Aluminium Parts Sand Blasting". *Proceedings in Manufacturing Systems*. Vol. II.2. Editura Acamdemiei Romane, pp. 69–74.

R. C. Snel et al. (2009). "In-flight calibration of the bidirectional reflectance distribtution function of the SCIAMACHY ESM diffuser". *Atmospheric Science Conference Proceedings*. SP-676. ESA Communication Office.

K. Stamnes et al. (2000). *DISORT, a General-Purpose Fortran Program for Discrete-Ordinate-Method Radiative Transfer in Scattering and Emitting Layered Media: Documentation of Methodology*. Tech. rep. NJ 07030. Hoboken: Dept. of Physics and Engineering Physics, Stevens Institute of Technology.

K. Stamnes (1986). "The theory of multiple scattering of radiation in plane parallel atmospheres". *Reviews of Geophysics* **24**.2, p. 299.

K. Stamnes et al. (1988). "Numerically stable algorithm for discrete-ordinate-method radiative transfer in multiple scattering and emitting layered media". *Applied Optics* **27**.12, p. 2502.

J. Stutz et al. (2008). *Differential Optical Absorption Spectroscopy*. Springer Berlin Heidelberg. 616 pp.

R. Thalman and R. Volkamer (2013). "Temperature dependent absorption cross-sections of O2–O2 collision pairs between 340 and 630 nm and at atmospherically relevant pressure". *Physical Chemistry Chemical Physics* **15**.37, p. 15371.

G. Thomas (1999). *Radiative transfer in the atmosphere and ocean*. Cambridge New York: Cambridge University Press.

A. Vandaele et al. (1998). "Measurements of the NO2 absorption cross-section from 42 000 cm-1 to 10 000 cm-1 (238–1000 nm) at 220 K and 294 K". *Journal of Quantitative Spectroscopy and Radiative Transfer* **59**.3-5, pp. 171–184.

R. Voors et al. (2017). "TROPOMI, the Sentinel 5 precursor instrument for air quality and climate observations: status of the current design". *International Conference on Space Optics 2012*. Ed. by B. Cugny et al. Vol. 10564. International Society for Optics and Photonics. SPIE, pp. 442–446.

M. Wenig et al. (2004). “Retrieval and analysis of stratospheric NO2 from the Global Ozone Monitoring Experiment”. *Journal of Geophysical Research: Atmospheres* **109**.D4.

M. Wenig et al. (2005). “Operator representation as a new differential optical absorption spectroscopy formalism”. *Applied Optics* **44**.16, p. 3246.

E. Wolf (1959). “Coherence properties of partially polarized electromagnetic radiation”. *Il Nuovo Cimento* **13**.6, pp. 1165–1181.

J. X. Zhu et al. (1991). “Internal reflection of diffusive light in random media”. *Phys. Rev. A* **44** (6), pp. 3948–3959.

Appendices

Listing 7.1: libRadtran input file for generating Earth reflectance

```
output_user wavelength uu
zout TOA
output_quantity reflectivity
sza 32.0
atmosphere_file afglus.dat
source solar sao2010_solref_air_highres_400_470.dat
mol_abs_param crs
mol_file no2 afglus_no2.dat cm_3
mol_file h2o afglus_h2o.dat cm_3
mol_file o3 afglus_o3.dat cm_3
quiet
albedo 0.1
umu 1
phi 0
wavelength_grid_file lambdagridfile_400_470_1.0pm.TRANS
rte_solver disort
crs_file no2 NO2_Vandaele96_220K_air.xs
crs_file o3 o3_223K_SDY_air.xs
crs_file o4 o4_Thalman_Volkamer_293K_air_corrected.xs
crs_file h2o H2O_HITEMP_2010_390-700_296K_1013mbar_air.xs
```

Acknowledgements

During the course of my work for this thesis I was supported by a lot of friendly people whom I want to thank now:

Prof. Dr. Mark Wenig for supervising the Ph.D. project from university-side and for the great support over the years,

Dr. Dennis Weise for enabling and initializing the Ph.D. project from Airbus-side,

Dr. Jasper Krauser for your support and your initiative to cooperate with various interesting projects.

Dr. Corneli Keim for supervising and supporting me every step of the long way,

Dr. Maximilian Harlander for always bringing new and insightful ideas to my attention,

Sorin Bota for the many hours in the lab and numerous talks with valuable advice,

Frank Nürnberg and Bernhard Franz, Heraeus Conamic, Germany kindly provided the fused silica diffuser HOD®-500 used in this work.

Further I want to thank my family and friends for their support and patience.